CARRIER RELAXATION DYNAMICS IN GRAPHENE

Martin Mittendorff

WISSENSCHAFTLICH-
TECHNISCHE BERICHTE

HZDR

HELMHOLTZ
ZENTRUM DRESDEN
ROSSENDORF

Martin Mittendorff

CARRIER RELAXATION DYNAMICS IN GRAPHENE

HZDR

HELMHOLTZ
ZENTRUM DRESDEN
ROSSENDORF

Carrier Relaxation Dynamics in Graphene

DISSERTATION

zur Erlangung des akademischen Grades

Doctor rerum naturalium
(Dr. rer. nat.)

vorgelegt
der Fakultät Mathematik und Naturwissenschaften
der Technischen Universität Dresden

von
Dipl. Ing. (FH) Martin Mittendorff
geboren am 07.06.1979 in Heilbronn

Die Dissertation wurde in der Zeit von 11 / 2010 bis 06 / 2014
im Institut für Ionenstrahlphysik und Materialforschung
angefertigt.

Abstract

Graphene, the two-dimensional lattice of sp^2-hybridized carbon atoms, has a great potential for future electronics, in particular for opto-electronic devices. The carrier relaxation dynamics, which is of key importance for such applications, is in the main focus of this thesis. Besides a short introduction into the most prominent material properties of graphene and the experimental techniques, this thesis is divided into three main parts.

The investigation of the carrier relaxation dynamics in the absence of a magnetic field is presented in Chapter 3. In the first experiment, the anisotropy of the carrier excitation and relaxation in momentum space was investigated by pump-probe measurements in the near-infrared range. While this anisotropy was not considered in all previous experiments, our measurements with a temporal resolution of less than 50 fs revealed the polarization dependence of the carrier excitation and the subsequent relaxation. About 150 fs after the electrons are excited, the carrier distribution in momentum space gets isotropic, caused by electron-phonon scattering. In a second set of two-color pump-probe experiments, the temperature of the hot carrier distribution, which was obtained within the duration of the pump pulse (about 200 fs), could be estimated. Furthermore, a change in sign of the pump-probe signal can be used as an indicator for the Fermi energy of different graphene layers. Pump-probe experiments in the far-infrared range in reflection and transmission geometry were performed at high pump power. A strong saturation of the pump-induced transmission was found in previous experiments, which was attributed to the pump-induced change in absorption. Our investigation shows the strong influence of pump-induced reflection at long wavelengths, as well as a lot smaller influence of the saturation of the pump-induced change in absorption. At a high pump power, the increase of the reflection exceeds the change in absorption strongly, which leads to negative pump-probe signals in transmission geometry.

In Chapter 4, investigations of the carrier dynamics of graphene in magnetic fields of up to 7 T are presented. Even though the optical properties of Landau-quantized graphene are very interesting, the carrier dynamics were nearly unexplored. A low photon energy of 14 meV allows the investigation of the intraband Landau-level (LL) transitions. These experiments revealed two main findings: Firstly, the Landau quantization strongly suppresses the carrier relaxation via optical-phonon scattering, resulting in an increased relaxation time. Secondly, a change in sign of the pump-

probe signal can be observed when the magnetic field is varied. This change in sign indicates a hot carrier distribution shortly after the pump pulse, which means that carrier-carrier scattering remains very strong in magnetic fields. In a second set of pump-probe measurements, carried out at a photon energy of $75\,\mathrm{meV}$, the relaxation dynamics of interband LL transitions was investigated. In particular, experiments on the two energetically degenerate LL transitions $LL_{-1} \Rightarrow LL_0$ and $LL_0 \Rightarrow LL_1$ showed the influence of extremely strong Auger processes.

An ultrafast and extremely broadband terahertz detector, based on a graphene flake, is presented in the last chapter of this thesis. To couple the radiation efficiently to the small flake, the inner part of a logarithmic periodic antenna is connected to it. With a rise time of about $50\,\mathrm{ps}$ in a wavelength range of $9\,\mu\mathrm{m}$ to $500\,\mu\mathrm{m}$, this detector is very interesting to obtain the temporal overlap in two-color pump-probe experiments with the free-electron laser FELBE. Furthermore, the importance of the substrate material, in particular for the high-speed performance, is discussed.

Zusammenfassung

Graphen besteht aus sp^2-hybridisierten Kohlenstoffatomen, die in einem zweidimensionalen Gitter angeordnet sind und hat ein großes Potential im Bereich der Elektronik, speziell für optoelektronische Bauteile. Der Schwerpunkt dieser Arbeit liegt in der Untersuchung der Ladungsträgerdynamik in Graphen, die eine Schlüsselrolle für die Entwicklung solcher Bauteile spielt. Neben einer kurzen Einführung in die wichtigsten Materialeigenschaften und die experimentellen Methoden besteht diese Arbeit aus drei Hauptteilen.

Untersuchungen der Ladungsträgerdynamik in Abwesenheit eines Magnetfeldes werden in Kapitel 3 vorgestellt. Die anisotrope Anregung und Relaxation der Ladungsträger wurde durch Anrege-Abfrage-Experimente im Nahinfrarotbereich untersucht. Während diese Anisotropie in allen bisherigen Anrege-Abfrage-Experimenten nicht berücksichtigt wurde, zeigen unsere Messungen mit einer zeitlichen Auflösung von unter 50 fs eine deutliche Polarisationsabhängigkeit für die Ladungsträgeranregung sowie die anschließende Relaxation. Durch Elektron-Phonon-Streuprozesse wird bereits nach etwa 150 fs eine isotrope Ladungsträgerverteilung erreicht. In einer zweiten Reihe von Zweifarben Anrege-Abfrage-Experimenten konnte die Temperatur der heißen Ladungsträgerverteilung, die sich bereits innerhalb des Anregepulses (ca. 200 fs) einstellt, ermittelt werden. Zusätzlich kann ein Vorzeichenwechsel in den Signalen der Anrege-Abfrage-Experimente genutzt werden um die Fermienergie in unterschiedlichen Graphenlagen zu bestimmen. Weitere Anrege-Abfrage-Experimente wurden im ferninfraroten Bereich durchgeführt, wobei in Reflexions- und Transmissionsgeometrie bei hoher Anregeleistung gemessen wurde. Bei vorherigen Experimenten wurde für das Transmissionssignal eine starke Sättigung gemessen, die auf eine Sättigung der Absorption zurückgeführt wurde. Unsere Untersuchungen zeigen sowohl einen starken Einfluss der Reflexionsänderung, als auch einen deutlich kleineren Einfluss der Absorptionsänderung auf das gemessene Transmissionssignal. Bei sehr hohen Anregeleistungen überwiegt die erhöhte Reflexion gegenüber der reduzierten Absorption der Probe, was zu einem negativen Transmissionssignal führt.

In Kapitel 4, werden die Untersuchungen der Relaxationsdynamik in Magnetfeldern von bis zu 7 T vorgestellt. Obwohl die optischen Eigenschaften von Landauquantisiertem Graphen sehr interessant sind, blieb die Ladungsträgerdynamik im Magnetfeld bisher nahezu unerforscht. Eine geringe Photonenenergie von 14 meV

erlaubt die Untersuchung von Intraband-Landauniveau-Übergängen. Diese Experimente enthüllten zwei grundlegende Effekte: Zum einen unterdrückt die Landauquantisierung die Ladungsträgerrelaxation über Elektron-Phonon-Streuprozesse, was zu einer ansteigenden Relaxationszeit führt. Zum anderen kann ein Vorzeichenwechsel im Transmissionssignal beobachtet werden, wenn das magnetische Feld verändert wird. Dieser Vorzeichenwechsel weist auf eine heiße Ladungsträgerverteilung hin, die bereits kurz nach der Anregung erreicht wird. Das schnelle Erreichen der heißen Verteilung zeigt, dass Elektron-Elektron-Streuprozesse auch im Magnetfeld sehr stark bleiben. In einer zweiten Messreihe, die bei einer Photonenenergie von 75 meV durchgeführt wurde, wurde die Ladungsträgerdynamik von Interband-Landauniveau-Übergängen untersucht. Besonders interessant sind die Messungen an den zwei energetisch entarteten Landauniveau-Übergängen $LL_{-1} \Rightarrow LL_0$ und $LL_0 \Rightarrow LL_1$, die einen starken Einfluss von Augerprozessen zeigt.

Ein extrem schneller und sehr breitbandiger Terahertz-Detektor, der auf einer Graphen-Flocke basiert, wird im letzten Kapitel dieser Arbeit vorgestellt. Um die langwellige Strahlung effizient anzukoppeln, ist eine logarithmisch-periodische Antenne mit der kleinen Flocke verbunden. Mit einer Anstiegszeit von ca. 50 ps im Wellenlängebereich von 9 μm bis 500 μm ist dieser Detektor sehr interessant, um den zeitlichen Überlapp für Zweifarb-Experimente mit dem Freie-Elektronen-Laser FELBE einzustellen. Zusätzlich wird noch der Einfluss des Substrates auf die Anstiegszeit des Detektorsignals diskutiert.

Contents

1. Introduction

Graphene is the two dimensional modification of sp^2-bonded carbon atoms, which form a purely two dimensional crystal lattice with a honeycomb structure. For a long time it was expected that these purely two dimensional lattices could not exist at room temperature as they would be destroyed by the lattice vibrations. Therefore it was surprising that Novoselov and Geim presented the production of small graphene flakes and demonstrated outstanding properties like the anomalous quantum Hall effect [1, 2]. For this work they were awarded with the Nobel Prize for physics in 2010. Zhang et al. also published measurements on the quantum Hall effect in graphene at the same time [3]. In the first part of this chapter a short overview over the outstanding features of graphene will be given besides a closer look at the optical properties, especially in presence of a magnetic field. In the second part different ways of the production of graphene are introduced.

1.1. Properties of graphene

Graphene consists of a hexagonal lattice with two carbon atoms per unit cell (see also Fig. 1.1). The lattice constant of this purely two dimensional crystal is $1.42\,\text{Å}$. Due to this unique structure, graphene exhibits many outstanding features. Three electrons per atom form very strong covalent σ-bonds, which leads to an extreme stiffness in the lattice direction. The stiffness of suspended graphene was measured with an atomic force microscope [4,5], where a Young's modulus of up to $1.0\,\text{TPa}$ was extracted. This in plane stiffness is connected to a very high thermal conductivity. From this point of view graphene could be a very prominent candidate as a new, very strong and light weight material. In the following part of the thesis the optical and electronic properties are discussed.
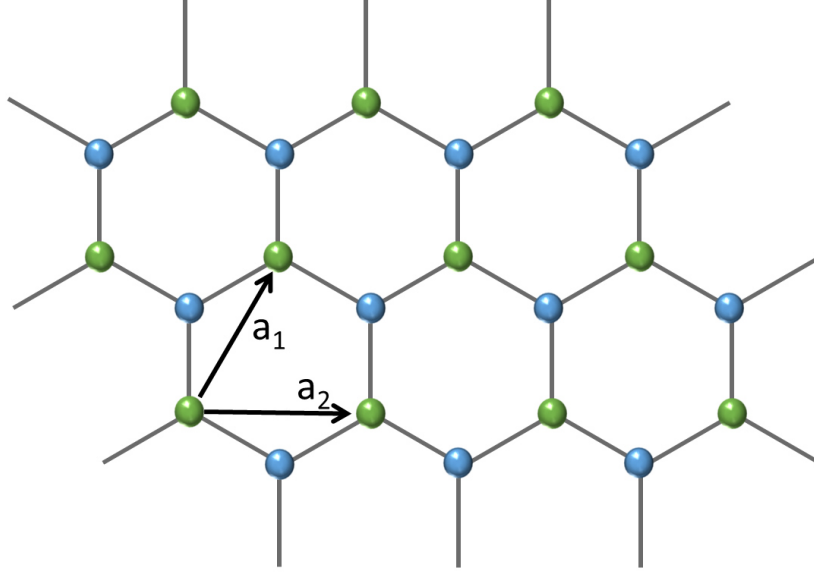
Figure 1.1.: Hexagonal crystal lattice of graphene, green and blue colored are the two sublattices resulting from the two atoms per unit cell. a_1 and a_2 are the two basis vectors.

1.1.1. Electronic properties

In contrast to the mechanical properties of graphene, the electronic properties result mainly from the π electrons. The unique spatial structure of graphene induces also unique electronic properties. The band structure of graphene was already calculated by Wallace in 1947 [6]. Within the tight-binding model with nearest-neighbor approximation he calculated the energy dispersion to be

$$E = \pm\sqrt{\gamma_0^2(1 + 4\cos^2(\pi k_y a) + 4\cos(\pi k_y a)\cos(\pi k_x \sqrt{3}a))}. \tag{1.1}$$

In this equation, γ_0 is the nearest-neighbor hopping energy and a is the lattice constant. The band with the negative energy represents the valence band, the positive sign indicates the conduction band. In Fig. 1.2 (a), the structure of the conduction band is depicted, the valence band is exactly symmetric with negative sign. Including the next-nearest neighbor, this symmetry is broken and the valence band gets flattened for very large negative energies. Most prominent in the picture of the bandstructure is the fact that valence and conduction band do not overlap, but touch in several points. These points are called K- and K'-points or Dirac points. For low energies, close to the Dirac points, the dispersion relation is linear
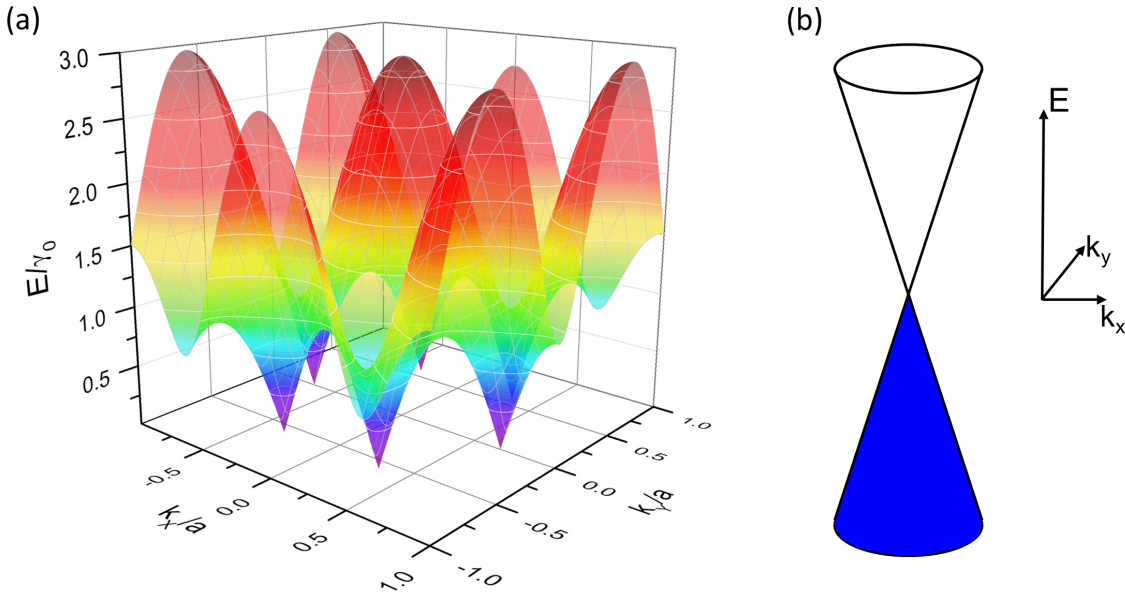
Figure 1.2.: (a) Bandstructure of the conduction band in graphene, calculated by Eq. 1.1. (b) Detail of the bandstructure at low energies where conduction and valence band touch in the K-point.

and forms two opposing cones, the so called Dirac cones (see also Fig. 1.2 (b)). This linearity can be expressed as

$$E = v_F \hbar \Delta k, \tag{1.2}$$

where $v_F \approx 10^6$ m/s is the constant Fermi velocity (e.g. [7]) and Δk is the momentum relative to the K-point. In comparison with the energy-momentum relation

$$E = \sqrt{(pc)^2 + (mc^2)^2} \tag{1.3}$$

one can see that the carriers in graphene behave like mass-less particles [8]. This unique feature opens up the possibility to investigate the equivalent form of relativistic particles, e.g. via optical or transport measurements.

Close to the Dirac points, the density of states can be approximated by the equation

$$\rho(E) = g_s g_v \frac{1}{2\pi\hbar^2} \frac{|E|}{v_F^2}. \tag{1.4}$$

The four-fold degeneracy of graphene, which arises from a two-fold degeneracy from the electron spin and an additional two-fold degeneracy from the two Dirac

points (K and K'), is taken into account by g_s and g_v, respectively. This means that the density of states is zero at the Dirac point, and linearly increasing with energy.

Furthermore, the carrier mobility in graphene is extremely high: A mobility of up to $230000\,\mathrm{cm^2V^{-1}s^{-1}}$ was reported in suspended graphene samples [9], measured at low temperatures. In comparison, the mobility of electrons in Si is far below the values for graphene ($20000\,\mathrm{cm^2V^{-1}s^{-1}}$ at low temperature [10]). Furthermore, the mobility in graphene remains very high at elevated temperatures [11], therefore graphene is discussed as replacement material for silicon as it allows one to build significantly faster transistors. Wu et al. [12] demonstrated the large scale production of graphene-based field-effect transistors with a cut-off frequency of $155\,\mathrm{GHz}$. Although these transistors show their potential in high frequency applications, e.g. radio frequency amplifiers, it is not straight forward to use these transistors for digital devices like processors. As graphene has no bandgap, the conductivity can not be suppressed as efficiently as compared to devices based on silicon. Furthermore, the mobility of the carriers is highly dependent on the Fermi energy of the graphene. When graphene is highly doped and the Fermi energy is increased the mobility is strongly quenched (e.g. [13]).

1.1.2. Optical properties

Due to the gap-less nature, graphene is able to absorb photons via interband absorption within an extremely wide spectral range from the ultraviolet to far-infrared radiation. Moreover, the linear dispersion results in a constant absorbance of $2.3\,\%$. This value is only defined by the fine-structure constant α [14] and can be calculated to be $\pi\alpha = 2.3\,\%$. However, interband absorption is suppressed in doped graphene for photon energies below twice the absolute value of the Fermi energy (see Fig. 1.3 (b)). In this case, phonon-assisted intraband absorption can be much stronger than the interband absorption [16]. The interplay between interband and intraband absorption can be identified via calculations of the real part of the dynamic conductivity [15, 17]. It is given by

$$
\begin{aligned}
Re[\sigma(\omega)] =& \frac{8\sigma_0\tau_m k_B T_{el}}{\pi\hbar(\omega\tau_m + 1)}\ln[2\cosh(-E_F/2k_B T_{el})] \\
&+ \frac{\sigma_0}{2}\left[\tanh\left(\frac{\hbar\omega + 2E_F}{4k_B T_{el}}\right) + \tanh\left(\frac{\hbar\omega - 2E_F}{4k_B T_{el}}\right)\right],
\end{aligned}
\tag{1.5}
$$

6

where $\sigma_0 = e^2/4\hbar$ is the universal value of the dynamic conductivity [18], T_{el} is the electron temperature and τ_m is the momentum relaxation time. The contribution of the absorption that is caused by intraband processes is described by the first summand while interband absorption is represented by the second summand. Results for calculations with $E_F = 13\,\text{meV}$ and $\tau_m = 300\,\text{fs}$ at various electron temperatures are plotted in Fig. 1.3 (a). In this plot one can see that absorption via phonon-assisted intraband processes dominates in the low-energy region. Interband absorption causes the flat contribution for higher photon energies, which represents the constant absorbance of 2.3 %. The upper energy limit of this constant absorption is about 2.5 eV, as for higher energy the bandstructure deviates from the linear dispersion.
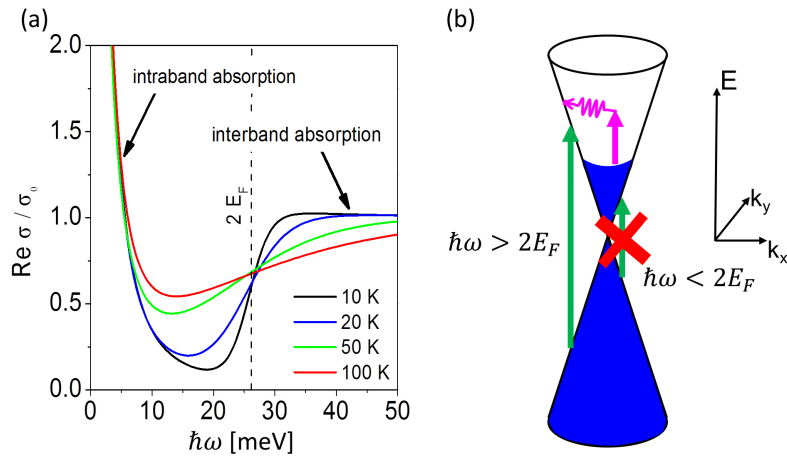
Figure 1.3.: (a) Real part of the dynamic conductivity of a single graphene layer for different temperatures. Interband absorption is dominating in the flat part for higher energies, for lower energies the intraband absorption strongly increases. The dashed line indicates twice the Fermi energy. Modified version of Fig. 7 (b) in [15]. (b) Bandstructure of graphene with a positive Fermi energy. While high energy photons can be absorbed via interband processes (green arrow), these transitions are blocked by Pauli blocking for low photon energies. The pink arrow indicates the phonon assisted intraband absorption.

The high carrier mobility, combined with broadband absorption makes graphene a highly promising material for electro-optic devices like detectors from the near-infrared range [19] to the THz range [20]. Graphene can also serve as attractive material for nonlinear optics, e.g. as saturable absorber for mode-locked lasers [21], in a wide spectral range. Strong plasmonics effects in graphene in the infrared

range [22] can be used for example to build tunable absorbers for the far-infrared range [23].

Even though the absorption of 2.3% is very high considering the fact that it is only one atomic layer thick, the high transparency makes it attractive as an electrode material for displays, touch screens or solar cells [24]. Compared to other electrode materials which are mainly used today, like indium tin oxide, their is no rare material needed for the production of graphene. Most importantly, graphene as electrode material allows one to build flexible displays.

1.1.3. Graphene in magnetic fields

As the carriers in graphene act like relativistic particles, the Landau level spectrum differs strongly from the one of conventional two dimensional electron gases with parabolic band structure. In a system with a parabolic band structure the Landau level energy can be calculated by $E_n = \hbar \omega_c (n + 1/2)$. Here n represents the index of the Landau level (LL), ω_c is the cyclotron frequency defined by $\omega_c = eB/m^*$, with the effective mass m^*. This leads to an equidistant LL spectrum, where the level spacing is proportional to the magnetic field.

In contrast to this, in graphene the energy of each Landau level is determined by $E_n = v_F \sqrt{e\hbar Bn}$ [25], where v_F represents the Fermi velocity. The energy of each Landau level is proportional to the square root of its index as well as the square root of the magnetic field. This leads to a very prominent feature of graphene, the anomalous quantum Hall effect [2]. Here the Hall plateaus are shifted compared to the Hall plateaus of a conventional two dimensional electron gas. But even more important for this thesis is the opportunity to address single LL transitions within the LL spectrum of graphene by choosing the proper wavelength. This enables one to measure the dynamics of a distinct LL transition via pump-probe measurements. More details of the Landau level spectrum can be found in Sec. 4.1.

1.1.4. Raman spectroscopy of graphene

Raman spectroscopy is a very versatile measuring technique to investigate the properties of a graphene sheet. Most important for the scope of this thesis is the possiblity to distinguish uncoupled graphene layers from coupled layers which behave like bilayer graphene or graphite [26]. Also the density of defects in the graphene sheet can be revealed by Raman spectroscopy [27], by comparing the characteristic

8

Raman peaks of graphene. Das et al. showed that even the doping of a graphene sheet can be monitored by Raman spectroscopy [28]. Also the strain in a graphene layer can be probed by Raman spectroscopy [29, 30].
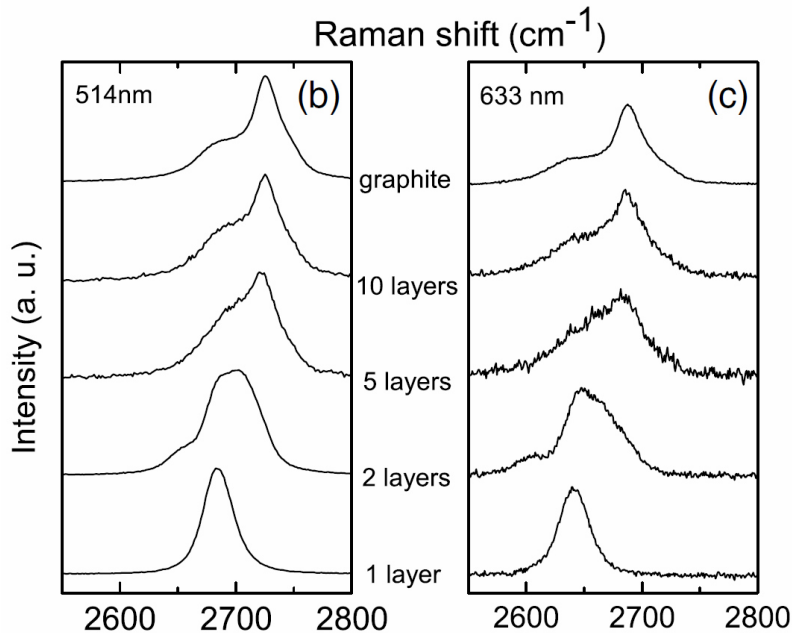
Figure 1.4.: Raman spectra of the $2D$-peak of graphene samples with different num-
ber of coupled graphene layers, measured with different laser sources.
Figure taken from [26] [1].

The main features of a Raman spectrum of a perfect graphene sheet are the G-peak at about $1580\,\mathrm{cm}^{-1}$ and the $2D$-peak at about $2700\,\mathrm{cm}^{-1}$. These two peaks stem from the efficient coupling of the electrons to the optical phonons with the highest energy on the Γ- and on the K-point, respectively. The G-Peak represents the Raman excitation of the highest optical phonon at the Γ-point. As the momentum of this phonon is zero, a direct coupling to a single photon is possible. In contrast to this, the optical phonon on the K-point has a very large momentum, so two phonons are needed to keep the resulting momentum at zero. As two of these phonons are involved, the resulting peak is labeled $2D$-peak. From the shape of this $2D$-peak, the number of coupled graphene layers can be estimated. A single layer of graphene has a Lorentz-shaped peak, while the $2D$-peak of a bilayer consists of a superposition of three different peaks. With rising number of coupled graphene layers the $2D$-peak is

---

[1]Reprinted figure with permission from A. C. Ferrari, J. C. Meyer, V. Scardaci, C. Casiraghi, M. Lazzeri, F. Mauri, S. Piscanec, D. Jiang, K. S. Novoselov, S. Roth, and A. K. Geim, Physical Review Letters, 97, 187401, 2006. Copyright (2006) by the American Physical Society.

changing to a peak with a prominent shoulder on the low-energy side, known from graphite (see also Fig. 1.4).
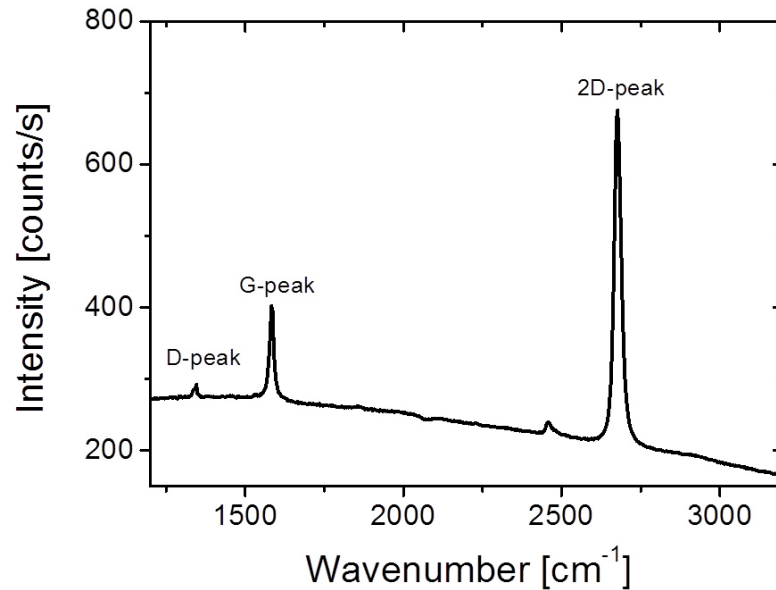
Figure 1.5.: Raman spectrum of a graphene flake used as detector material (see also Chapter 5).

With increasing number of defects in graphene, the momentum conservation of the scattering processes gets weakened, giving rise to the D-peak at $1350\,\mathrm{cm}^{-1}$. The ratio between the G-peak and the D-peak is a direct measure of the number of defects in the graphene sheet under investigation. In Fig. 1.5 a Raman spectrum of a graphene flake on SiO_2 is depicted. The two main peaks in the spectrum are the G-peak and the $2D$-peak, the small peak on the left side is the defect induced D-peak. The broad background signal is caused by a gold contact, which is next to the measured spot on the graphene flake.

1.2. Synthesis of graphene

After the discovery of the outstanding features of graphene, which can be used in many different fields, a great effort has been spent to find ways to produce high quality graphene on large scale. Meanwhile a large variety of methods exists that can produce graphene on different levels of structural quality and size. In the following subsections, the three methods for production of the graphene samples used in this thesis, namely mechanical exfoliation of graphite, thermal decomposition of SiC

and chemical vapor deposition, are presented. Apart from these methods that have been well established for almost 10 years, a number of potential mass production methods have been introduced recently. One example is the liquid-phase exfoliation of graphite [31]. Graphite is put into a solvent that separates the single atomic layers, which results in flakes of single layers of graphene in the solvent. A more chemical pathway to the graphene production is the reduction of graphite oxide [32]. The chemical reduction of graphene oxide can even be combined in an inkjet printer, which allows the direct patterning of reduced graphene oxide to the desired substrate [33]. A nice overview of different techniques to produce graphene is given in [34].

1.2.1. Mechanical exfoliation of graphite

This very simple method of the production of small graphene flakes was utilized for the first Hall measurements published by Novoselov et al. [1]. A sticky tape is pressed on a piece of graphite, usually highly ordered pyrolytic graphite (HPOG). After the mainly used sticky tape this method is also called "scotch-tape method". When the sticky tape is peeled off from the graphite, a thin layer (many atomic layers) of graphite is separated from the graphite and sticks on the tape. Now the tape is pressed several times onto another sticky tape to reduce the thickness of the remaining graphite on the tape. When the thickness is reduced strongly, the tape is pressed onto the desired substrate, in most cases SiO_2 on Si is used. This substrate has two main advantages: On the one hand one can identify flakes which consist of a single layer of graphene with a simple optical microscope if the SiO_2 has the correct thickness (e.g. 275 nm) [35]. On the other hand one can easily control the level of the Fermi energy in the flake by gating via the Si substrate (back-gating). To this end, doped Si is required.

The size of flakes produced by this method is usually in the range of $10\,\mu$m. Although this is very small, this method is widely used. The flakes contain only few defects, which can be seen in Raman spectra by a very small contribution of the defect induced D-peak. In the context of this thesis this type of graphene is used for the development of graphene-based detectors (see Chapter 5). The Raman spectrum of a flake used for the detectors can be seen in Fig. 1.5.

1.2.2. Thermal decomposition of silicon carbide

In contrast to the mechanical cleavage of graphite, thermal decomposition of SiC [36] allows one to produce wafer size graphene [37]. For this a wafer of SiC is heated up above 1300 °C. This can be done under ultra high vacuum, or under an inert atmosphere like argon. The silicon is evaporating from the SiC, the remaining carbon forms layers of graphene. Although the graphene layers are formed by the remaining carbon, this method is also often called "epitaxial growth". The hexagonal SiC has a wurtzite structure, where the (0001)-oriented surface of the wafer is Si-terminated, the (000-1)-oriented one is C-terminated. Due to the different composition at the surface of these two sides, the growth of the graphene differs strongly: On the Si-terminated side in the beginning of the process a buffer layer is formed [38]. This buffer layer has already the atomic structure of the desired graphene, but it is covalently bound to the substrate. Therefore this layer does not behave graphene like, e.g. it is insulating. After some more time a new layer grows below the buffer layer. This new layer builds a new buffer layer while the old buffer layer gets electronically decoupled from the new buffer layer and therefore behaves like graphene. As the growth on this side of the SiC is quite slow, the process can be stopped after a high coverage of the wafer with a single layer of graphene is achieved. Growing for a longer time leads to the formation of coupled layers of graphene, so called bilayers and trilayers. Finally, when this method is continued for a long time, graphite is produced. Another way to grow a single layer of graphene that is not coupled to the substrate is to stop the growth after the formation of the buffer layer. Via the intercalation of hydrogen, it is possible to release the buffer layer and obtain a single layer of quasi-free standing graphene [39]. By patterning the substrate material, it is possible to directly grow single-layer graphene in nanostructures, e.g. for an array of transistors [40].

The growth characteristics on the C-terminated side is completely different. A buffer layer like on the Si-terminated face does not exist, the first layer of carbon atoms is not coupled to the substrate. As the layers grow very fast on this side it is not easily possible to produce a single layer of graphene on a large scale. This is caused by the fact that in some regions the graphene formation did not start, while in others already several layers are grown. In contrast to the layers grown on the Si-terminated side, on the C-terminated side the layers are electronically decoupled when a multilayer stack is grown. Each layer is rotated by roughly 30° against the neighboring ones [41].

12

The quality of the grown graphene is strongly dependent on the number of defects in the lattice of the SiC and the flatness of the surface. e.g. screw dislocations lead to defects in the graphene lattice. Hydrogen etching can strongly improve the surface flatness a lot and therefore enhance the grade of the graphene. During the last years the quality has increased strongly, so this method might be interesting to develop electronic devices based on graphene. Up to now the substrate prices for semi insulating SiC is very high ($\approx$ 2500 Euro for a 3" wafer). A recent overview about graphene grown by the thermal decomposition of SiC is given by Sprinkle et al. in [42].

The uncoupled multilayer samples grown on the C-terminated side are very interesting, in particular for spectroscopic purposes. The signal is strongly increased compared to the signal of a single-layer sample, while the sample still keeps it single-layer characteristics. Furthermore this type of graphene features a large number of almost intrinsic layers, which enables the investigation of interband transitions at low photon energies. Only a few layers at the interface to the SiC substrate are highly doped. The first layer is characterized by a Fermi energy of about 300 meV, which is caused by charge transfer from the substrate to the graphene and precludes the investigation of interband transitions at low photon energies (cf. Sec. 1.1.2). Such a charge transfer is observed for practically every substrate material. For the subsequent graphene layers, the Fermi energy is strongly decreased down to the range of 10 meV [15, 43]. In the scope of this thesis mainly samples of this type were used. They were grown by the group of Walt A. de Heer at the Georgia Institute of Technology.

1.2.3. Chemical vapor deposition

In 1991, Land et al. [44] demonstrated the growth of very small flakes (about 2 nm) of "graphite monolayers" by chemical vapor deposition (CVD) on Pt. This technique, the CVD growth of graphene on metal films, has been strongly improved over the last years. A metal is heated up to temperatures of about 1000 °C and brought into contact with carbonaceous gas like methane. At this high temperature the molecules of the gas are decomposed and the carbon is adsorbed or absorbed by the metal. Cooling down the metal to about 800 °C leads to a strong decrease of the solubility of carbon in the metal. The carbon leaves the bulk metal and forms graphene on the metal surface. Sutter et al. demonstrated the growth of graphene monolayers on single crystalline ruthenium with domain sizes of about 200 μm by

this method [45]. Other metals like platinum [46] or iridium [47] can also be used to obtain high quality graphene. A commonly used metal for the production of CVD graphene is copper. The solubility of carbon in the hot copper is very low, therefore the graphene grows directly as a single layer in a self limiting process [48]. Compared to the growth on ruthenium or iridium, the graphene grown on copper has more defects and smaller domain sizes, but it is easy to produce and cheap.

For most applications metals are not suitable substrate materials. To build electronics from graphene, an insulating substrate is needed, for spectroscopy a transparent one is preferred. Therefore it is necessary to transfer the graphene to a different substrate. A special sticky tape that loses its adhesive properties above $80\,°C$ can be used for this. After pressing the sticky tape onto the graphene the metal can be etched away. The sticky tape with the graphene can then be applied to the desired substrate. By heating the substrate the sticky tape can be removed and the graphene stays on the surface of the new substrate.

Due to the mechanical work during the transfer process many defects are induced to the graphene. Samsung demonstrated a sheet of graphene on synthetic material with a size of 30" [49]. This large-scale graphene features a high defect density, nevertheless it is well suited for applications such as electrode material for bendable displays or solar cells.

2. Samples and experimental techniques

In the following chapter, firstly the samples used for the spectroscopic investigations are described. Secondly, a route to the production of multilayer epitaxial graphene with the high-temperature oven, available at the HZDR, is shown. In the last part of this chapter, the experimental technique which is used for most of the spectroscopic measurements, as well as the basics of the data analysis are presented.

2.1. Multilayer epitaxial graphene

2.1.1. Samples for the measurements

The samples used for the spectroscopic measurements are produced by thermal decomposition of SiC, as it is described in Sec. 1.2.2. Three different samples, namely with 40 layer (sample name: 7D8), 50 layers (MEG 30 TK) and 70 layers (7C2), have been grown on the C-terminated face of SiC at the Georgia Institute of Technology in the group of Walt de Heer. Orlita et al. demonstrated the graphene like nature of the multilayer samples by magneto-spectroscopy experiments [7,50]. Within the scope of Fabian Göttfert's diploma thesis [51], the samples were investigated via Raman spectroscopy at $532\,\mathrm{nm}$, which also predominantly revealed a single-layer behavior of the samples. Normalized spectra for each of the samples are depicted in Fig. 2.1. The signature in the tails of the G-peak at around $1600\,\mathrm{cm}^{-1}$ originate from the SiC substrate. The $2D$-peak at around $2700\,\mathrm{cm}^{-1}$ shows a Lorentzian shape for most positions on all three samples, which identifies the single-layer characteristics. At the D-peak position at $1350\,\mathrm{cm}^{-1}$, only very small peaks can be observed, which indicates a low number of defects within the samples. At few positions on all samples, signatures of coupled multilayers could be found at the $2D$-peak. Hence, in all measurements, a part of the signal might be caused by coupled multilayers.
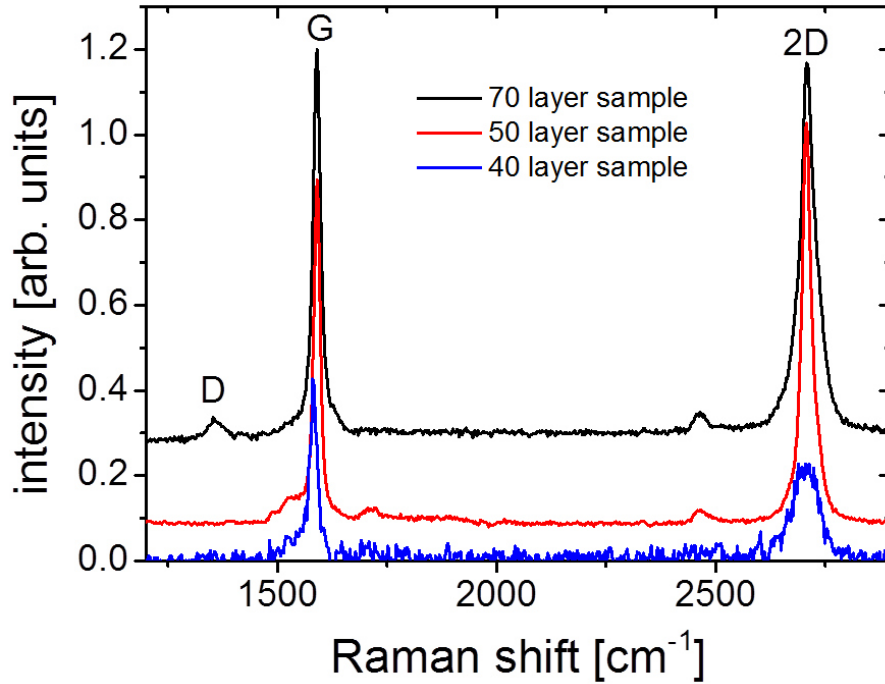
Figure 2.1.: Typical Raman spectra of the three different multilayer samples measured at 532 nm.

While a large part of the graphene layers of such a multilayer sample is quasi intrinsic, which means that the Fermi energy is in the range of several meV, the graphene layers at the interface to the SiC substrate are highly doped (cf. [15, 43]). While for most parts of this thesis only the quasi intrinsic layers are of interest, a closer look on the highly doped layers is taken in Sec. 3.3.2 and Sec. 4.2.

2.1.2. In-house production of multilayer epitaxial graphene

Besides the spectroscopic measurements on the multilayer samples from the Georgia Institute of Technology, it has proven very useful for us to have the ability to grow these samples on our own. On the one hand, it is not only interesting for the measurements of the carrier dynamics of graphene, but also it is useful to have some samples as reference in other pump-probe measurements, e.g. to optimize the alignment on a known sample before measuring unknown systems. On the other hand, the possibility to grow many, very similar samples, would enable one to study the influence of defects on the relaxation dynamics. To this end, different samples could be irradiated at the Ion Beam Center with various ions and energies. An

investigation of the dependence of the relaxation time on the number of defects could reveal the role of defects for carrier-phonon scattering. Furthermore, it was initially intended to use this type of graphene for the development of graphene-based detectors.

As highly conductive SiC is much cheaper compared to semi-insulating SiC, a set of highly doped SiC wafers was bought to perform the first growth tests. A special SiC furnace from JIPELEC, which can heat up samples to 2000°C, was used to grow the samples. The samples are placed in a glossy-carbon susceptor, which is heated inductively at high frequency. It is possible to heat the samples under vacuum condition ($p < 10^{-5}$ mbar), as well as in Ar or N_2 atmosphere. A picture of the susceptor at a temperature of 1600°C, surrounded by the heater coil can be seen in the inset of Fig. 2.2.
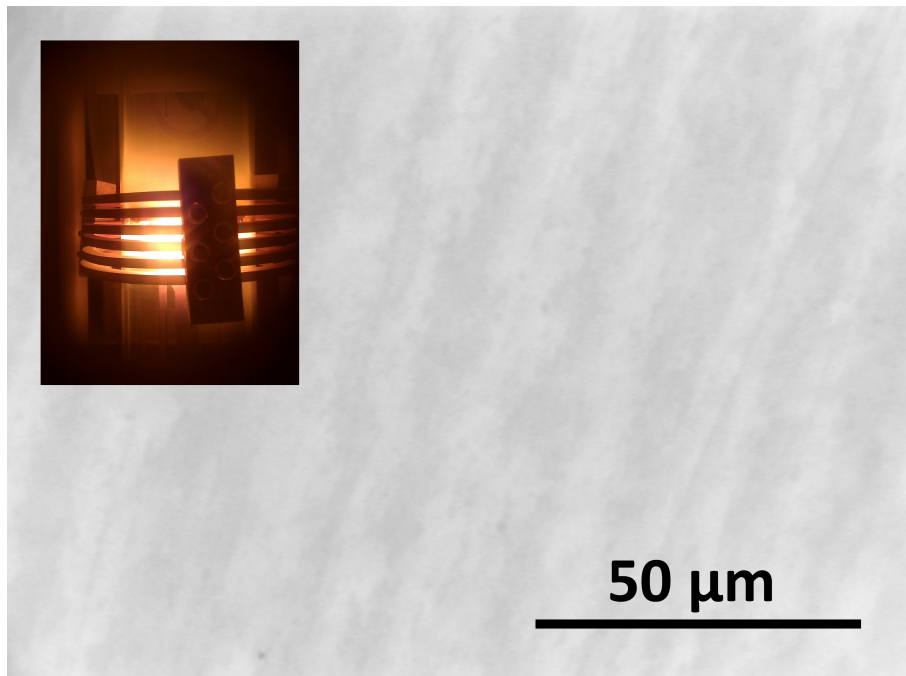
Figure 2.2.: Optical image of a multilayer epitaxial graphene sample. The different shades are caused by different number of graphene layers. A picture of the carbon susceptor at a temperature of 1600°C, surrounded by the heater coil, can be seen in the inset.

Usually the SiC is treated by H_2-plasma etching to get an atomically smooth surface [41]. As this process is not available at HZDR, and the sample quality was not very important for the first growth tests, all growth tests were performed with mechanically polished samples. Different growth tests were carried out under vacuum

and Ar atmosphere at atmospheric pressure. To determine the sample quality, the homogeneity of the graphene covering of the surface, as well as the height of the D-peak was taken into account. It turned out that the growth under Ar atmosphere had no positive effect on the graphene quality, but the growth was significantly slower. Hence, all further growth processes were performed under vacuum conditions. In a first step, the sample was heated to a temperature of 1200°C to remove oxides from the surface as well as for the annealing of the sample surface. It turned out that an annealing time of 10 minutes is reasonable to achieve high quality samples, a longer annealing time did not result in higher graphene quality. The main growth process was performed at temperatures between 1500°C and 1800°C. The best results for the highly conductive samples were obtained at a growth temperature of 1500°C. A large number of graphene layers are grown within 60 minutes. In Fig. 2.2, an optical image of the sample surface with the multilayers of graphene is depicted. The visible stripes in the pictures originate from different number of graphene layers, but the whole surface is covered by uncoupled graphene multilayers. A Raman spectrum of this sample is depicted in Fig. 2.3. The Lorentzian $2D$ peak verifies the graphene like behavior, the low height of the D-peak indicates a high quality of the sample. The spectrum looks the same for the dark and the light parts in Fig. 2.2. The detailed growth recipe for growing graphene in the present furnace is shown in Table 2.1.

Table 2.1.: Standard recipe for the growth of multilayer epitaxial graphene with the SiC furnace from JIPELEC.

step	temperature	duration
1	710°C	4 s
2	714°C	14 s
3	1200°C	35 s
4	1200°C	10 min
5	1500°C	35 s
6	1500°C	60 min
7	0°C	0 s (= switch off)

The samples grown on the highly conductive SiC were used for first tests of the metallization on top of the grown graphene for detector devices, as well as for pump-probe measurements in the near-infrared range. Although the metallization worked out very well, the devices were short-circuited by the substrate. In the pump-probe measurements, the home-grown samples showed comparable signals and relaxation
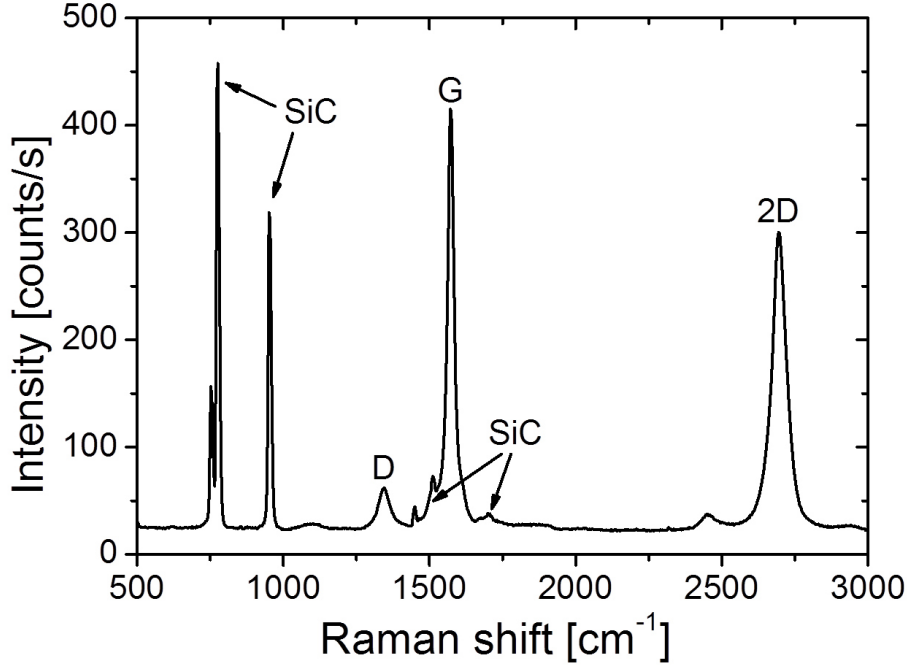
Figure 2.3.: Raman spectrum of a multilayer epitaxial graphene sample, grown at 1500°C for 60 minutes.

time as the samples grown at the Georgia Institute of Technology (see also Sec. 3.2). As the highly conductive substrate is only transparent for wavelengths below $5\,\mu$m, new samples were grown on semi-insulating SiC. Leaving all growth parameters the same, it was also possible to grow graphene on these samples on the whole surface, but the amount of grown layers was strongly reduced (the samples are a lot more transparent, which can be seen by the bare eye). To get samples with a comparable number of layers, either the temperature or the duration of the growth has to be strongly increased compared to the growth on highly conductive SiC.

2.2. Experimental techniques

2.2.1. Setup for pump-probe measurements

Pump-probe experiments are a very common tool for the investigation of carrier dynamics in solid-state systems (e.g. [52–55]). For single-color pump-probe experiments, an ultra-short laser pulse is split up into a strong pump pulse and a weak pulse for probing the system. Both pulses are brought to temporal and spatial overlap at the sample position. While the strong pump pulse is used to excite the sample,

the transmission of the probe pulse through the sample is measured as a function of the time delay between pump and probe pulse. This time delay is set by varying the optical path length of the probe beam with a mechanical delay stage. As the system relaxes back to its equilibrium state, the pump-induced change in transmission goes back down to zero. The temporal resolution is limited by the pulse duration of the laser system. In the case of graphene and large photon energies, electrons are mostly excited via interband transitions, therefore the transmission through the sample is increased due to bleaching of the transition (Pauli blocking). As some of the experiments require low temperature, the sample can be placed in a cryostat or in a magnet cryostat where magnetic fields of up to 8 T can be applied. In Fig. 2.4, a simple sketch of the pump-probe setup is shown.
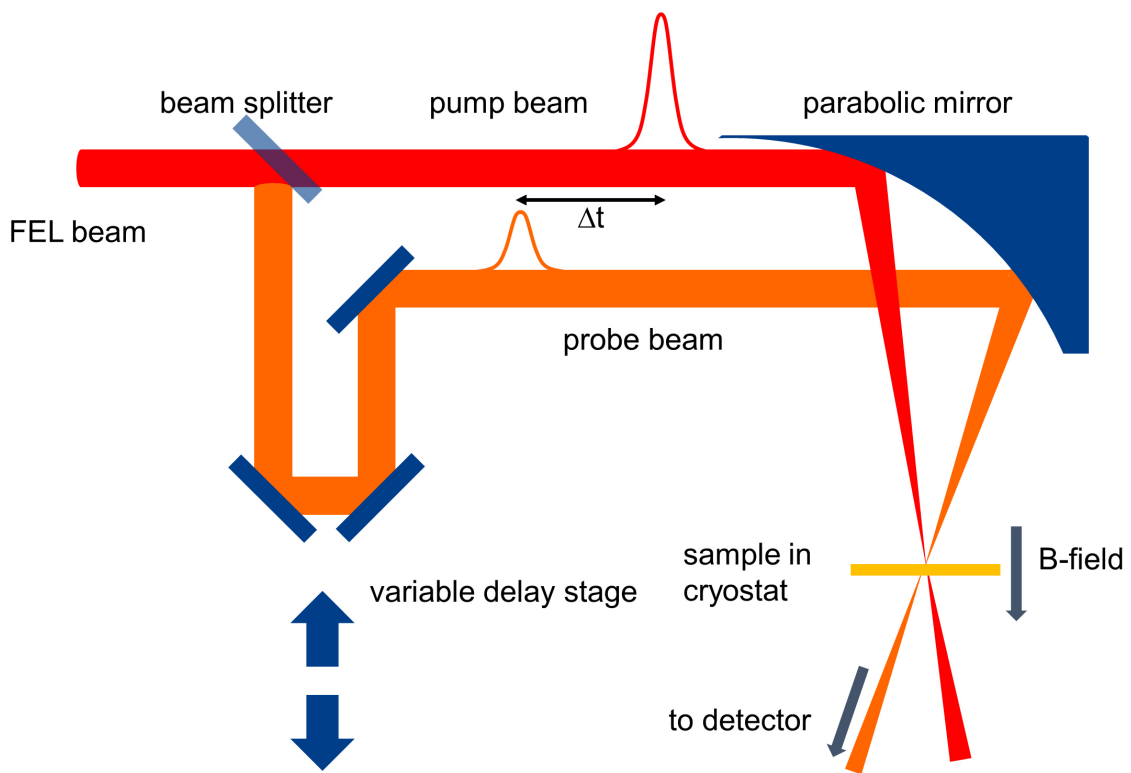
Figure 2.4.: Setup for single-color pump-probe measurements with the free-electron laser.

In the scope of this thesis, pump-probe experiments were performed in a wide spectral range, namely in the wavelength range from 800 nm to 88 μm. For the near infrared range, different Ti:sapphire lasers served as radiation source. The pulses exhibited a full width at half maximum (FWHM) between 30 fs and 50 fs

and a repetition rate of 78 MHz. The average output power at this wavelength was up to 800 mW. An optical-parametric oscillator (OPO), synchronously pumped by a Ti:sapphire laser, was exploited as radiation source for the wavelength range from $1.2\,\mu$m to $3.5\,\mu$m. The average output power of this system was limited to several tens of mW, the pulse duration was about 200 fs. More details on this laser system and two-color pump-probe measurements are given in section 3.3. For the measurements discussed in Sec. 3.2 and Sec. 3.4, slightly varied pump-probe setups were used, the variations of the setup are also described in these sections.

For investigations in the mid and far infrared range, the two free-electron lasers (FELs) FELBE at Dresden-Rossendorf were employed. A superconducting electron accelerator produces relativistic electron bunches with ps duration and a repetition rate of 13 MHz. These electron bunches pass the undulator of the FEL, which causes the emission of infrared photons. After one roundtrip through the cavity, the photons coincide with the next electron bunch. The photon pulse gains energy from the electron bunch as they pass the undulator together. A more detailed description of FELBE was published by Michel et al. [56]. With these FELs, the wavelength range between $5\,\mu$m and $250\,\mu$m is covered with an average output power of several W, corresponding to pulse energies up to the μJ range. The pulse duration varies between 1 ps at short wavelengths and 30 ps for wavelengths above $200\,\mu$m.

As the experiments were carried out in a wide wavelength range, different types of detectors were used to monitor the probe-beam intensity. Photodiodes based on Si and InGaAs were employed for the near-infrared range, while liquid nitrogen cooled mercury-cadmium-telluride detectors (HgCdTe, MCT) were used for the mid-infrared range. For even longer wavelengths, an extrinsic photoconductive Ge:Ga detector or a Si bolometer, both operated at liquid helium temperature, were utilized. To measure the pump-induced change of the transmission through the sample, the pump beam was modulated by a mechanical chopper. The frequency of the chopper was used as reference signal for a lock-in amplifier, which was connected to the detector.

In nearly all pump-probe experiments, the signal-to-noise ratio is reduced by scattered pump radiation: A part of the pump radiation that is scattered at the sample surface can reach the detector and cause an offset in the registered signal. The noise of this offset, which is caused by the noise of the laser source, yields an additional noise to the desired signal. Furthermore, interference between scattered pump radiation and probe radiation can cause strong fringes at the temporal overlap

of both pump and probe pulses. To suppress this scattered radiation, for most measurements the polarization of the pump beam was rotated by 90° with respect to the probe beam. Therewith, a polarizer was utilized to effectively suppress the scattered pump radiation at the detector position.

As the output power of the FEL can be very unstable, an additional beam splitter was included in front of the setup. With this, a small part of the FEL power was split off and measured with a pyroelectric detector to monitor fluctuations of the FEL power. For measurements with the FEL, this additional detector was also connected to a lock-in amplifier that was read out by the measurement software.

2.2.2. Data analysis

For all pump-probe measurements, different software based on Labview was used to control the mechanical delay stage, as well as the read-out of the lock-in amplifiers. The measured data are stored in ASCII files, which can be imported e.g. into Origin for the data analysis. The recorded detector voltage is proportional to the pump-induced transmission change ΔT, combined with an offset of the signal, caused by the scattered pump radiation. In a first step of the data processing, this offset is subtracted. For obtaining the relative pump-induced change in transmission $\Delta T/T_0$, a measure of the sample transmission T_0 in the absence of pumping is required. To this end an additional measurement of the detector signal with chopped probe beam and blocked pump beam is performed. With this additional information, the $\Delta T/T_0$ can be calculated.

The decay of practically all pump-probe signals obtained within this thesis can be described well by a bi-exponential decay. To extract the values for the relaxation times and the amplitude of the pump-probe signal, the function

$$\Delta T(t)/T_0 = A \cdot erf(t) \cdot (C \cdot e^{\frac{-t}{\tau_1}} + e^{\frac{-t}{\tau_2}}) \tag{2.1}$$

was fitted to the data. An error function $erf(t)$, which represents the excitation of the carriers, is combined with a bi-exponential decay. The scaling factor C accounts for the different size of the components decaying with τ_1 and τ_2 respectively, A is a scaling factor to fit the amplitude of the fit function to the signal. In Fig. 2.5 the pump-probe signal, measured at a wavelength of $16\,\mu$m, is depicted. The second peak in the data set arises from a multiple reflection of the pump pulse, probably from the outer window of the cryostat or the beam-line window. To include this
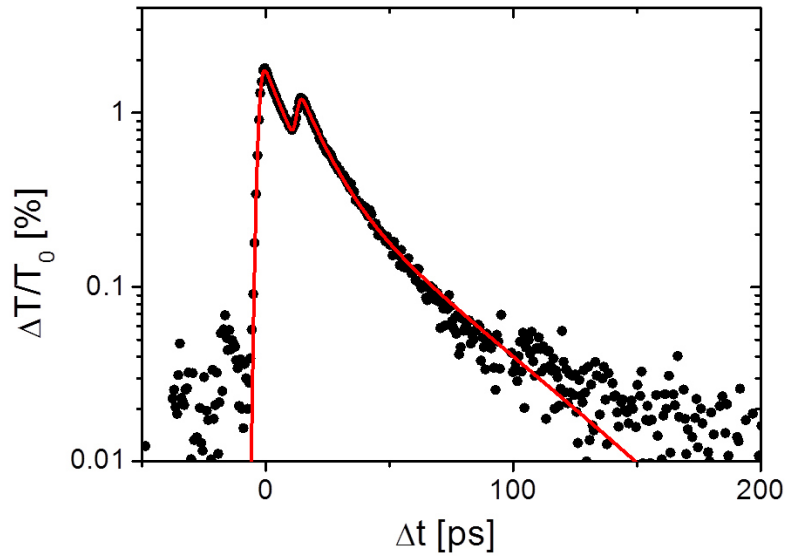
Figure 2.5.: Pump-probe signal measured at a wavelength of $16.5\,\mu$m with fit function (red line).

into the fit function, a second pump pulse is modeled by adding a second error function with a different amplitude but the same exponential decays as for the first pulse. The red line in Fig. 2.5 shows the fit function for a pump-probe signal with secondary pump pulse.

3. Carrier relaxation dynamics of graphene

The carrier relaxation dynamics is a very important property for the design of electronic, optoelectronic or optical devices. Also this dynamics can clarify the role of carrier-carrier and carrier-phonon scattering. This interplay has been investigated in graphene in the near infrared range excessively, while the mid and far infrared range was hardly explored. In the first section of this chapter, the current state of research is introduced. In the second section a study of the anisotropic carrier excitation by linearly polarized pump radiation is presented. The anisotropy of the carrier distribution around the Dirac cone is preserved during the carrier-carrier scattering processes until an isotropic carrier distribution is reached after 150 fs due to carrier-phonon scattering. Further single color and two color pump-probe experiments in the near-infrared range are discussed in the third section. In the last section, pump-probe experiments with very strong pump pulses, carried out in the far infrared range, are presented. While a strong negative pump-induced change in the transmission could be observed, the reason for this negative signal was found to stem from induced reflection of the sample.

3.1. Relaxation channels for hot carriers

Due to the widespread use of Ti:sapphire laser systems, the relaxation dynamics of graphene has been widely investigated via pump-probe measurements in the near-infrared range. As the number of different studies is very large, in the following only the most important ones for this thesis are discussed. Three different relaxation channels are important for the fast carrier relaxation in graphene: The first one is an ultrafast carrier-carrier scattering, which leads to a hot carrier distribution within a few tens of femtoseconds. The second one is related to an extremely efficient carrier-phonon scattering via the optical phonons in graphene. Carrier-phonon scattering

via acoustic phonons is a much slower process that becomes important at low energy.

The influence of the first two processes were revealed by two pump-probe studies by Dawlaty et al. [57] and Wang et al. [58]. They identified two different time constants, the faster one was attributed to carrier-carrier scattering and was found to be of the order of 100 fs. The slower time constant that was in the order of 2 ps and attributed to carrier-phonon scattering via the optical phonons. Furthermore, they could measure a strong decrease of the relaxation time for graphene samples containing more defects. Breusing et al. presented results of broad-band pump-probe experiments with ultra high temporal resolution of about 7 fs [59]. Spectrally resolved measurements of the pump-probe signal allowed to prove a hot distribution of the carriers within 30 fs. The influence of the Fermi energy of the graphene sample on the pump-probe signal was investigated by Sun et al. [60]. Furthermore, they could identify the doping of the highly doped graphene layers on the interface to the SiC substrate [43]. A more detailed description of the carrier-carrier and carrier-phonon scattering processes is given in the next section.

The third process, namely carrier-phonon scattering via acoustic phonons, was observed in a joint experiment-theory study. Pump-probe experiments were conducted in the spectral range from $5\,\mu$m to $125\,\mu$m [17]. In this paper, a strong increase of the relaxation time was shown, as soon as the photon energy is considerably below the energy of the optical phonon in graphene. The theoretical calculations revealed that even though the photon energy is far below the energy of the optical phonon, the main scattering process for the relaxation is carrier-phonon scattering via the optical phonon. This is possible, as due to the fast thermalization of the carriers, some carriers are highly excited into the conduction band. Besides the influence of the optical phonon, a third time constant of about 300 ps was attributed to scattering via acoustic phonons. In addition, a change in the sign of the pump-probe signal was shown, as soon as the photon energy is below twice the Fermi energy. In this case, interband excitation of the carriers is not possible due to Pauli blocking. Strong intraband absorption leads to a hot carrier distribution and the Fermi edge is smeared out, which enables interband absorption of the probe pulse and induced absorption occurs.

A first two-color pump-probe experiment, where the sample was excited by near-infrared radiation and probed with a THz pulse, was published by Paul et al. in 2008 [61]. A similar study was published by Choi et al. in 2009 [62], in both studies the relaxation times were in the ps range. Transient gain in the THz range is expected

26

in this type of experiments for high near-infrared pump power [63]. Experimental hints for this gain were published recently [64, 65]. The hot carrier distribution was also directly investigated by angle-resolved photon-emission spectroscopy very recently in two very similar studies [66, 67]. In [67], population inversion induced by interband carrier excitation could be observed.

In summary, it was possible to identify the three main relaxation channels of hot electrons via the large number of experiments in a broad spectral range. The fastest time constant (below 100 fs) is caused by electron-electron scattering which leads to a hot distribution of the carriers. Relaxation processes via optical phonons are in the time scale of several ps. As the energy of the optical phonons is very high (196 meV), the influence of the optical phonons decreases with increasing wavelength, resulting in prolonged relaxation times of about 20 ps. In the mid- and far-infrared range a third time constant (above 100 ps) can be observed, which is attributed to the scattering of the hot electrons with the acoustic phonons.

3.2. Anisotropy of excited carriers in momentum space

In most publications on carrier dynamics, the excitation of carriers in momentum space has been assumed to be isotropic. However, linearly polarized radiation leads to an anisotropic excitation of carriers in momentum space, which was already predicted in 2003 by Grüneis et al. [68] for graphite, but furthermore they assumed that it might be hard to measure this effect. Despite the large number of pump-probe experiments in the near-infrared range and the fact that this anisotropy of the carrier excitation was known that long, this effect was not shown in an experimental study. To close this gap, we performed pump-probe experiments in the near-infrared range with a temporal resolution below 45 fs. By varying the polarization of the pump beam, a strong anisotropy of the excited carriers was observed. Parts of this study have recently been published in [69] [1].

Theoretical studies of the anisotropic carrier excitation in graphene as well as of the scattering processes resulting in an isotropic distribution were recently published

---

[1]Fig. 3.3, 3.4 and parts (a) and (b) of Fig. 3.6 are reprinted with permission from M. Mittendorff, T. Winzer, E. Malic, A. Knorr, C. Berger, W. A. de Heer, H. Schneider, M. Helm, and S. Winnerl, "Anisotropy of excitation and relaxation of photogenerated charge carriers in graphene", Nano Lett. **14**, 1504-1507 (2014). Copyright 2014 American Chemical Society.

[70, 71]. The anisotropic excitation of the carriers in the momentum space with linearly polarized radiation is proportional to $|\sin\Phi_k|^2$. Here, Φ_k represents the angle between the momentum of the excited carrier and the polarization of the radiation. The resulting occupation probability ρ is depicted in Fig. 3.1, where the black line represents the carrier distribution caused by the pump pulse. Within approximately 10 fs after the pump pulse extremely fast carrier-carrier scattering leads to a hot carrier distribution while the distribution in momentum space remains anisotropic. The carrier distribution can only get isotropic via carrier-phonon scattering, which is predicted to take about 5 times longer. To observe this anisotropic carrier excitation, pump-probe measurements with an extremely high temporal resolution and varied pump and probe polarization are needed.
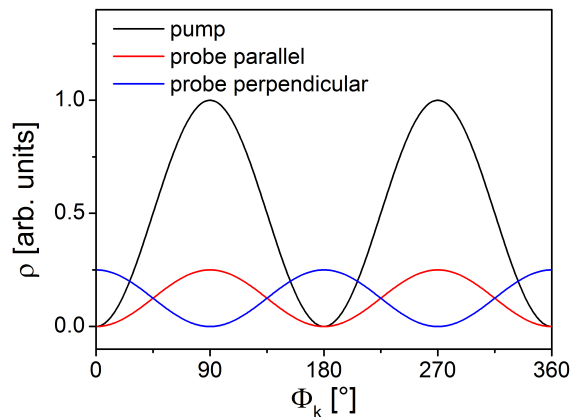
Figure 3.1.: Occupation probability as a function of the angle between the momentum of the excited carrier and the polarization of the pump radiation at an energy of $\hbar\omega/2$. The black line represents the carrier excitation caused by the pump pulse, the red (blue) line stands for the carrier excitation caused by probe radiation polarized parallel (perpendicularly) to the pump pulse.

To reach the temporal resolution required to observe this effect, a Ti:Sapphire laser (Femtosource scientific sPRO from Femto Lasers) with a minimum pulse duration of about 15 fs was used. As laser pulses with such a short pulse duration are linked to a very broad spectrum, dispersion of glass and air can stretch the pulse duration at the sample position significantly. Two chirped mirrors were used to prechirp the laser pulse in a way that the dispersion of the optical elements in the setup is roughly canceled out. Two half-wave plates were used to set the polarization of pump and probe beam. The pulse duration at the sample position was measured via second-harmonic generation in a β-barium borate crystal. To this end, the crystal

was placed at the sample position. In contrast to pump-probe measurements, the power of pump and probe beam was the same for this measurement. Furthermore, the detector was placed exactly in the center between pump and probe beam behind the crystal. At the temporal overlap of pump and probe beam in the crystal, photons of each of the beams can combine and a third beam in the center of pump and probe beam is formed. By changing the time delay between pump and probe pulse, the pulse duration can be estimated. In Fig. 3.2 the amplitude of the measured signal is depicted as a function of the time delay between pump and probe pulse.
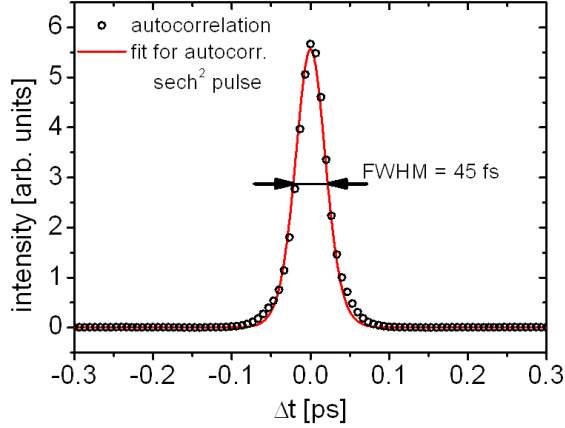
Figure 3.2.: Shape of the second-harmonic generation signal as a function of the time delay between pump and probe pulse. The red line indicates the fit function described by Eq. 3.1.

The pulse shape of a fs-laser pulse, generated by a Ti:sapphire laser, can be described by a sech^2 function. As the autocorrelation is the convolution of pump and probe pulse, the autocorrelation signal has the form of the convolution of a sech^2 pulse with itself [72]. This convolution can be expressed by

$$I_{\Delta t} = \frac{3}{\sinh^2\left(\frac{2.7196\Delta t}{\tau_{ac}}\right)} \left(\frac{2.7196\Delta t}{\tau_{ac}} \coth\left(\frac{2.7196\Delta t}{\tau_{ac}}\right) - 1 \right), \qquad (3.1)$$

where τ_{ac} represents the full-width at half-maximum (FWHM) of the signal shape. From the fit of this function to the measured data a FWHM of the autocorrelation signal of 45 fs can be estimated. From the width of the autocorrelation signal one can calculate the FWHM of the single pulse by dividing this value by 1.54, therefore the duration of a single pulse is about 30 fs.

To measure the anisotropic excitation of the carriers, pump-probe measurements were performed with horizontal polarization for pump and probe beam, named as

parallel configuration in the following. The perpendicular polarization was measured by rotating the half-wave plate in the pump beam to get vertically polarized pump radiation while the probe beam was kept horizontally polarized. For these measurements, the suppression of scattered pump radiation at the detector position is not possible with a polarizer. Hence, a very good spatial filtering of the probe radiation in front of the detector is required. Therefore, the probe beam was focused behind the sample with a lens that has a short focal length of about 30 mm. At the focus position, a pin hole was placed directly in front of the photo diode. Comparing the pump probe signals from the two different configurations should lead to different amplitudes and dynamics. In Fig. 3.3 (c), pump-probe signals are depicted for both configurations.
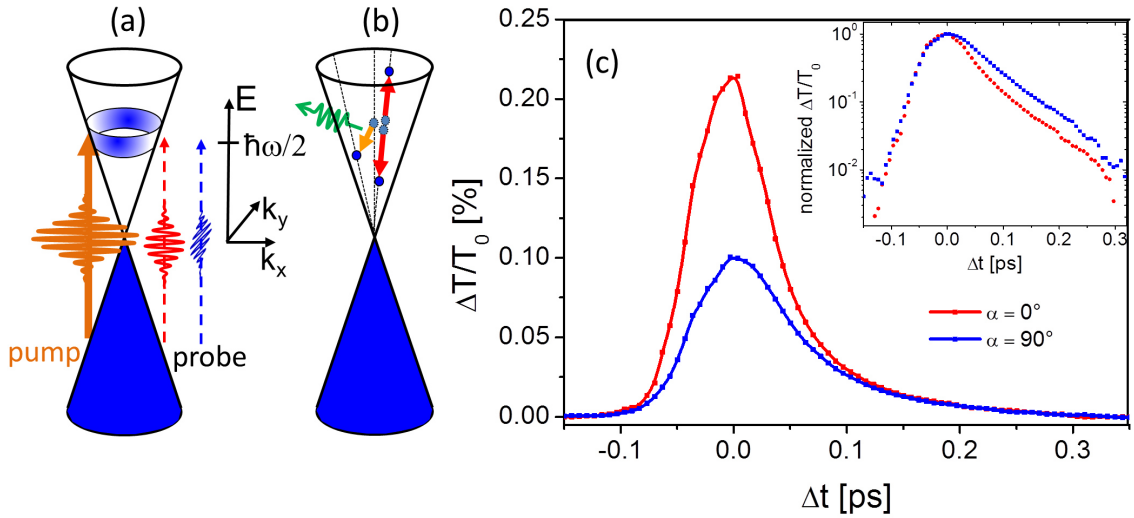
Figure 3.3.: (a) Band structure of graphene with anisotropic conduction band occupation induced by a linearly polarized pump beam. (b) Illustration of collinear intraband carrier-carrier scattering preserving both energy and momentum. (c) Pump-probe signals for parallel polarization configuration ($\alpha = 0°$) and perpendicular polarization configuration ($\alpha = 90°$). The dots and squares are experimental data, and the lines are guides for the eye. The inset depicts the same pump-probe data as in the main figure, but normalized and plotted on a logarithmic scale. Figure taken from [69].

The most obvious difference between parallel and perpendicular configuration is the signal amplitude, which is about 2.1 times larger for the parallel configuration. This difference can be explained by the overlap of the occupation probability of pump and probe radiation. The red (blue) line Fig. 3.1 stand for the carrier excitation

caused by parallel (perpendicularly) polarized probe radiation. A maximum overlap of pump and probe induced carriers is given for the parallel configuration, but even in the perpendicular configuration the occupation probabilities overlap which leads to the remaining signal.

After the pump-probe signals reach their maximum, both signals decay initially extremely fast. As the pulse is nearly symmetric in the time interval of -50 fs to 50 fs, the initial relaxation seems to be dominated by scattering processes with a time constant below the temporal resolution of the setup. During this initial relaxation, the difference between the signals for parallel and perpendicular polarization remains, which indicates the persisting anisotropy of the carriers. This can be explained by the extremely fast carrier-carrier scattering processes. To preserve energy and momentum conservation, these processes can only occur on straight lines on the Dirac cones. A simple sketch of carrier-carrier scattering is depicted by the red arrows in Fig. 3.3 (b). As these processes redistribute the carriers only along a straight line on the Dirac cones, the anisotropic carrier distribution remains. The larger signal relaxes slightly faster, which can be also seen in the inset of Fig. 3.3 (c). This difference in the decay is caused by carrier-phonon scattering processes which lead to an isotropic carrier distribution. To allow scattering processes which are not collinear on the Dirac cone, the emission of a phonon has to be included. This process is described by the yellow arrow in Fig. 3.3 (b). After about 150 fs both signals have the same amplitude, which means that an isotropic carrier distribution is reached. The overall relaxation time is for both signals approximately 65 fs. To verify the observed effects, additional measurements were carried out, which are discussed later in this section.

In Fig. 3.4 the amplitude of the pump-probe signal is plotted as a function of the polarization angle between pump and probe beam. The angle dependence of the signal amplitude should follow a convolution of the sine-square functions of the excited carriers of the pump pulse and the sine-square function of the carriers excited by the probe pulse. This convolution results in a cosine-square dependence of the signal amplitude. This dependence can be expressed by $1 + 2\cos^2(\alpha)$, where α is the angle between the polarization of pump and probe radiation. Hence, the maximum difference of the amplitude between perpendicular and parallel configuration can reach a factor of 3. As the temporal resolution of the experiment was limited, the measured ratio is only about 2. The red line in Fig. 3.4 is fitted to the measured data with this function. The error bars are estimated by the reproducibility of
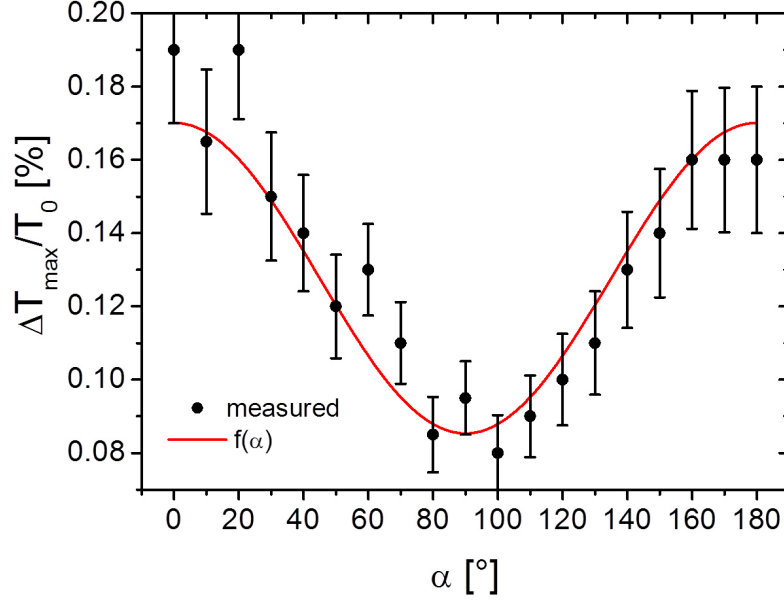
Figure 3.4.: Dependence of the amplitude of the pump-probe signal on the angle α between pump and probe-beam polarization. The fit function $f(\alpha)$ is described in the main text. Figure taken from [69].

the signal amplitude. At temporal overlap of pump and probe pulse, the scattered pump radiation interferes with the probe radiation at the detector position. This leads to strong interference fringes on the positive slope and the peak of the pump-probe signal. To suppress these fringes every measurement was repeated for 20 times. Despite these 20 repetitions, the influence of the fringes on the amplitude of the signal could not be completely eliminated. For direct comparison of parallel and perpendicular measurements, shown in Fig. 3.3, 30 measurements have been averaged to further minimize this error.

An additional significant difference between parallel and perpendicular configuration is the saturation behavior. In Fig. 3.5 pump-probe signals for different pump powers are depicted for parallel (a) and perpendicular (b) configuration. The amplitude of each signal as a function of the pump power is depicted in Fig. 3.5 (c). To get a measure of the saturation, a fit function [73] is fitted to the data. The fit function is given by

$$\Delta T/T_{max} = A_{sat} \cdot \frac{p/p_{sat}}{1 + p/p_{sat}}. \tag{3.2}$$

The saturation power p_{sat} indicates the power at which the amplitude of the signal

is quenched by 50 % and A_{sat} represents the maximum signal amplitude at which the full saturation is reached. The fitted functions are depicted as red lines in the insets of Fig. 3.5. For the parallel configuration the saturation power is $p_{sat} = 100\,\mathrm{mW}$, while for the perpendicular case it is about $300\,\mathrm{mW}$. This difference originates directly from the sine-square dependence of the carrier excitation in momentum space: Most carriers in momentum space are excited perpendicular to the polarization direction of the pump pulse (cf. Fig. 3.1). Therefore, in this region the saturation of the carrier excitation is strongest. This region of strongest saturation is most sensitively probed in parallel configuration as the carrier excitation follows the same sine-square function as for the pump pulse. Hence, the observed saturation of the pump-probe signal is strong. When the probe-pulse polarization is perpendicular to the pump pulse, the most sensitively probed region coincides with the lowest excited region in momentum space as the sine-square function for the excitation of pump and probe beam are shifted by 90°. This leads to a less pronounced saturation of the pump-probe signal. Notably, the saturation fluence found in this experiment ($7\,\mu\mathrm{J/cm}^2$) is far below the saturation fluence which was observed earlier in experiments and theory at the same wavelength ($0.65\,\mathrm{mJ/cm}^2$) [74]. A two-stage saturation characteristics that could explain the obtained results is subject of ongoing research.

The experimental results were complemented by microscopic calculations by Torben Winzer in the theory group of Ermin Malic at the Technical University of Berlin. In Fig. 3.6 the results of the calculations are shown. For the calculations, the same pulse duration, pump fluence and photon energy as in the experimental study were assumed. The results of the calculated pump-probe signals is depicted in Fig. 3.6 (b), and resemble the experimental results extremely well (cf. Fig. 3.3 (c)). The evaluation of the carrier occupation around the Dirac cone is shown in Fig. 3.6 (a). In contrast to the experiment, where a large part of the Dirac cone is probed, in the calculation one can observe the evolution of the occupation for a line in the k space selectively. While the occupation perpendicular to the polarization increases immediately, parallel to the polarization the occupation remains at zero first. As carrier-phonon scattering starts to become more important at higher occupations in perpendicular polarization, the occupation parallel to the polarization successively increases. The green dashed line represents the averaged occupation around the Dirac cone. In part (c) of Fig. 3.6, the calculated saturation characteristics, which describes the experimental findings very well, is depicted.

To ensure that the observed effects are not caused by any anisotropy of the sample,
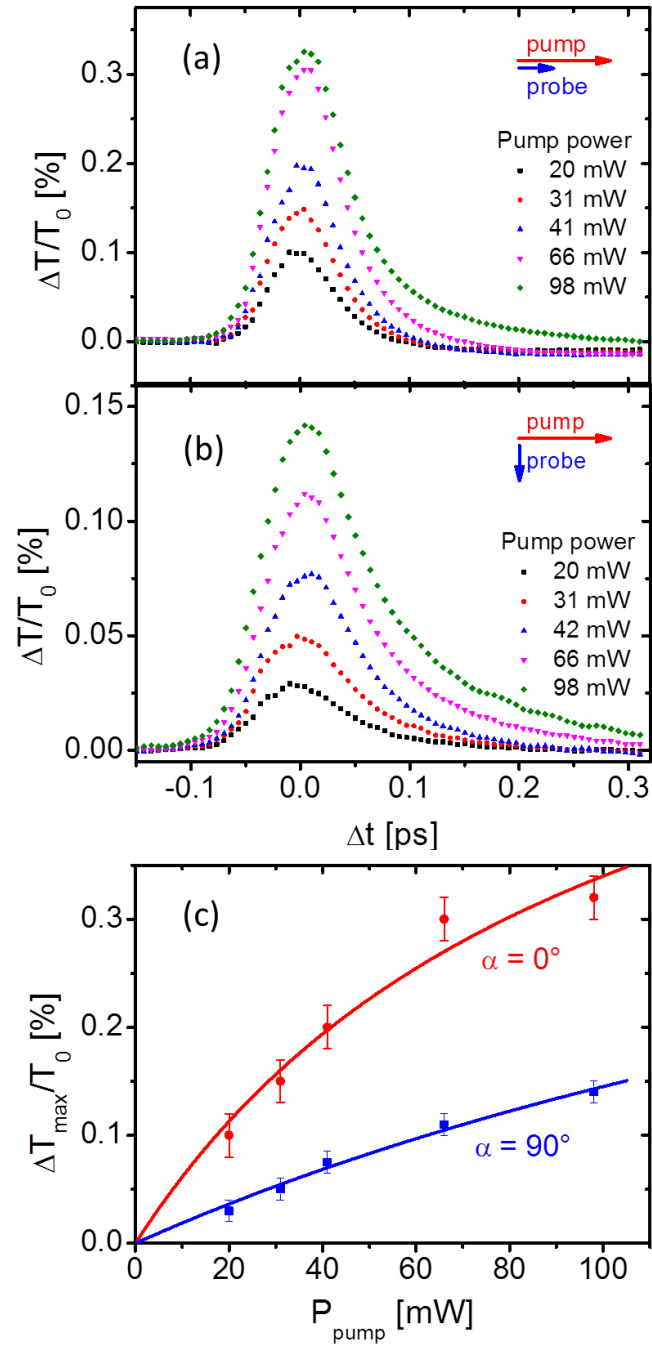
Figure 3.5.: Pump-probe signals for (a) parallel and (b) perpendicularly polarized pump and probe radiation at different pump power. The signal amplitude as a function of the pump power for both measurement configurations is depicted in (c).
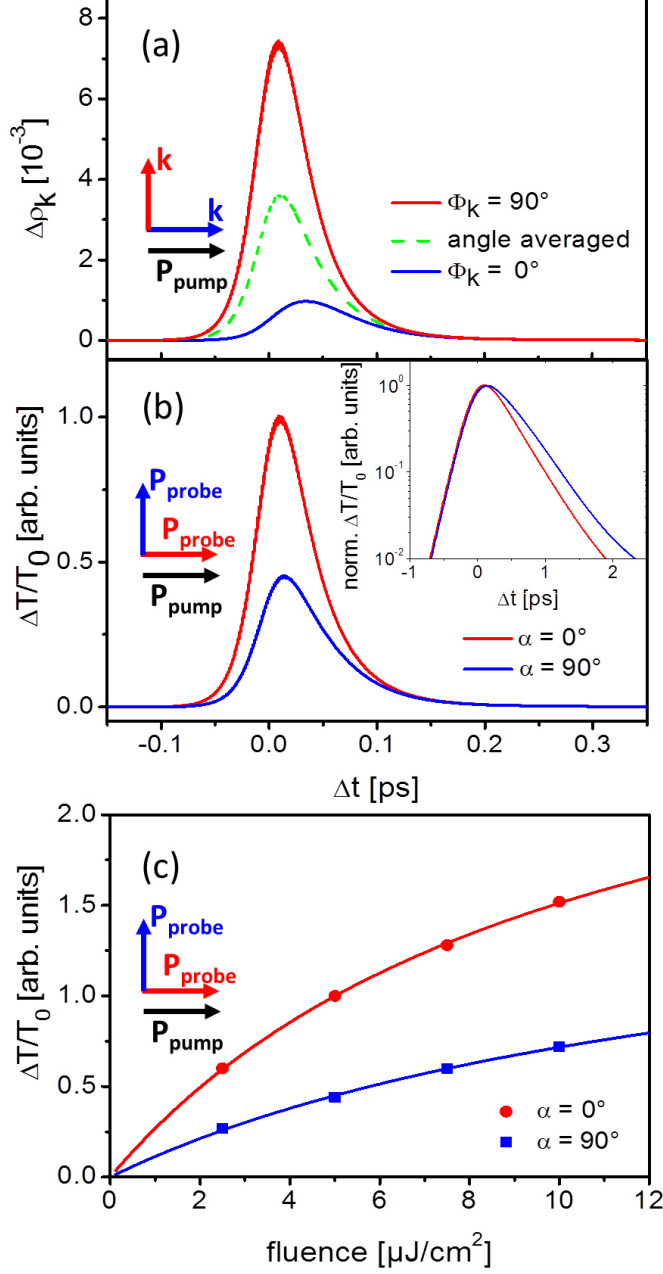
Figure 3.6.: (a) Pump induced occupation probability in k space at $\hbar\omega/2$ parallel (blue line) and perpendicular (red line) to the pump polarization as well as averaged around the Dirac cone (green dashed line). (b) Calculated pump-probe signals for pulse duration and excitation intensity like in the experiment for parallel (red line) and perpendicular configuration (blue). In the inset, the same data as in the main figure is plotted, but normalized and plotted on a logarithmic scale. (c) Signal amplitude of the calculated pump-probe signals as a function of the pump fluence for both configurations. Parts (a) and (b) are taken from [69].

a part of the measurements was repeated with rotated samples as well as with different samples. The results remained the same for all cases. Furthermore, the experiment was repeated with a sample which was grown in our own group to compare the performance of the home-grown graphene. The sample was grown as described in Sec. 2.1.2 on highly conductive SiC. As these substrates are only transparent in the near-infrared range, this sample could not be used for experiments in the mid and far-infrared range. Therefore polarization dependent measurements in the near-infrared range are an ideal "playground" to test the samples. The results of the pump-probe measurements in perpendicular and parallel configuration are depicted in Fig. 3.7. In comparison to Fig. 3.3 (c), one can see that the signal amplitudes as well as the relaxation times are in very good agreement to the results of the 50-layer sample. This verifies the quality of the home-grown sample, which is important for future projects.
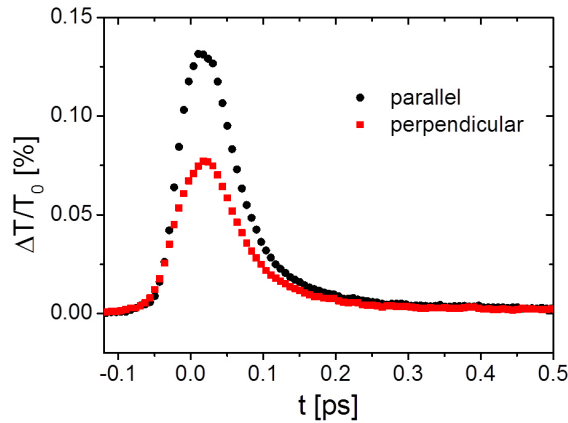
Figure 3.7.: Pump-probe signals for parallel and perpendicular configuration, measured with a home-grown sample on highly conductive SiC.

3.3. Two-color pump-probe experiments in the near-infrared range

The results discussed in this section where obtained within the framework of the diploma thesis of Fabian Göttfert [51], whose experimental work was supervised by myself. An optical-parametric oscillator (OPO) from the company APE served as radiation source for the two-color experiments. The OPO is pumped by a Ti:sapphire laser at a wavelength of $830\,\mathrm{nm}$, which delivers pulses of a duration of about $200\,\mathrm{fs}$

and a spectral width of 16 nm. In the OPO, a periodically poled potassium titanyl phosphate (KTP) crystal is placed within a cavity which also contains an additional dispersive element. By a nonlinear process in the crystal, the pump photons are split up into two so called signal and idler photons. Therefore, the photon energy of signal and idler photon are connected via the relation $\hbar\omega_{pump} = \hbar\omega_{signal} + \hbar\omega_{idler}$. While the cavity is not closed for the idler beam, which is coupled out directly after its generation in the crystal, for the signal beam the cavity is closed. The duration of one round trip through this cavity has to match exactly to the repetition rate of the pump laser. Due to the dispersive element within the cavity, this condition is only fulfilled for a small wavelength range. By changing the length of the cavity, the wavelength of both, signal and idler beam can be tuned.

In the first part of this section, the investigation of the electron temperature via two-color pump-probe measurements is presented. In the second part, the influence of the highly doped interface layers on the spectral dependence of the pump-probe signal is discussed. The sample with about 50 layers of graphene was used for the described experiments, which were performed at room temperature. The results of these measurements are published in [15] [2].

3.3.1. Probing the hot electron distribution

As discussed in the introduction, the fastest time constant of the relaxation is caused by extremely fast carrier-carrier scattering processes. For further insights how these processes lead to a hot carrier distribution, two-color pump-probe experiments were carried out for different values of the photon energies of pump and probe beam. In particular, the rather unusual configuration with a blue-shifted probe beam allowed us to estimate the temperature of the hot electron distribution. A schematic picture of the conditions for the experiments is depicted in Fig. 3.8 (a), the corresponding pump-probe signals are presented in Fig. 3.8 (b). For three different experiments, the photon energies were 0.68 eV, 0.54 eV, and 0.48 eV for the pump beam and 0.82 eV, 0.96 eV, and 1.02 eV for the probe beam, respectively. For all three signals, strong positive pump-probe signals could be observed, which is a direct evidence for the hot carrier distribution. Furthermore, the rise time for all three

---

[2]Figures 3.8 and 3.9 are reprinted with permission from S. Winnerl, F. Göttfert, M. Mittendorff, H. Schneider, M. Helm, T. Winzer, E. Malic, A. Knorr, M. Orlita, M. Potemski, M. Sprinkle, C. Berger, and W. A. de Heer, "Time-resolved spectroscopy on epitaxial graphene in the infrared spectral range: relaxation dynamics and saturation behavior", J. Phys.-Condens. Mat. **25**, 054202 (2013). Copyright 2013, IOP.

signals is identical, which indicates that the underlying process, leading to the hot carrier distribution, is too fast to be resolved by the temporal resolution of these measurements.
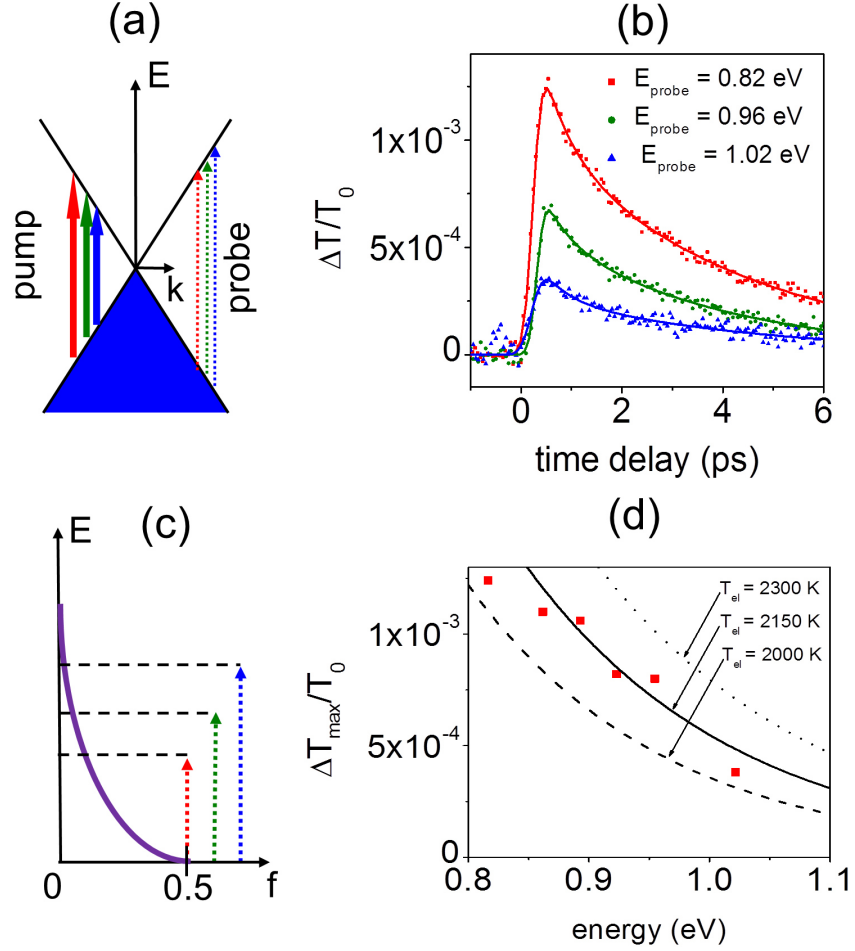
Figure 3.8.: Two-color pump-probe spectroscopy with a blue-shifted probe beam. (a) Schematic representation of the experiment. (b) Measured (dots) pump-probe curves, which are well described by biexponential decays (solid lines). (c) Sketch of a hot carrier distribution probed at the energies $(1/2)\,E_{probe}$. (d) Electron temperatures obtained for different probe energies. The experimental data fit to an electron temperature of $2150\,\text{K} \pm 150\,\text{K}$. Figure taken from [15].

From the amplitudes of the different pump-probe signals, the electron temperature of the hot electron distribution can be estimated. The amplitude of the pump-probe signal $\frac{\Delta T}{T_0}$ for a single graphene layer can be approximated by

$$\frac{\Delta T}{T_0} \approx -\Delta\alpha(\hbar\omega) = -\alpha_0(\Delta f_e(\hbar\omega/2) + \Delta f_h(\hbar\omega/2)). \qquad (3.3)$$

In this equation, α_0 stands for the universal absorption in graphene of 2.3%, the thermally induced change of the occupation for electrons and holes at a given energy is calculated by the Fermi function $f_{e,h}$. For the estimation of the electron temperature, the Fermi energy was assumed to be zero, the hot carrier distribution is sketched in Fig. 3.8 (c). The amplitude of the pump-probe signal as a function of the photon energy of the probe beam is depicted in Fig. 3.8 (d). The decrease of the signal amplitude with increasing photon energy can be best described by an electron temperature of $2150\,\text{K} \pm 150\,\text{K}$, which is represented by the lines in Fig. 3.8 (d).

3.3.2. Influence of the highly doped interface layers

Most of the signals observed in the near infrared range originate from the large number of quasi intrinsic layers of the sample. As the Fermi energy in these layers is very small compared to the photon energy, the carriers are excited by interband transitions and the positive pump-probe signal is caused by bleaching of this transition. In this section, a closer look on the influence of the highly doped interface layers on the pump-probe signals is taken. When the photon energy is slightly above or below twice the Fermi energy, the probed system changes strongly. Both schemes are shown in Fig. 3.9 (a) and (b). For photon energies slightly above twice the Fermi energy the transition is slightly bleached due to the increase of the electron temperature and the resulting pump-probe signal is positive. In the case of a photon energy slightly below twice the Fermi energy, the situation differs strongly. Interband absorption is partly suppressed in this case, so the absorption of this layer is very low. Still, a small part of the radiation can be absorbed, also by phonon assisted intraband absorption. In this case, the electron temperature is also increased and the Fermi edge is smeared out. When the Fermi edge is smeared out sufficiently, the interband transition is not blocked that strong anymore, and therefore the absorption of the sample increases. This increase of the absorption is strongest for photon energies slightly below twice the Fermi energy (cf. Fig. 1.3 (a)). The pump-induced absorption of a single, highly doped layer seems to be strong enough to lead to an overall negative signal. When the photon energy is decreased further the effect of the smeared out Fermi edge decreases strongly and the positive pump-probe signal

of the large number of less doped layers lead to a positive signal.

Two-color pump-probe measurements were performed at different probe photon energies of 0.4 eV to 0.82 eV to investigate the highly doped layers. A part of the results is shown in Fig. 3.9 for probe (pump) energies of 0.82 eV (0.68 eV) in (c), 0.66 eV (0.84 eV) in (d), 0.53 eV (0.97 eV) in (d) and 0.51 eV (0.99 eV) in (f). The sign of the pump-probe signal is only dependent on the probe-photon energy. The photon energy of the pump pulse should have no influence since a hot carrier distribution is obtained within the duration of the pump pulse. Corresponding to the explanation above, the probe-photon energy (c) is above twice the Fermi energy in the graphene layer with the highest doping. The sign of the pump-probe signal changes to negative as the probe energy is decreased to 0.66 eV (d), which indicates a photon energy below twice the Fermi energy. As the influence of this layer decreases, the negative signal part gets smaller (e.g. at 0.53 eV (e)) until the signals are purely positive again (e.g. at 0.51 eV (f)). From the first change in sign between probe-photon energies of 0.82 eV and 0.66 eV one can estimate the Fermi energy in the first graphene layer to be $0.37\,\text{eV} \pm 0.04\,\text{eV}$. For probe photon energies below 0.4 eV the sign of the signal changes again (not shown). This provides evidence that the second graphene layer has a Fermi energy of $0.208\,\text{eV} \pm 0.008\,\text{eV}$. These values match very well to the Fermi energies reported by Sun et al. [43], namely $E_f^1 = 0.36\,\text{eV}$ and $E_f^2 = 0.215\,\text{eV}$, measured on a similar sample. This indicates that the doping of the first interface layers seems to be very robust. Notably, the appearance of the negative signal is strongly dependent on the sample position, which might be caused by coupled layers of graphene on the interface or local variations of the Fermi energy.
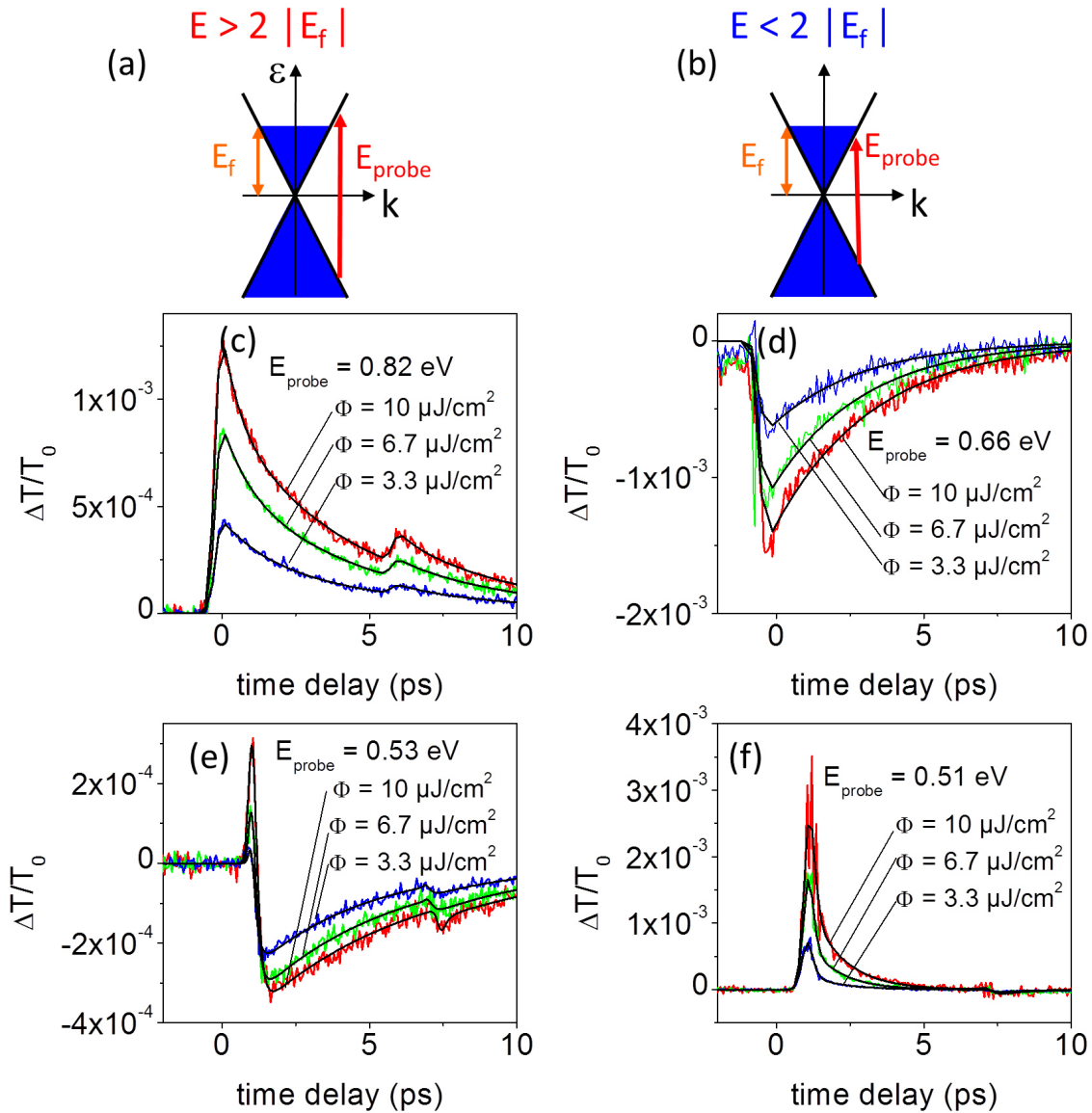
Figure 3.9.: Schematic illustration of probing the highly doped layer at the interface above (a) and below (b) the Fermi energy. (c)-(f) Two-color pump-probe signals for different probe energies and pump fluences as indicated. The colored curves are experimental data, the black lines fits based on a biexponential decay. The steps observed in part (c), (e) and (f) around delay times of 7 ps are artifacts caused by a secondary pump pulse caused by internal reflection in the substrate. Figure taken from [15].

3.4. Pump-probe experiments at small photon energy with large pump power

For pump-probe measurements with low pump power, the amplitude of the pump-probe signal is proportional to the applied pump power. When the pump power is increased to higher values, the pump-probe signal starts to saturate. In reference [74] the important mechanisms responsible for the saturation characteristics are described with microscopic theory and compared with results of pump-probe measurements in the near-infrared range. As more and more carriers are excited by a pump pulse, the absorption probability decreases and therefore the efficiency of the pumping is decreased for higher pump power. The saturation characteristics of graphene is mostly influenced by the Pauli blocking of the pumped transition as well as the relaxation dynamics, e.g. the extremely fast carrier-carrier scattering processes. Due to the strong absorption saturation, graphene can be used as saturable absorber in mode-locked lasers [75]. Due to the linear dispersion of the density of states in graphene in combination with the extremely fast carrier-carrier scattering, the saturation power scales quadratic with the photon energy [15].
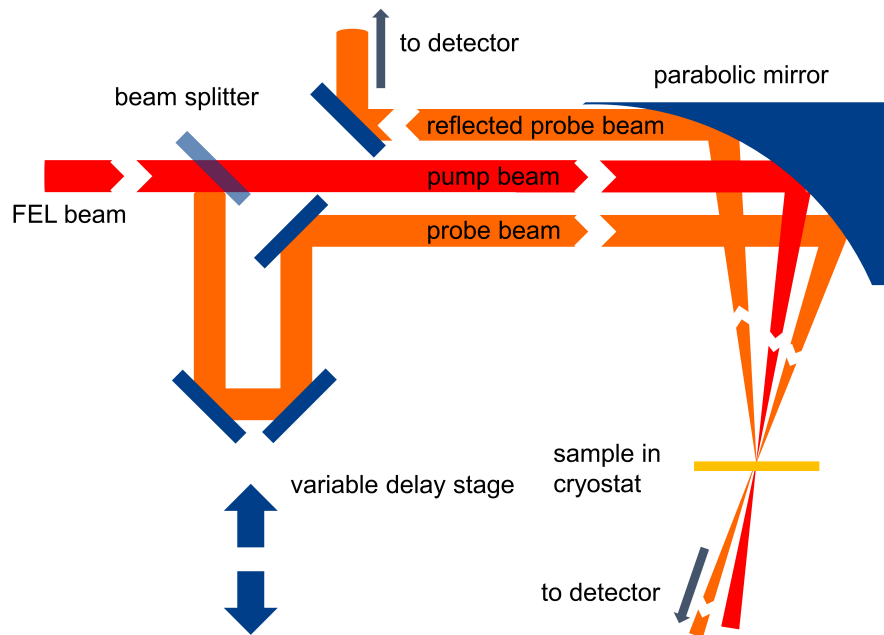

Figure 3.10.: Sketch of the setup for simultaneous measurement of pump-probe signals in transmission and reflection geometry.

Usually, the saturation of the pump-induced transmission through a graphene

sample is explained by a bleaching of the interband transition and therefore reduced absorption. The second possible mechanism, an increase of the reflectivity of the graphene, is usually neglected. To investigate the influence of pump-induced reflectivity to the change in the transmission, pump-probe measurements in transmission and reflection geometry were performed.

To have the opportunity of measuring pump-induced changes of transmission through the sample simultaneously with the reflection, the distance between pump and probe beam in front of the parabolic mirror was decreased. On the one hand the spatial separation of the probe beam from the pump beam is worse, which means that more scattered radiation from the pump beam will reach the detectors and therefore the signal-to-noise ratio is worse. On the other hand this allows one to use the focusing parabolic mirror also to separate the reflected pump beam from the incoming pump and probe beam without additional beam splitter. A simple sketch of the main features of the setup is shown in Fig. 3.10. Two different detectors were used for this measurement, namely a Si bolometer for the reflection measurement and a Ge:Ga detector in transmission geometry.

As the saturation power of the pump-probe signal increases with photon energy, the measurements were carried out at a wavelength of $42\,\mu$m, which corresponds to a photon energy of $30\,$meV. At this wavelength, the pump-probe signal, measured in transmission geometry, is still positive at low pump power. To get the purely positive signals, as well as a strong saturation and the negative signals at even higher pump powers, the pump power was varied between $1\,$mW and $320\,$mW. In Fig. 3.11, the results of the pump-probe measurements in transmission geometry are depicted.

A set of selected pump-probe signals in depicted in Fig. 3.11 (b). Here one can see the purely positive signal at low pump power, which is already nearly completely saturated at a pump power of $22\,$mW. At higher pump powers, the pump-probe signal is positive in the first part of the signal and gets a strong negative peak afterward. After the minimum is reached in the signal, the transmission through the sample again rises and a second change in sign occurs, resulting in a positive part at the end of the pump-probe signal. For the pump-probe signal at the lowest pump power, a secondary peak can be seen, which is caused by multiple reflection in the cryostat windows or the sample substrate. With increasing power, additional peaks arise, which were buried in the noise for the lower pump power. As the main peak gets saturated, the influence of these additional peaks increases.

The positive peak of the pump-probe signal as a function of the pump power
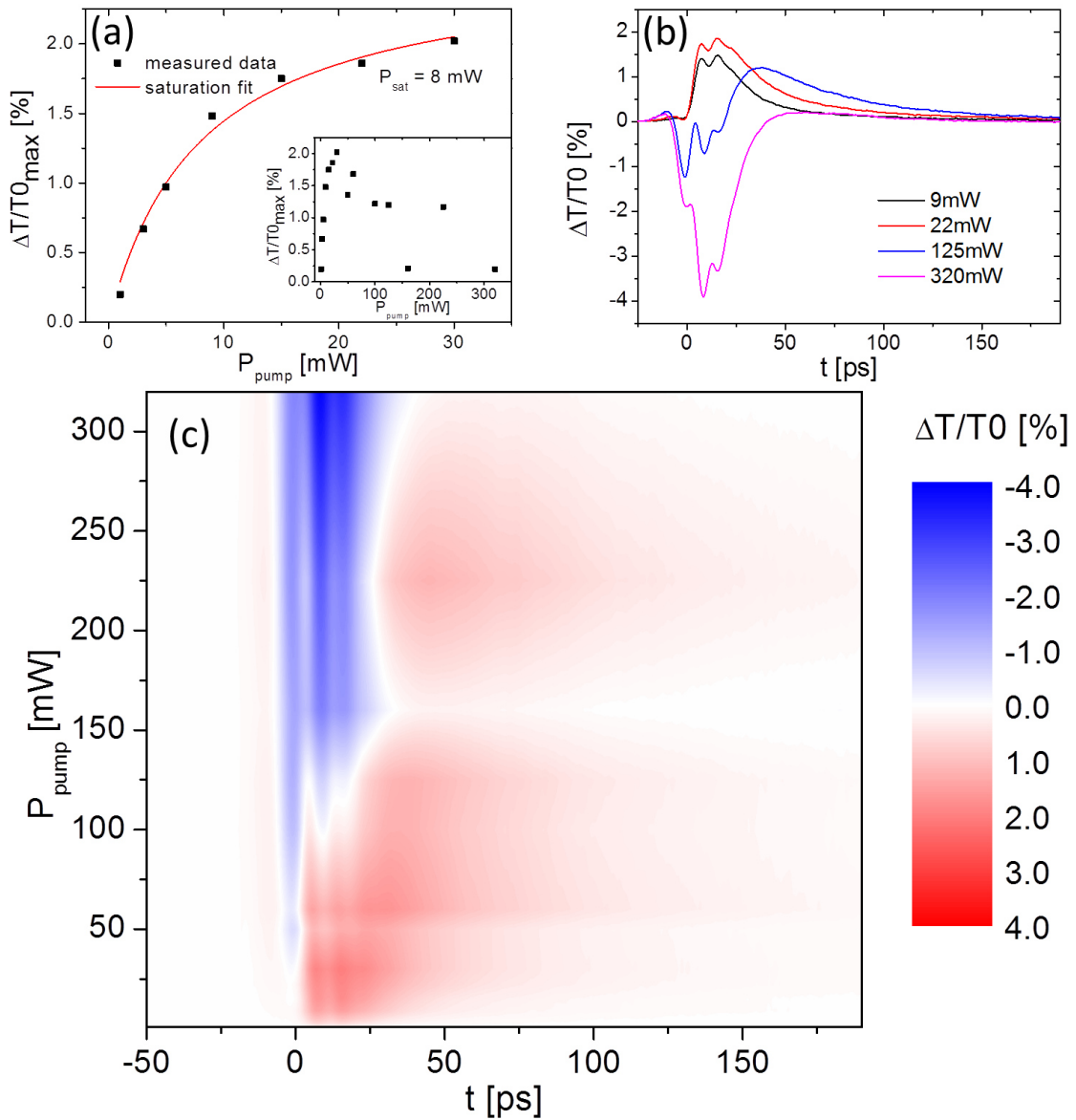
Figure 3.11.: (a) Positive amplitude of the pump-probe signal in transmission geometry as a function of the pump power up to 30 mW with saturation fit. In the inset the signal amplitude is shown for pump powers of up to 320 mW. (b) Pump-probe signal for different pump powers. (c) 2d-plot of the pump induced change in transmission as a function of the time delay between pump and probe beam (x-axis) and the pump power (y-axis), the pump induced change is color coded.

is shown in Fig. 3.11 (a) for the range of pump powers which result in purely positive signals, combined with the saturation fit. In the inset of Fig. 3.11 (a), the positive peak height of the pump-probe signal is shown for the whole measured range up to a pump power of 320 mW. In these two plots one can see the very low saturation power of 8 mW at this low photon energy, as well as the decrease of the positive signal amplitude for pump powers above 30 mW. The jumps of the signal amplitude at higher pump powers (e.g. at about 150 mW) are caused by changes in the probe power. To reach the high dynamic range in the power dependence, not only the pump power was varied, but also the probe power. Otherwise, the signal-to-noise ratio would have been very poor for the signals at the lowers pump power. Notably, the negative signal amplitude increases linearly with the pump power until the highest values are reached.

The whole data set, measured in transmission, is depicted in Fig. 3.11 (c). In this plot, the pump-induced change in transmission is color coded in dependence of the time delay between pump and probe pulse on the x-axis and the pump power on the y-axis. While a red color represents a positive signal, blue colors stand for decreased transmission through the sample. The visible vertical lines in the plot are caused by multiple pump and probe pulses, while the horizontal lines are caused by the aforementioned changes of the probe power. In this plot the positive change in transmission in the beginning and in the end of the signal can be seen.

The results of the measurements in reflection geometry are depicted in Fig. 3.12. The most obvious difference to the measurement in transmission geometry is the absence of negative signal parts. The saturation of the signal is shown in Fig. 3.12 (a), combined with a fit of the saturation function Eq. 3.2. The saturation power estimated for the measurements in reflection geometry is about 124 mW. This value can not be directly compared to the very low saturation power obtained in saturation geometry since the characteristics of these signals strongly differ. Corresponding to Fig. 3.11, in Fig. 3.12 (b) the pump-probe signals for different pump powers are depicted, while in Fig. 3.12 (c) the whole data set for all measurements in reflection geometry is shown. In contrast to the measurements in transmission geometry, no horizontal lines correspondings to the steps in applied probe power are visible in the color coded plot. This indicates that for the reflection mechanism the number of probe induced carriers play a minor role compared to the transmission signal.

To calculate the pump-induced change of the absorption, one needs to know the ratio between transmitted and reflected signal to consider the different responsivities
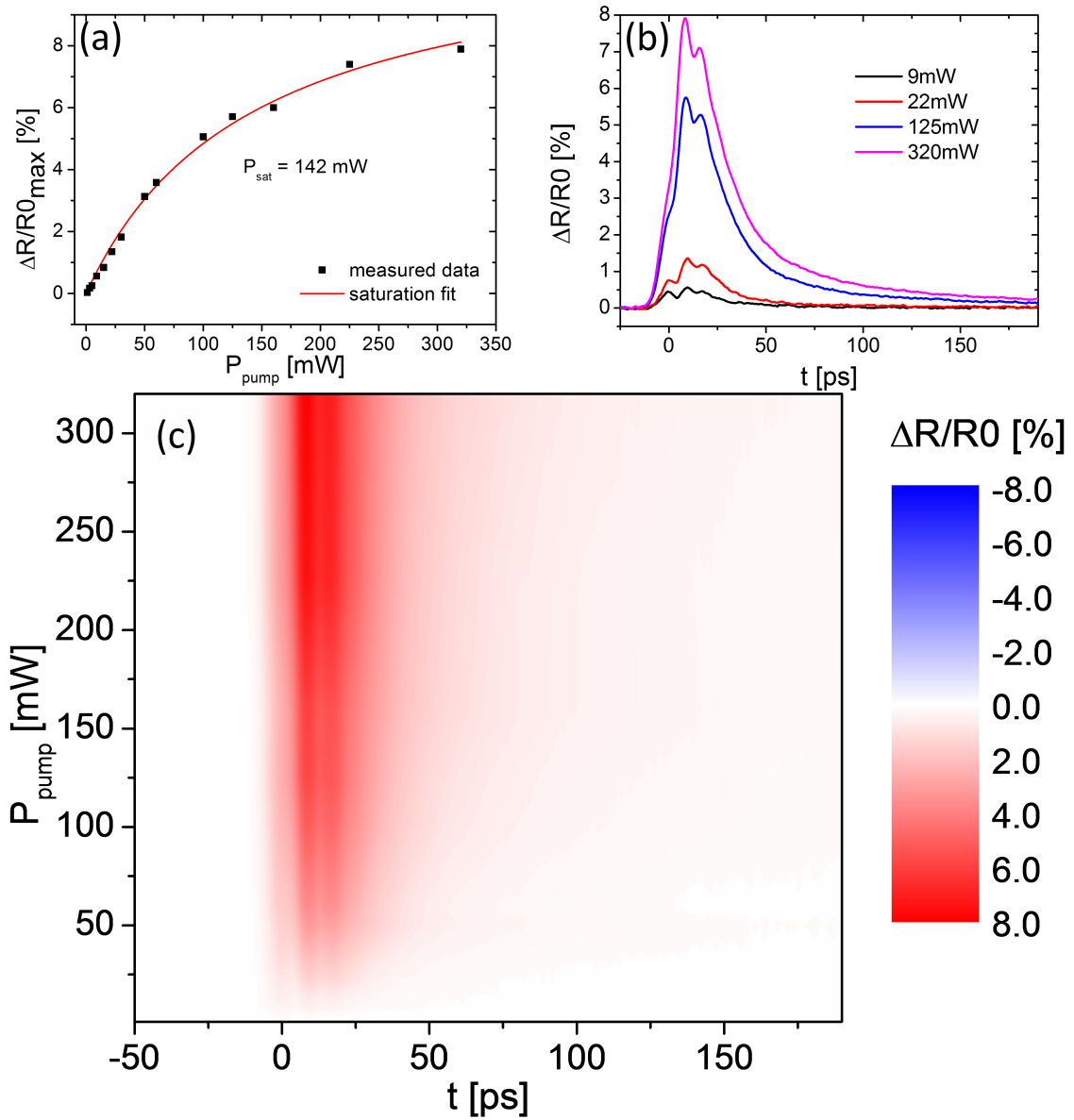
Figure 3.12.: (a) Amplitude of the pump-probe signal in reflection geometry as a function of the pump power with saturation fit. (b) Pump-probe signal for different pump powers. (c) 2d-plot of the pump induced change in reflection as a function of the time delay between pump and probe beam (x-axis) and the pump power (y-axis), the pump induced change is color coded.

of the detectors for the reflection and the transmission measurement. To get this ratio, the probe beam was chopped to have a relative measure for the transmitted and reflected probe beam. Later, the postion of the two detectors in transmission and reflection geometry was exchanged without further changes in the setup or the detector settings. This measurements revealed that the Ge:Ga detector had a 2.4 times higher responsivity compared to the Si bolometer. With this ratio, the measured change in reflection was scaled to the measured change in transmission and both signals were added. As long as the sum of these signals is positive, the pump-induced change of the absorption is also positive. The results of this calculation is depicted in Fig. 3.13. The pump-induced change of the absorption is purely negative for all pump powers, which means that the negative parts of the pump-probe signals in transmission geometry stem from the pump-induced increase of the reflectivity, but not a pump-induced absorption. Furthermore, also for the pump-induced change of the the absorption a clear saturation can be observed (cf. Fig. 3.13 (a)). The saturation power for the absorption is $56\,\mathrm{mW}$, which is between the values for the transmission and the reflection geometry. It is expected that Eq. 3.2 is valid for the saturation characteristics of the absorbance since it reflects the characteristics of a leaky two-level system. In contrast to this, the saturation of the signals in transmission geometry only follow this function phenomenologically for low photon energies. Therefore, taking into account only the pump-induced changes of the transmission leads to a saturation power which is strongly underestimated.

To compare the dynamics of the different measurements, a simple single-exponential fit was performed to the pump-probe signals. For the calculated signals of the absorption dynamics and the reflection measurement, the fit was performed for the full decay of the signal. Due to the change in sign in the transmission signal, this simple fit could not be performed. For all transmission signals, the fit was performed for the decay after the last positive peak. Hence, the dynamics of these measurements can not be compared directly. For the lowest pump powers, the signal-to-noise ratio for the reflection measurement was to poor to estimate a reliable relaxation time. The results of the fits is shown in Fig. 3.14. For the reflection and absorption signal, the relaxation time seems to be nearly independent of the pump power at around $20\,\mathrm{ps}$, for the transmission signal, the relaxation time strongly increases with the applied pump power. This strong increase of the relaxation time might be caused by the neglected fast initial decay, as only the signal after the second positive peak was considered, as well as by a slower signal component which
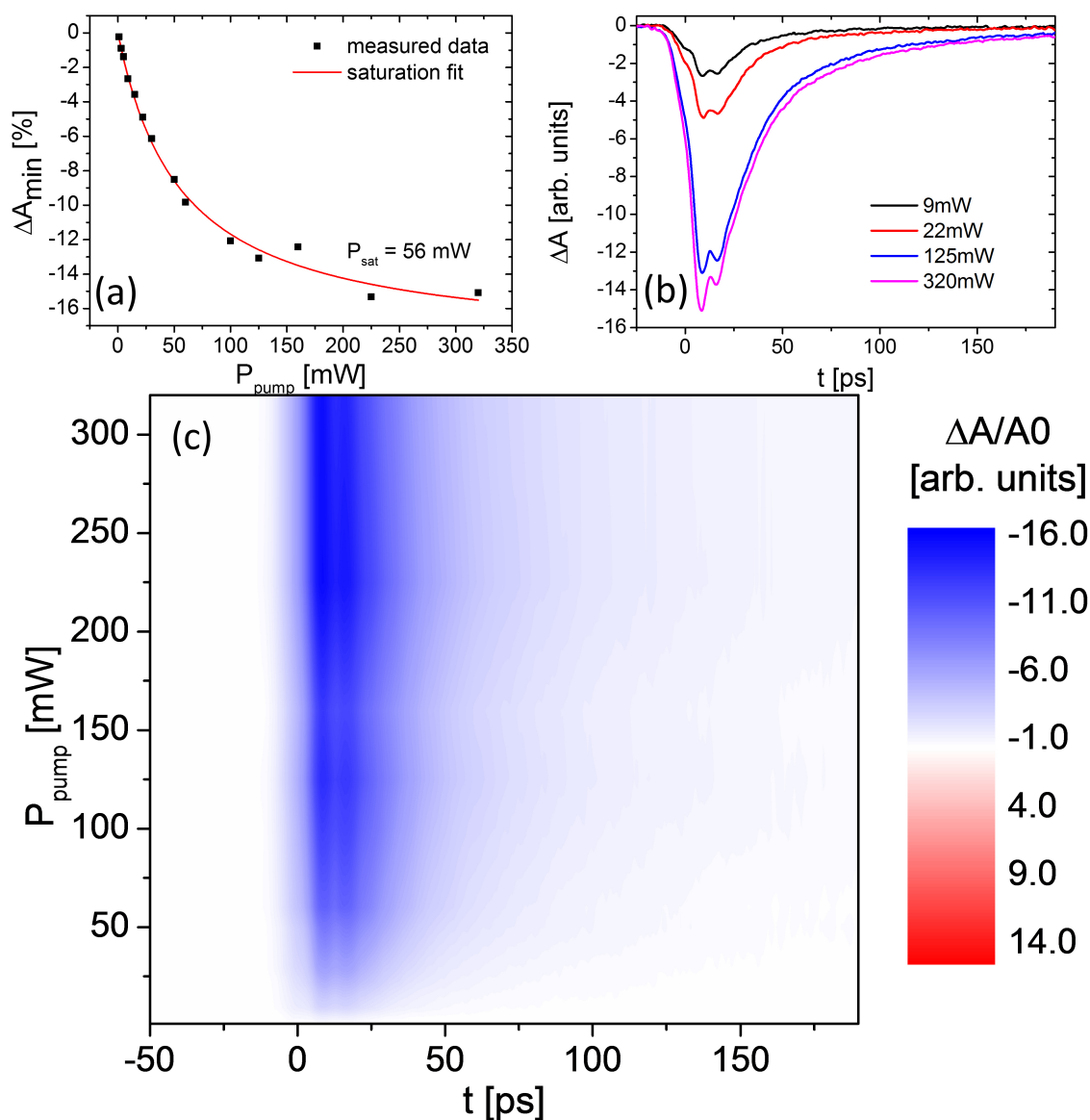
Figure 3.13.: (a) Calculated amplitude of the change in absorption as a function of the pump power. (b) Pump-probe signal for different pump powers. (c) 2d-plot of the pump induced change in absorption as a funcion of the time delay between pump and probe beam (x-axis) and the pump power (y-axis), the pump induced change is color coded.

is buried in the noise for low pump power. In general, the dynamics for the reflection measurement seems to be faster compared to the transmission measurement. The reason for the different dynamics of the pump-probe signals in transmission and reflection geometry is part of future work.
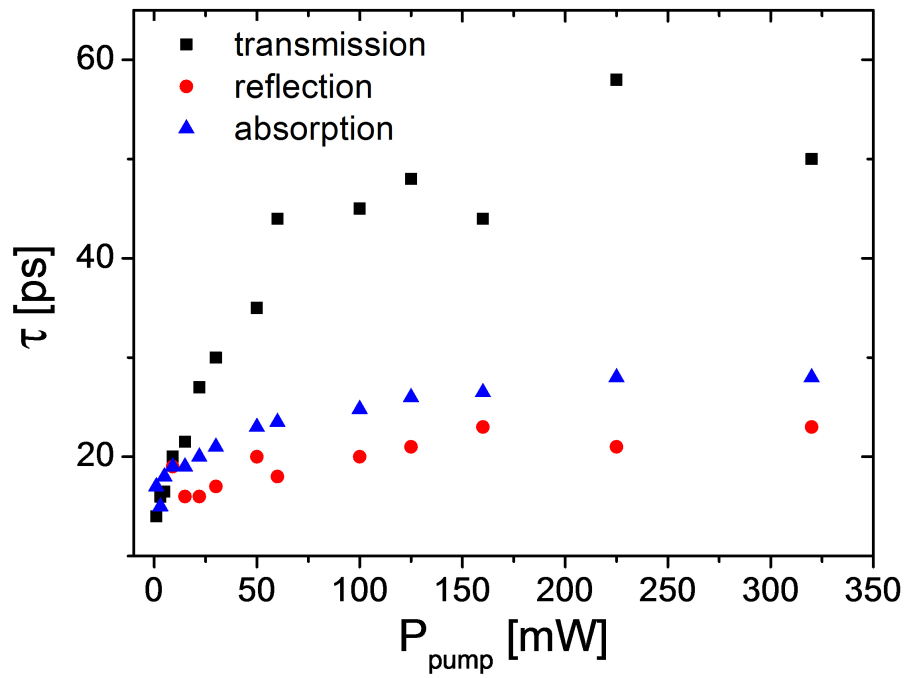
Figure 3.14.: Relaxation time for the different pump-probe signals as a function of the pump power.

4. Carrier relaxation dynamics in strong magnetic fields

While the carrier dynamics in graphene without magnetic field has been explored in a large variety of measurements (cf. Sec. 3.1), the dynamics of Landau quantized graphene is nearly unexplored. Only one study, where pump-probe measurements on graphene were performed in magnetic fields of up to 6 T, was published by Plochocka et al. [76]. A Ti:sapphire laser served as radiation source at a photon energy of 1.6 eV. At this high photon energy in combination with magnetic fields of up to 6 T, the pump induced change of the Landau level (LL) index is about 100. At these high energies, the LLs overlap strongly so that they form a quasi continuum. In this study it was shown that the relaxation time increases by a factor of 3 in high magnetic fields. The main focus of this thesis is therefore the investigation of the carrier relaxation in strong magnetic fields. In the first part of this chapter, a short introduction into the LL spectrum of graphene, as well as the optical properties of Landau-quantized graphene is given. In the second part, pump-probe measurements at small photon energies are presented. In these measurements, the dynamics of intraband LL transitions in the highly doped interface layers was measured. In the last part of this section, pump-probe measurements in the mid-infrared range are presented, which revealed the importance of Auger-like processes for the lowest LL transitions.

4.1. Landau-level spectrum of graphene

In conventional two-dimensional electron gases with parabolic band structure the LL spectrum is equidistant. The energy E of the LLs is proportional to the magnetic field and the index n of the LL:

$$E_n = \hbar\omega_c(n + 1/2). \tag{4.1}$$

The cyclotron frequency ω_c is determined by the magnetic field and the effective mass of the charge carrier via $\omega_c = eB/m^*$. As in graphene the electrons behave like massless particles with the constant Fermi velocity v_F, the LL spectrum differs strongly from this. To calculate the LL spectrum, one can start from the stationary massless Dirac equation for graphene

$$v_F(\sigma_x p_x + \sigma_y p_y)\Psi(r) = E\Psi(r), \tag{4.2}$$

where σ represents the Pauli spin matrices. The magnetic field is introduced to this equation by the transformation of the momentum operator

$$p \to p - qA(r), \tag{4.3}$$

where q represents the charge of the electron, A denotes the vector potential. The complete algebraic solution of this problem is described by Peres and Castro in [77]. The calculation results in a LL spectrum where the energy of each LL is proportional to the square root of the magnetic field B and the LL index:

$$E_n = sgn(n)v_F\sqrt{2e\hbar B|n|}. \tag{4.4}$$
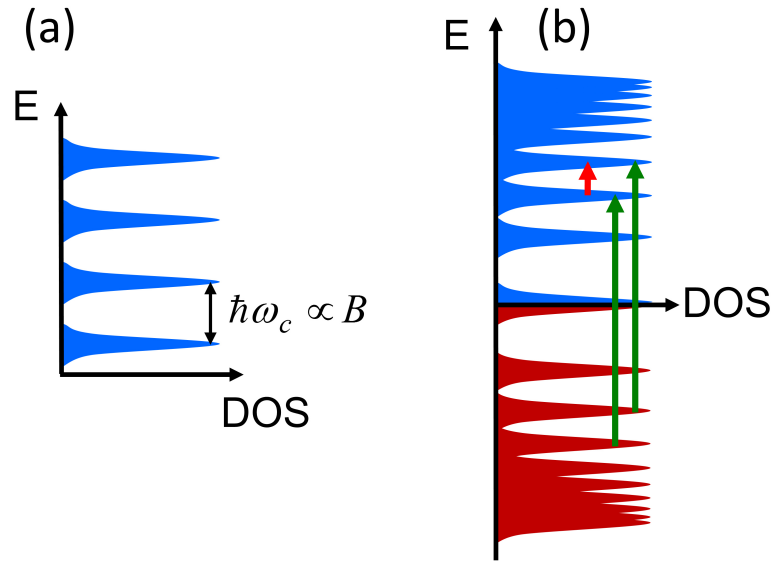
Figure 4.1.: Density of states of Landau quantized (a) two-dimensional electron gases with parabolic dispersion and (b) graphene. The arrows in (b) indicate the possibility of addressing distinct interband (green) or intraband (red) transitions by varying the photon energy.

The density of states for a conventional two-dimensional electron gas and graphene is depicted in Fig. 4.1. This non-equidistant LL spectrum of graphene enables one to perform pump-probe measurements on single LL transitions. In equidistant LL systems it is hardly possible to perform these measurements: As every transition has the same energy, an excited electron can still get excited to the next higher LL, therefore the transmission through a equidistant LL system remains nearly unchanged. With the free-electron laser as radiation source and the Oxford magnet cryostat that is able to produce magnetic fields of up to $8\,T$, a whole variety of different LL transitions can be addressed. For dipole radiation, only LL transitions where the absolute value of the LL index changes by $+/-1$ are accessible [7]. Therefore always two transitions are energetically degenerate, e.g. $LL_{-2} \Rightarrow LL_3$ and $LL_{-3} \Rightarrow LL_2$ (green arrows in Fig. 4.1 (b)), which can be distinguished by circularly polarized radiation. In the following, the combination of both transitions is denoted as $LL_{-2,-3} \Rightarrow LL_{3,2}$. In this example the electrons are excited from the valence band to the conduction band, so this type of transition is denoted as interband LL transition.

A second type of transition, where only one of the bands is involved, are the intraband LL transitions. The intraband LL transitions can only be excited in highly doped layers of graphene, e.g. at the interface to the SiC. One example for this type of transitions is indicated by the red arrow in Fig. 4.1 (b) ($LL_2 \Rightarrow LL_3$). However, for the example considered here where the transition $LL_2 \Rightarrow LL_3$ is active, i.e. in n-type graphene, the transition $LL_{-3} \Rightarrow LL_{-2}$ is inactive as both, initial and final state are fully occupied.

4.2. Intraband Landau-level transitions

In undoped graphene (at low temperature), only interband LL transitions are optically active as no higher-index LL is occupied. As soon as the Fermi energy deviates from zero, higher-index LLs are occupied, which can serve as ground state for optical excitation of carriers within one band. In multilayer-epitaxial graphene, a large number of the decoupled layers is quasi-intrinsic with a Fermi energy in the range of $10\,meV$, while the layers on the interface to the SiC are highly doped (see also Sec. 3.3.2). These highly doped layers open up the possibility to investigate intraband transitions via pump-probe experiments. The intraband LL transitions were investigated by pump-probe measurements at a wavelength of $88\,\mu m$ which corresponds

to a photon energy of $14\,\text{meV}$. By varying the magnetic field between $0\,\text{T}$ and $7\,\text{T}$, different interband and intraband LL transitions can be brought into resonance with the photon energy. In Fig. 4.2 the energies of different intraband LL transitions are depicted as a function of the magnetic field. The orange line at $14\,\text{meV}$ indicates the photon energy at our measurements. Most of the results described in this section are published in [78] [1].
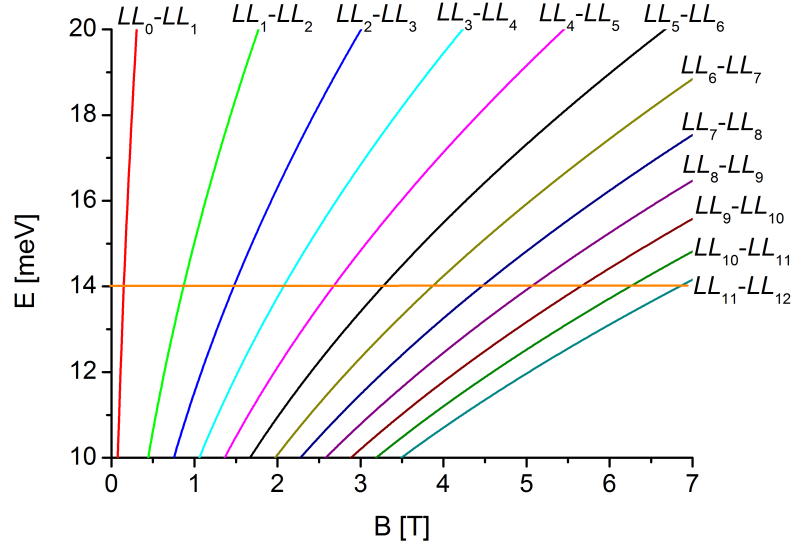
Figure 4.2.: Energy of different intraband LL transitions as a function of the magnetic field. The orange line at $14\,\text{meV}$ indicates the photon energy of the experiment.

4.2.1. Quasi cyclotron resonance

In Fig. 4.3, the energy of different LLs is plotted as a function of the magnetic field. An elevated Fermi energy, e.g. of about $80\,\text{meV}$, leads to optically active intraband LL transitions, as it is indicated by the black arrows. The highest occupied LL changes with the magnetic field as the Fermi energy shifts through different LLs. From this simple figure, one can already assume that the energy of the optically active intraband transition, indicated by the red dashed lines, scales linearly with the magnetic field.
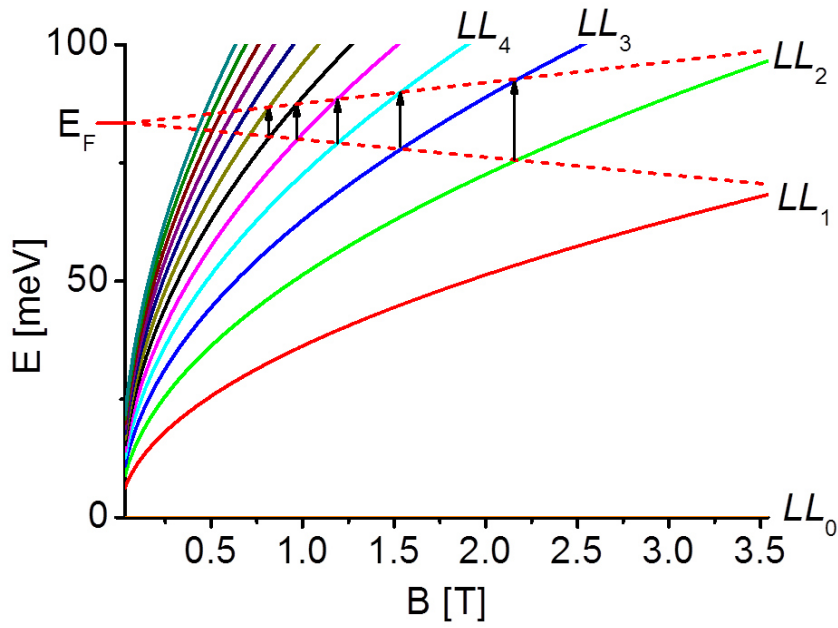
Figure 4.3.: Energy of different LLs as function of the magnetic field. In the highly doped graphene layers the optically active transition changes as the Fermi energy shifts through the LLs. Therefore the energy of the optically active transition is proportional to the magnetic field (indicated by the red dashed lines). Figure taken from [78].

This behavior can be described by a simple approximation. The photon energy E_{Phot} of the optical active intraband transition can be calculated by

$$E_{Phot} = E_{|nmax|+1} - E_{|nmax|}, \tag{4.5}$$

where $nmax$ is the highest populated LL and serves as ground state of the corresponding transition. The Fermi energy determines the index of the highest populated LL ($E_{|nmax|} = E_F$) and can be calculated using Eq. 4.4 by

$$n_{max} = \frac{E_F^2}{v_F^2 2e\hbar B}, \tag{4.6}$$

with the Fermi velocity v_F. With this LL index in combination with Eq. 4.4 one can calculate the energy of the next higher LL ($E_{|nmax|+1}$) via

$$E_{nmax+1} = v_F\sqrt{2e\hbar B \left(\frac{E_F^2}{v_F^2 2e\hbar B} + 1\right)} = \sqrt{E_F^2 + v_F^2 2e\hbar B}, \tag{4.7}$$

where the term $v_F^2 2e\hbar B$ is equivalent to the square of the energy of the first LL. With this relation the photon energy of the optical active intraband LL transition can be calculated using Eq. 4.5 via

$$E_{Phot} = \sqrt{E_F^2 + E_1^2} - E_F. \tag{4.8}$$

Considering that $E_1^2 << E_F^2$ one can use the first-order Taylor series approximation $\sqrt{1+x} \approx 1 + 0.5x$ to estimate the photon energy of the transition via

$$E_{Phot} = E_F\sqrt{1 + E_1^2/E_F^2} - E_F \approx E_F\left(1 + 0.5\frac{E_1^2}{E_F^2}\right) - E_F = \frac{v_F^2 e\hbar B}{E_F}. \tag{4.9}$$

In equation 4.9 one can see the linear connection between the energy of the optically active transition and the magnetic field. This behavior leads to a quasi cyclotron resonance, similar to the cyclotron resonance in conventional semiconductors with parabolic dispersion. The quasi cyclotron resonance of a single layer of graphene, grown on the Si-terminated face of SiC, was experimentally observed in static magneto spectroscopy by Orlita et al. [79]. They calculated the cyclotron mass m_c from the cyclotron resonance ω_c by $m_c = \omega_c / eB$. From this value, the Fermi energy in the graphene sheet was estimated by $|E_F| = m_c \cdot v_F^2$ to be $325\,\text{meV}$.

4.2.2. Amplitude dependence

To measure the magnetic-field dependence of the amplitude as well as the relaxation time of the pump-probe signal, the photon energy was $14\,\mathrm{meV}$ at a constant pump pulse energy of about $0.5\,\mathrm{nJ}$. With this pulse energy, an increase of the transmission of $0.3\,\%$ is induced without magnetic field. A set of pump-probe curves at different magnetic fields is shown in Fig. 4.4 (a). The amplitude as a function of the magnetic field is depicted in Fig. 4.4 (b). When a magnetic field of $0.165\,\mathrm{T}$ is applied, the transition $LL_{-1,0} \Rightarrow LL_{0,1}$ is resonant to the photon energy and the maximum change in transmission is increased by a factor of five. This transition cannot be clearly defined as interband or intraband transition since LL_0 is shared by valence and conduction band, in the following it is denoted as interband transition. When the magnetic field is increased above this value only intraband LL transitions can get into resonance with the photon energy (see Fig. 4.2). The signal amplitude decreases down to the value without magnetic field slightly above the resonance and further at intermediate magnetic fields.

Above $1.7\,\mathrm{T}$, the signal starts to go negative after a short initial positive peak. The negative part gets stronger as the magnetic field is increased, until at $3.1\,\mathrm{T}$ the negative peak reaches its maximum amplitude. At even higher fields the amplitude of the negative peak decreases again and above $3.3\,\mathrm{T}$, the signals are purely positive again. The signal amplitude increases strongly when the magnetic field is increased above $4\,\mathrm{T}$ and reaches $0.75\,\%$ at $7\,\mathrm{T}$, which is about three times larger compared to the signal without magnetic field. Note that the large number of quasi-intrinsic layers in this sample do not contribute to the signal at $7\,\mathrm{T}$ since in those layers no higher index LL is occupied. Hence, this extremely high signal, compared to the signal without magnetic field, is caused by only one or two highly doped layers at the interface to the SiC.

To understand the sign reversal of the pump-probe signal at intermediate magnetic fields, calculations of the absorption of a stack of differently doped graphene layers were performed using the Kubo formalism. Sadowski et al. showed in [7] how to calculate the optical conductivity σ_{xx} of a graphene layer in magnetic fields. With this, the contribution of each transition can be calculated by

$$\sigma_{xx}^{(n)}(B, T_{el}, \omega) = \frac{4(eB/h)e^2}{\omega} \frac{i(v_F^2/p)(f(E_{n-1}, E_F, T_{el}) - f(E_n, E_F, T_{el}))}{(E_n - E_{n-1}) - (\hbar\omega - i\gamma)}. \qquad (4.10)$$
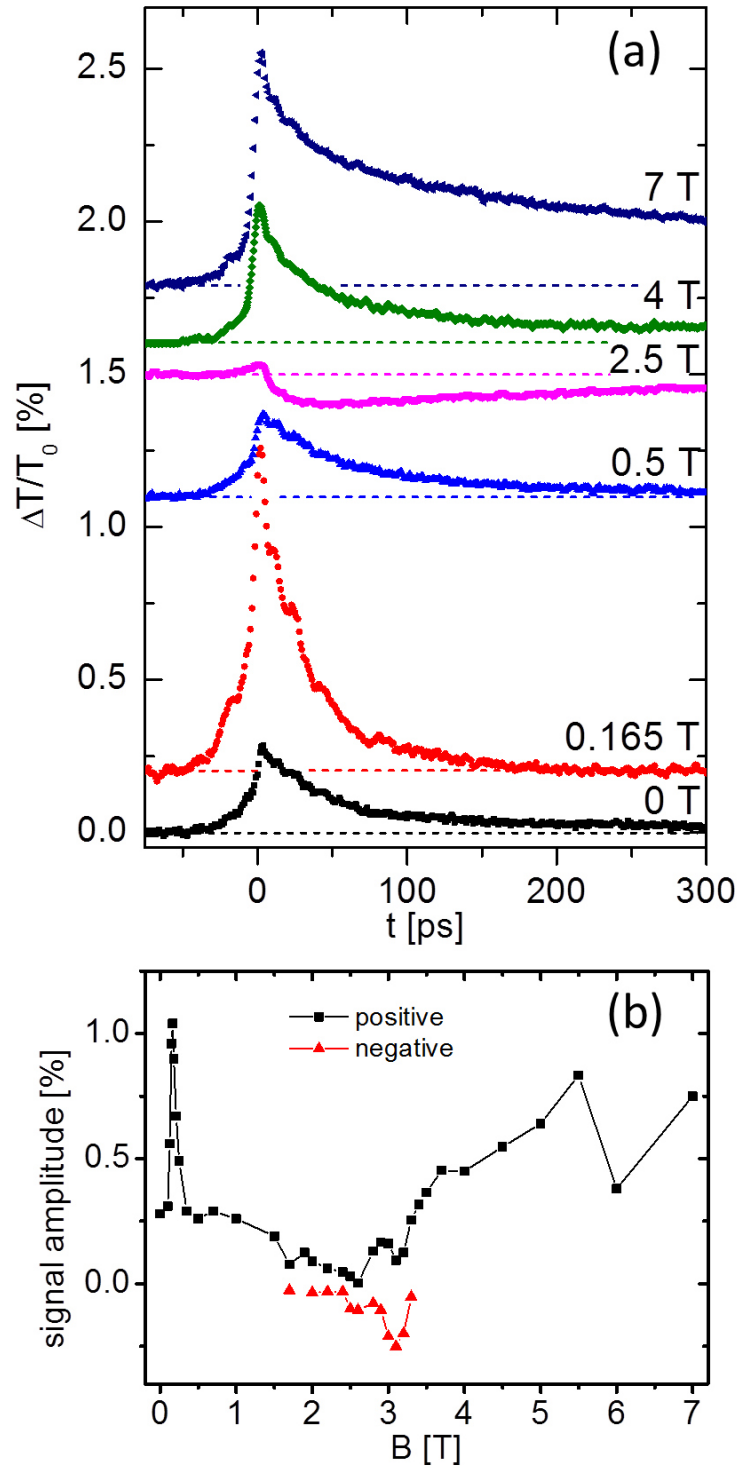
Figure 4.4.: (a) Pump-probe signals at different magnetic fields. For better visibility the curves are vertically shifted, the zero line for each curve is indicated by the dotted lines.(b) Amplitude of the pump-probe signal as a function of the magnetic field. Figure taken from [78].

T_{el} is the electron temperature and f the Fermi-Dirac distribution and $\gamma = 2\,\text{meV}$ is a phenomenological broadening parameter, p is the degeneracy of each LL. The conductivity contribution of the first 30 intraband LL transitions to the conductivity have been added up. The sample is assumed to consist of 30 layers of quasi intrinsic graphene with a Fermi energy of $5\,\text{meV}$ and four highly doped layers with Fermi energies of $E_{F1} = 380\,\text{meV}, E_{F2} = 230\,\text{meV}, E_{F3} = 150\,\text{meV}$ and $E_{F4} = 80\,\text{meV}$. The calculated absorption for a wavelength of $88\,\mu\text{m}$ as a function of the magnetic field is depicted in Fig. 4.5 (a).

In [43] Sun et al. measured the Fermi energy of the first four layers to be $E_{F1} = 360\,\text{meV}, E_{F2} = 215\,\text{meV}, E_{F3} = 140\,\text{meV}$ and $E_{F4} = 93\,\text{meV}$. As the sample measured for this thesis is very similar to the sample measured by Sun et al., these values were slightly varied to have a better overall agreement between our measurements and the calculation. The calculated absorption for a wavelength of $88\,\mu\text{m}$ as a function of the magnetic field is depicted in Fig. 4.5 (a). The broad maxima at magnetic fields of about $1.6\,\text{T}, 3.1\,\text{T}\ 4.7\,\text{T}$ and $8\,\text{T}$ correspond to the quasi-cyclotron resonances of the four highest doped layers. This calculations reproduces qualitatively the field dependent amplitude of the pump-probe signal (cf. Fig. 4.4 (b)). Note that the values in our calculations are in good agreement with the Fermi energies reported by Sun et al. in [43] ($E_{F1} = 360\,\text{meV}, E_{F2} = 215\,\text{meV}, E_{F3} = 140\,\text{meV}$ and $E_{F4} = 93\,\text{meV}$).

Comparing the absorption at different magnetic fields, one can see that at some fields the absorption decreases with increasing electron temperature, at other fields the absorption increases (cf. arrows in Fig. 4.5 (a)). The increased absorption at specific magnetic fields is caused by the smeared out Fermi edge, similarly to the origin of the negative signals discussed in Sec. 3.3.2. Assuming a thermalized carrier distribution, one can write down a simple balance equation for the time dependent electron temperature via [17]

$$\frac{dT_{el}}{dt} = \frac{P(t)}{c_p} - \frac{T_{el} - T_{latt}}{\tau}, \tag{4.11}$$

where $P(t)$ represents the absorbed pump power per unit area. T_{latt} is the lattice temperature and c_p the specific heat of the electrons in the graphene. τ is a phenomenological relaxation time. In combination with Eq. 4.10 one can estimate the pump-probe signal at different magnetic fields. In Fig. 4.5 (b) the calculated pump-probe signals at magnetic fields of $2.6\,\text{T}$ and $4.5\,\text{T}$ are depicted. Although this model does not include the non-equilibrium carrier distribution directly after
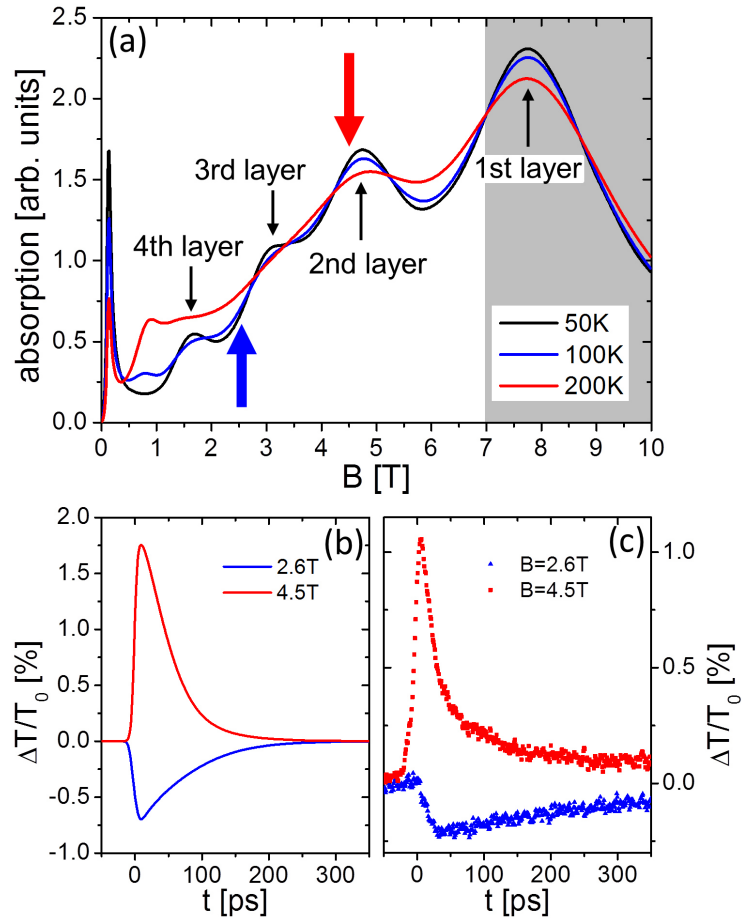
Figure 4.5.: (a) Calculated absorption at a wavelength of $88\,\mu$m as a function of the magnetic field for three different electron temperatures. The grey shaded area was not accessible in our experiment. (b) Calculated and (c) experimental pump-probe signals at two different magnetic fields with different signs, the blue and red arrow in (a) indicate the magnetic field of the measurement/calculation. Figure taken from [78].

the pump pulse, the calculated signals fit quite well to the measured ones depicted in Fig. 4.5 (c).

4.2.3. Relaxation time dependence

The relaxation dynamics at small photon energies at zero field is dominated by two different relaxation times as described in [17]. A fast one of about 25 ps, which is caused by the relaxation via the optical phonons, and a slow one of around 300 ps, which is determined by the relaxation via scattering processes with acoustic phonons. The relaxation times have been extracted from the measured data with a fit for a bi-exponential decay as described in Eq. 2.1. To minimize the number of fit parameters and therewith maximize the comparability between the different measurements, the error function was fixed. Only the two time constants and the scaling factors A and C can differ between the measurements. The pump-probe signal without magnetic field as well as the fit function are shown in Fig. 4.6. The extracted time constants are $\tau_1 = 40\,\mathrm{ps} \pm 1\,\mathrm{ps}$ and $\tau_2 = 550\,\mathrm{ps} \pm 50\,\mathrm{ps}$, the scaling factor $C = 6.8 \pm 0.4$ indicates that the faster time constant dominates the relaxation process. In comparison to [17] the time constants are longer, which can be explained as for those measurements another sample was used. Still the two time constants can be clearly attributed to the different relaxation channels via optical and acoustic phonons.

As described in section 4.2.2, at a magnetic field of 0.165 T the photon energy is resonant to the first LL transition $LL_{-1,0} \Rightarrow LL_{0,1}$. At this resonance, the relaxation time is strongly quenched to $\tau_1 = 2.6\,\mathrm{ps} \pm 1\,\mathrm{ps}$ and $\tau_2 = 36\,\mathrm{ps} \pm 0.5\,\mathrm{ps}$, while the scaling factor is about 1. This extremely fast relaxation time can be explained by Auger-like scattering processes, which are explained in detail in section 4.3.3. At higher fields the relaxation time is increased again, exceeding the relaxation time without magnetic field. In Fig. 4.7 (a) the fit parameters are depicted for different magnetic fields. While the sharp dip in the relaxation time at resonance with the LL transition $LL_{-1,0} \Rightarrow LL_{0,1}$ can be seen clearly, no systematic behavior is obvious for higher fields. In the range where the pump-probe signals are negative after a short positive peak (cf. Fig. 4.5 (b)), the interpretation of τ_1 and τ_2 differs from the one with purely positive signals. In this case the fast time constant represents the time of the sign reversal, which can also be seen as the scaling factor C is negative for those signals. At higher fields the time constants increase again, as does the scaling factor C. While the time constants themselves stay below the value at 0 T, the scaling factor is decreased compared to the measurements without magnetic
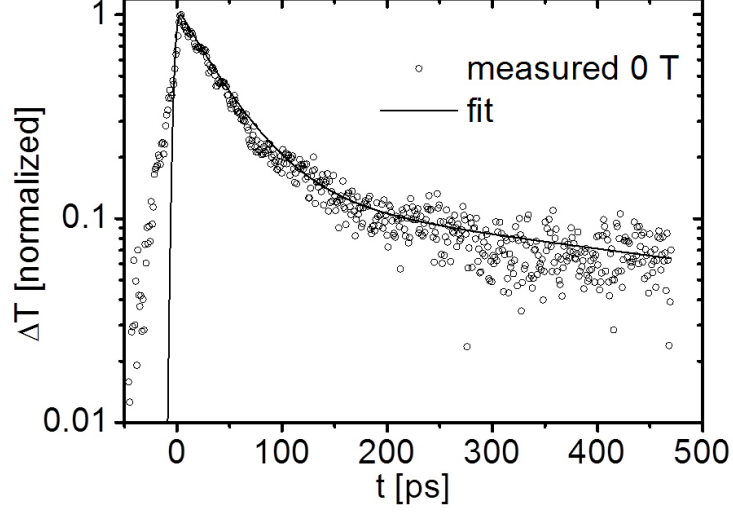
Figure 4.6.: Pump-probe signal at a photon energy of 14 meV and a pulse energy of 0.5 nJ without magnetic field. The open circles indicate the measured data, the line represents a fit function with a bi-exponential decay. Modified version of Fig. 4 in [78].

field. This indicates that the influence of the faster time scale τ_1 is weakened in the presence of a magnetic field and therefore the overall relaxation process is slowed down. To have an direct measure of the overall relaxation process, the time after which the signal has decreased to 20 % compared to its maximum amplitude ($\tau_{0.2}$) is depicted in Fig. 4.7 (b). Here one can see clearly that for all measurements in magnetic fields the relaxation process is slowed down, except at the resonance with the lowest LL transition $LL_{-1,0} \Rightarrow LL_{0,1}$.

4.2.4. Field dependent saturation

To get a deeper insight into the relaxation processes in Landau-quantized graphene, the dependence of the signal amplitude on the pump power was measured at three different magnetic fields (3.1 T, 6 T, and 7 T) and at 0 T. In Fig. 4.8 (a), the pump-probe signals for varied pump powers without magnetic field are depicted, in part (b) the amplitude is plotted as a function of the pump power. A clear saturation of the signal amplitude for pump powers above 10 mW can be observed. As described in Sec. 3.2, Eq. 3.2 was fitted to the measured data. The saturation measurements have been performed during two different FEL shifts. As the saturation strongly depends on the spot size of pump and probe beam on the sample, which is de-
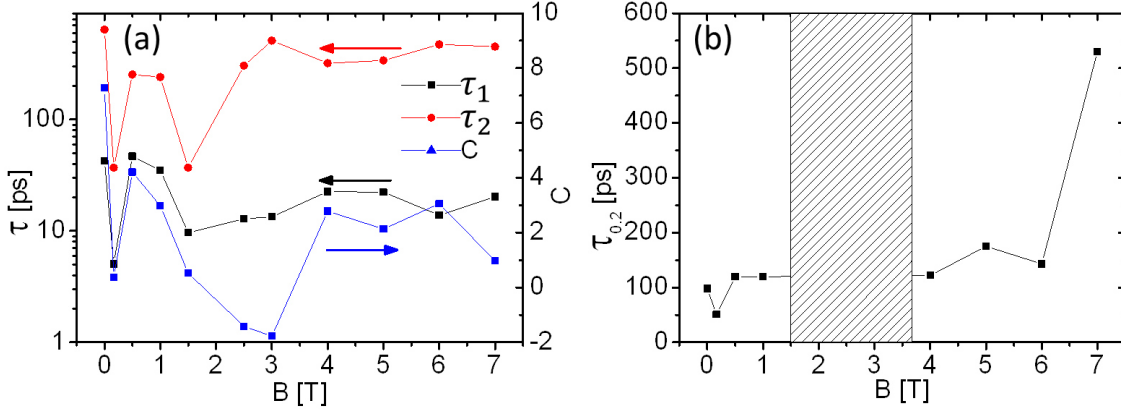
Figure 4.7.: (a) Fit parameters for different magnetic fields. (b) Time constant $\tau_{0.2}$ after which the signal is reduced to 20 % of the maximum signal amplitude. As this time constant does not make sense for the signals with sign reversal this area is shaded.

pendent on the beam profile of the FEL, the saturation characteristics can differ strongly between measurements on two different days. Furthermore, a difference in the alignment of the spatial overlap at the sample position can lead to the same effect. Comparing the data obtained on the two days at 7 T, the values for the saturation power P_{sat} changed from 16 mW in the first shift to 6 mW in the second shift. In contrast to the saturation power, the saturation amplitude A_{sat}, which indicates the maximum signal amplitude $(\Delta T_{max}/T_0)$ at full saturation, changed only slightly from 2.7 % to 2.9 % which is within the error of the fit. As the saturation amplitude remains nearly unchanged between these two measurements, the main difference seems to be indeed the spot size or the spatial overlap of pump and probe beam at the sample position. To have the saturation power comparable for all four measurements, the second measurement is normalized to the first one with the data sets measured at 7 T.

In Table 4.1 the saturation power as well as the saturation amplitude are shown. The values of the saturation power change in the range from $+15$ % to -40 %. Without magnetic field, the saturation power is strongly influenced by the extremely fast thermalization of the excited carriers [74]. Remarkably, the situation of the pump-probe measurements strongly change when the magnetic field is applied: Without magnetic field, the pump-probe signal is dominated by interband excitation in the large number of quasi-intrinsic layers. In contrast, when the magnetic field is applied, intraband transitions within one or two highly doped layers are mainly excited.

Therefore, the constant saturation power might indicate that the non-equilibrium carrier distribution after the pump pulse gets thermalized similarly fast under Landau quantization. At least for the higher-index intraband transitions this behavior would not be surprising: Although the transition energies between neighboring LLs are not equidistant, a scattering process of two electrons in the LL_n to the levels LL_{n-1} and LL_{n+1} is possible due to the broadening of the LLs.
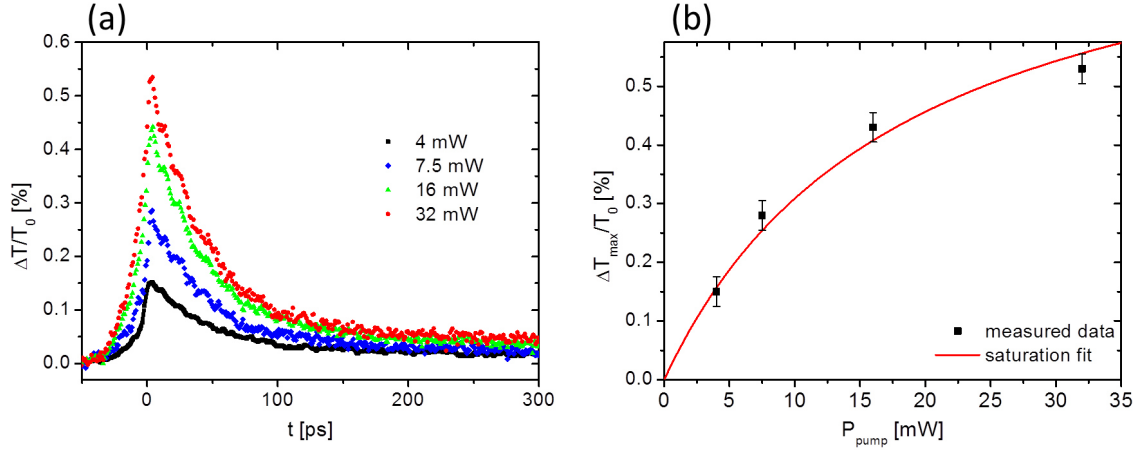
Figure 4.8.: a) Pump-probe signals for different pump powers without magnetic field. b) Signal amplitude in dependence of the pump power, the black dots represent the measured data, the red line indicates a saturation fit (cf. Eq. 3.2).

Table 4.1.: Parameters of the fitfunction Eq. 3.2 for measurements at different magnetic fields. ^{a} indicates values measure on 01.02.2013, values marked by ^{b} are measured on 31.01.2013.

	0 T	3.1 T (pos.)	3.1 T (neg.)	6 T	7 T
P_{sat}[mW]	18.3^a	4.4^b	3.6^b	17.7^a	$16.1^a/5.9^b$
$P_{sat}/P_{sat}(7\,\mathrm{T})$	1.13	0.74	0.61	1.10	1
A_{sat}	0.9 %	0.3 %	-0.8 %	1.1 %	2.8 %

4.2.5. Temperature dependence at high magnetic fields

The temperature dependence of the carrier relaxation has been measured at 7 T. Due to a lack of FEL beam time, it was not possible to measure this dependence at different magnetic fields or at 0 T. In Fig. 4.9 (a), the pump-probe signals measured

at different sample temperatures are depicted, the signal amplitude as a function of the sample temperature is shown in Fig. 4.9 (b). The amplitude of the pump-probe signal decreases approximately linearly in the temperature range from 8 K to 50 K. This decrease of the signal amplitude might be caused by the strongly decreased relaxation time at higher temperatures. Taking a closer look to Fig. 4.9 (a), one can realize already with the bare eye that both relaxation times become significantly shorter with increasing temperature.
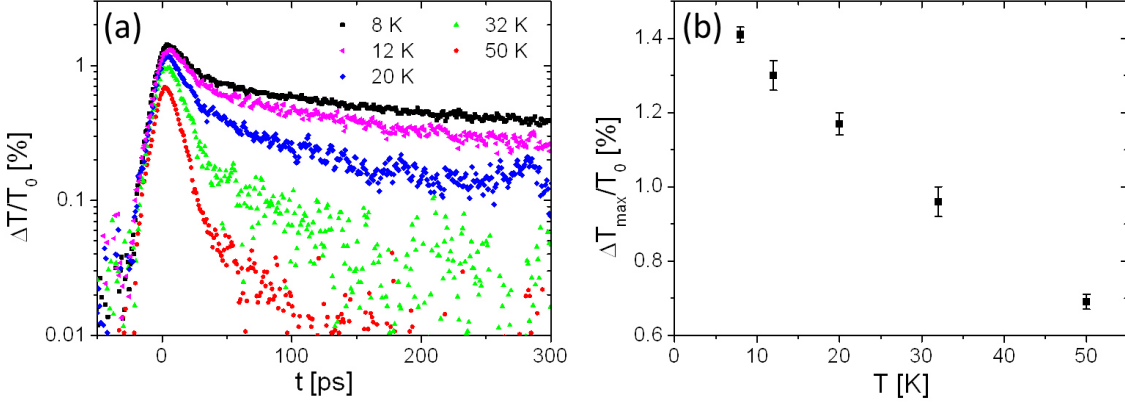
Figure 4.9.: (a) Pump-probe signals for different sample temperatures at 7,T. (b) Signal amplitude in dependence of the sample temperature.

By fitting Eq. 2.1 to the measured data, the different time constants are extracted (see Fig. 4.10). In previous measurements without magnetic field it has been shown that for larger photon energies the relaxation times are only slightly dependent on the sample temperature, while for small photon energy the relaxation processes are strongly sped up [15]. At the highest magnetic field of 7 T and a temperature of 8 K, τ_1 is about 18 ps and τ_2 is about 530 ps. Both time constants decrease to 5 ps and 45 ps, respectively, upon rising the temperature to 50 K.

This strong decrease of the relaxation time for higher temeperatures can be explained by an increased thermal phonon occupation. A second contribution could be the disorder-assisted electron-phonon scattering. Song et al. [80] reported the important role of so-called supercollisions (without magnetic field), which was proven by other groups [81–83]. The main idea is that a phonon can lose a large part of its momentum via scattering on defects in the graphene lattice, which strongly increases the number of phonons available for electron-phonon scattering. This effect is strongly temperature dependent and leads to a strong decrease of relaxation times at higher temperatures.
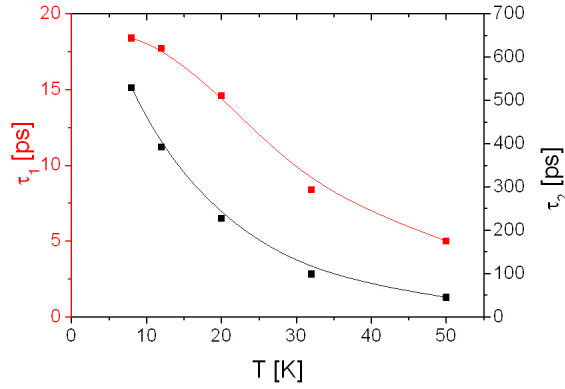
Figure 4.10.: Temperature dependence of the two time constants extracted from the pump-probe signals. The continuous lines serve only as guide to the eye.

4.2.6. Measurements of a single layer of quasi-free-standing graphene

In addition to the measurements on the multilayer samples, measurements with a single layer of quasi-free-standing graphene have been performed. This sample was grown by the group of Thomas Seyller on the Si-terminated face of SiC [39,84]. The quasi-cyclotron resonance for this sample was already measured by static magneto-spectroscopy [79].
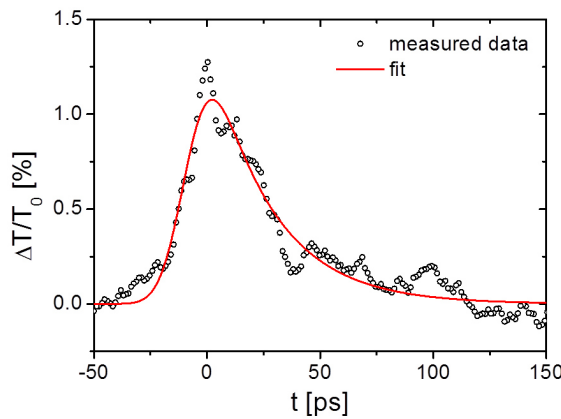
Figure 4.11.: Pump-probe signal of a quasi-free-standing layer of graphene at 7 T. The circles represent the measured data while the red line is a fit with a single exponential decay to the measured data.

The measurements were performed under the same conditions as described for the multilayer samples. Without magnetic field, no pump-probe signal could be

measured with the single-layer sample. This might be explained by the Fermi energy, which is about -0.3 eV in this type of sample [85]. Hence, interband transitions are completely blocked at the low photon energy in this experiment. Pumping of the system via intraband absorption is still possible, but the signal is expected to be very small and might be buried in the noise. The reason for this is the fact that the Fermi edge can be smeared out only slightly compared to the high Fermi energy as the photon energy is very small. At a magnetic field of 7 T, a pump induced increase of the transmission of about 1.4 % could be observed. The FEL did not work very stable on the day of this measurement, so the signal-to-noise ratio of the pump-probe signals is very poor. To minimize the noise, the average of four pump-probe measurements was calculated. The averaged signal is depicted by open circles in Fig. 4.11, the red line is a fit with a single-exponential decay of 27 ps. A fit with a double exponential function does not make any sense, as the second time constant is mainly buried in the noise.

4.3. Interband Landau-level transitions

In contrast to Sec. 4.2, this section is dedicated to interband LL transitions including the transition $LL_{-1,0} \Rightarrow LL_{0,1}$. This transition can not easily be assigned as an interband or intraband transition as the zeroth LL belongs partly to the valence band as well as to the conduction band. In the following, this transition will be described as the lowest interband LL transition. It was also measured at small photon energy in Sec. 4.2, but not discussed in detail. To investigate the dynamics of interband LL transitions, pump-probe measurements have been performed at a wavelength of 16.5 μm at magnetic fields of up to 7 T. At this wavelength the energy of the lowest LL transition is resonant to the photon energy of 75 meV at a magnetic field of 4.2 T. With linearly polarized radiation the two transitions $LL_{-1} \Rightarrow LL_0$ and $LL_0 \Rightarrow LL_1$ are pumped and probed at the same time. The results of measurements with linearly polarized radiation, which are described in the first part of this section, were rather surprising as a decrease of the relaxation time was observed in magnetic fields. Therefore measurements with circularly polarized radiation have been performed, which enables one to distinguish between the aforementioned transitions. In the second part of this section the results of measurements with circularly polarized radiation are presented, which revealed complex signals with positive and negative signal parts, caused by Auger-like processes. These processes can be describe by a

simple rate equation model for a three-level system, which is discussed afterwards. The experimental results and the findings of the rate equation model are confirmed by microscopic calculations based on the density matrix formalism. In the last part of this section, a second set of measurements is presented, which was performed with a different sample. Parts of the work presented in this section are published in [86].

4.3.1. Measurements with linearly polarized radiation

At a wavelength of $16.5\,\mu\mathrm{m}$, which corresponds to a photon energy of $75\,\mathrm{meV}$, the duration of the FEL pulses is about $2.7\,\mathrm{ps}$. A pump pulse with an energy of $10\,\mathrm{nJ}$ induced a transmission increase of $1.8\,\%$ at zero field. The decay of the signal can be described by an exponential decay with a time constant of $18\,\mathrm{ps}$.
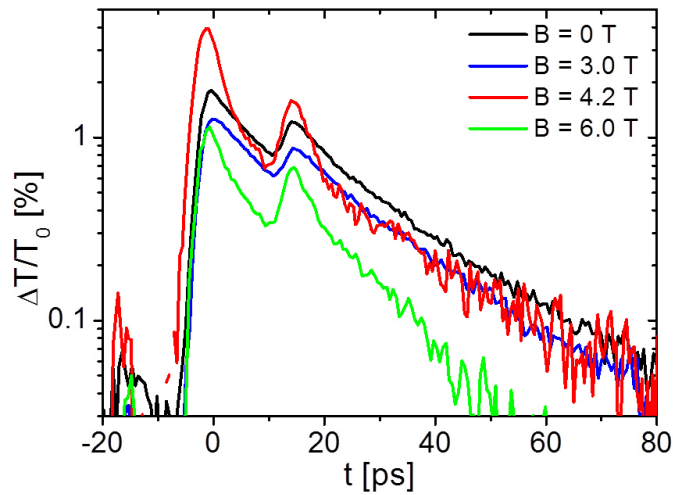
Figure 4.12.: Pump-probe signals for different magnetic fields measured with linearly polarized radiation at a wavelength of $16.5\,\mu\mathrm{m}$.

The signals in the following parts are divided by the transmission through the sample without magnetic field, since a reference measurement was done only without magnetic field. Applying a magnetic field has a strong influence on the amplitude of the pump-probe signal and the relaxation time. A set of pump-probe signals, measured at different magnetic fields, is presented in Fig. 4.12. Such measurements were performed at various magnetic fields between $0\,\mathrm{T}$ and $7\,\mathrm{T}$ and analyzed with respect to the signal amplitude (see Fig. 4.13) and the decay time (see Fig. 4.14). At lower fields only a slight decrease of the signal amplitude appears, while the time constant stays unchanged. In this low-magnetic field part without significant struc-

ture, higher index interband LL transitions (e.g. $LL_{-5,-6} \Rightarrow LL_{6,5}$) are resonant to the photon energy. For these high-index transitions, the absorption strength is quite small since it scales with the magnetic field, so they are also hardly visible even in static magneto-spectroscopy. The first clear resonance is reached at a magnetic field of 0.45 T, where the photon energy is resonant to the transition $LL_{-2,-3} \Rightarrow LL_{3,2}$. The amplitude increases slightly while no change in the relaxation time can be observed. At the next lower transition $LL_{-1,-2} \Rightarrow LL_{2,1}$, which is resonant at a magnetic field of 0.75 T, a more pronounced increase of the signal amplitude is visible, the relaxation time still remains constant. For a better visualization of these two higher transitions, a detail of Fig. 4.13 (a) is depicted in Fig. 4.13 (b). For increased magnetic fields between 1.2 T and 3 T the signal amplitude decreases until a minimum of 1.1 % is reached. The relaxation time slowly increases until it reaches its maximum of about 25 ps. Notably in this magnetic field range no LL transitions of graphene can be resonant to the photon energy, therefore it is rather surprising to observe signals which exhibit nearly the same strength compared to the measurements without magnetic field. This fact might be caused by defects in the graphene layers giving rise to a background density of states or some parasitic flakes of coupled multilayers.
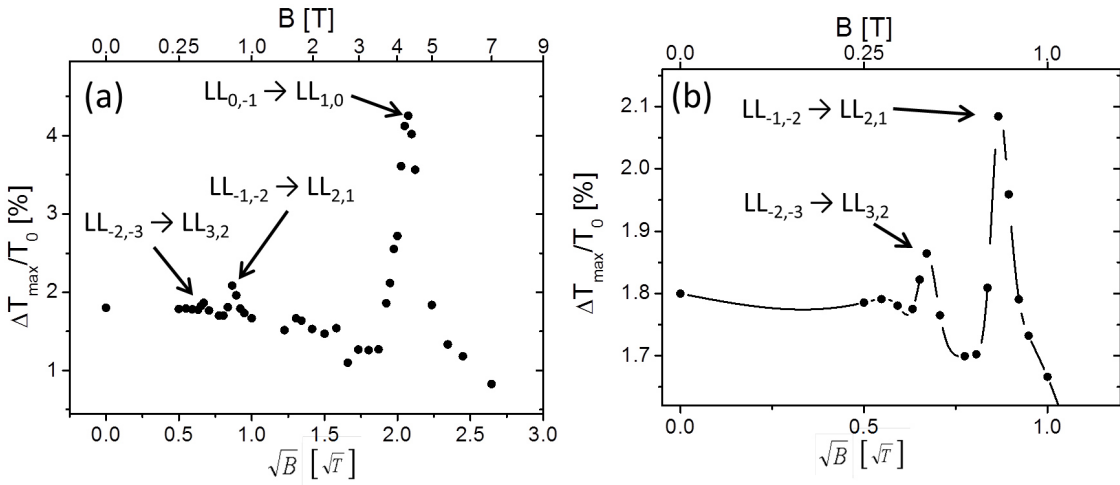
Figure 4.13.: (a) Amplitude of the pump-probe signals as a function of the square root of the magnetic field. The amplitudes are normalized to the amplitude without magnetic field. (b) Enlarged detail of (a), where the higher index interband transitions are visible.

Above 3 T the signal amplitude strongly increases until it reaches its maximum at 4.2 T, where the photon energy is resonant to the LL transition $LL_{0,-1} \Rightarrow LL_{1,0}$.

The amplitude increases to 4.2 %, which is about 2.5 times the amplitude of the measurements without magnetic field. A strong increase of the relaxation time was expected, as this was observed for high-index LL transitions. Plochocka et al. reported an increase of the relaxation time of a factor about 3 with magnetic fields of up to 6 T [76]. They assumed this to be caused by a strong reduction of electron-electron scattering processes and supposed that these processes should be even stronger suppressed for low-index LL transitions. In contrast to this, we observed a shortening of the relaxation time by a factor of 10 in our measurements. Above this resonance the signal amplitude strongly drops down while the relaxation time increases again until the maximum field of 7 T is reached.
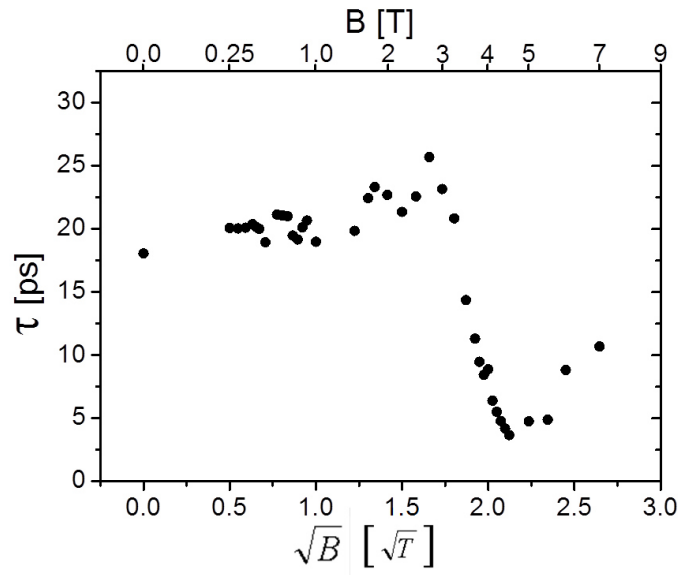
Figure 4.14.: Relaxation time of the pump-probe signals as a function of the square root of the magnetic field. The values are extracted by a fit function with a single-exponential decay.

4.3.2. Measurements with circularly polarized radiation

To get a deeper insight in the processes at the lowest LL transition ($LL_{0,-1} \Rightarrow LL_{1,0}$), pump-probe measurements with circularly polarized radiation have been performed. As the radiation of the FEL is linearly polarized, two $\lambda/4$ plates were included in pump and probe beam. With this all four combinations of polarization of pump and probe beam could be measured, namely $\sigma_{pump}^+/\sigma_{probe}^+$, $\sigma_{pump}^+/\sigma_{probe}^-$, $\sigma_{pump}^-/\sigma_{probe}^+$ and $\sigma_{pump}^-/\sigma_{probe}^-$. While the transition $LL_{-1} \Rightarrow LL_0$ is allowed for

σ^+ polarized radiation, the transition $LL_0 \Rightarrow LL_1$ can be excited by σ^- polarized radiation. Intuitively one would expect positive pump-probe signals (increased transmission) when pump and probe radiation have the same polarization state. The pump pulse depopulates the ground state of the probed transition, while the excited state gets populated. Therefore Pauli blocking for this transition should lead to positive pump-probe signals. For the case of opposite polarization states, e.g. when the lower transition is pumped and the upper transition is probed, the pump pulse populates the ground state while the excited state of the probed transition remains unchanged. As the ground state of the probed transition is populated, the probability for absorption of a photon is increased and negative pump-probe signals (increased absorption) are expected. The results of the measurement of the four different pump-probe measurements are depicted in Fig. 4.15. The multiple peaks are caused by iterated pumping of the sample due to multiple reflections on the beam line window and/or the cryostat window. Although these peaks disturb the signal, the initial dynamics as well as the long time relaxation can be analyzed.

Some of the measurement results differ strongly from this first expectations. A set of complex signals is revealed, which partly even change the sign. In Fig. 4.15 (a) and (b), the signals of the measurements with same polarization are depicted. For the case of σ^- polarized radiation the signal is purely positive as it was expected (b), but with of σ^+ polarized radiation the signal is negative after a very short positive peak (a). For the measurements with opposite polarizations (Fig. 4.15 (c) and (d)) the situation is similar. For the case of σ^- polarized pump radiation and σ^+ polarized probe radiation, the signal is purely negative like expected (c). In the opposite case the pump-probe signal is purely positive, which is opposed to the expectation (d). Adding up these four pump-probe signals should lead to the same signal as the pump-probe measurement with linearly polarized radiation, as the linearly polarized radiation can be described by a superposition of σ^+ and σ^- polarized radiation. The sum of the four signals obtained by all four combinations of pump and probe polarization is depcited in Fig. 4.16 together with the pump-probe signal measured with linearly polarized radiation. Only a small deviation between the sum of the four circularly polarized measurements and the linearly polarized measurement, which might be caused by slightly elliptical instead of circularly polarized radiation, can be observed.

This addition of the four different signals directly can explain phenomenologically the surprising effect of the short relaxation times measured with the linearly polar-
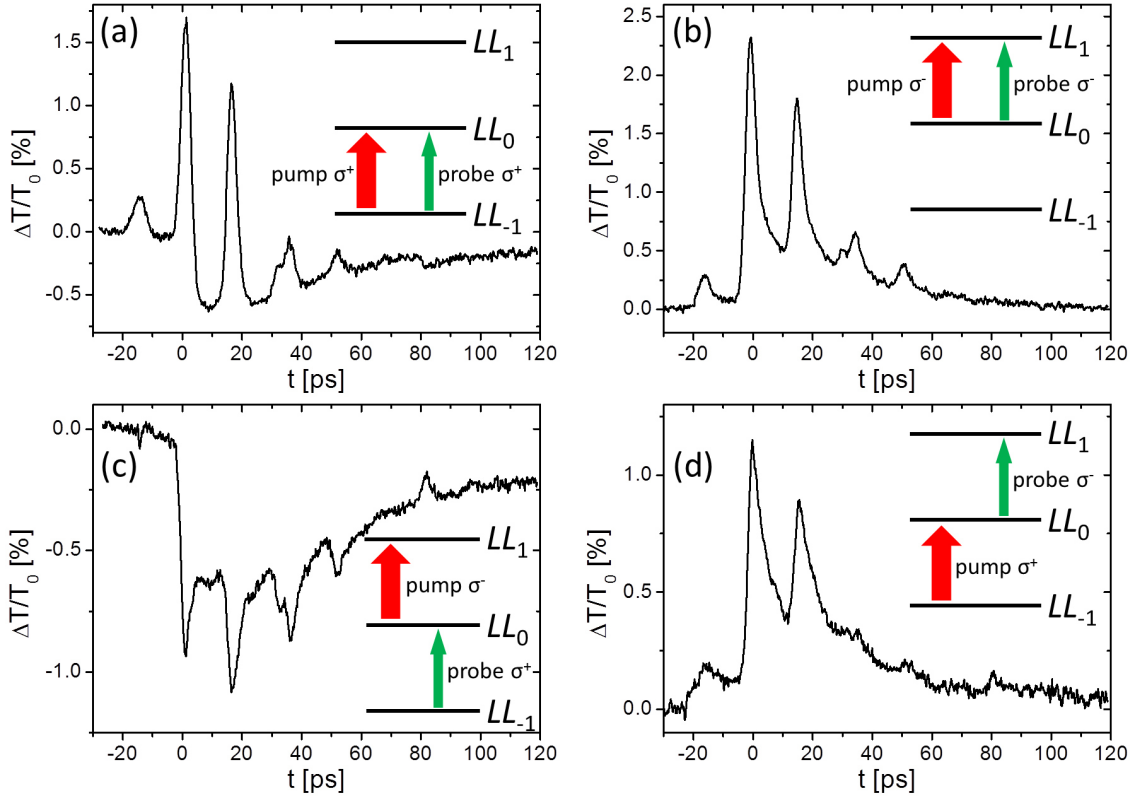
Figure 4.15.: Pump-probe signals for all four combinations of pump and probe beam polarization. The arrows indicate the different pump and probe schemes in each of the plots.

ized radiation. Three of the four signals start with a very short positive peak, only one signal starts with a negative peak. Altogether this results in a short positive peak for the measurement with linearly polarized radiation. After this initial peak, the signal in Fig. 4.15 (a) changes the sign. Therewith the signal measured with the linearly polarized radiation is a superposition of two positive and two negative signals, which cancel out each other. Thus the system that seems to be relaxed already in the linear case, is in fact not in equilibrium, but the electrons are redistributed.

To check whether the $\lambda/4$ plates have any influence to the measurement itself, for each combination of pump and probe polarization additional measurements have been performed without magnetic field. For all four combinations of pump and probe polarization the signal is the same, as expected for this case. The complex signals can be understood, if one takes into account Auger-like processes, e.g. the scattering of two electrons from the zeroth LL to the LL_{-1} and LL_1 respectively. How these processes can cause the observed signals is described in detail in the next
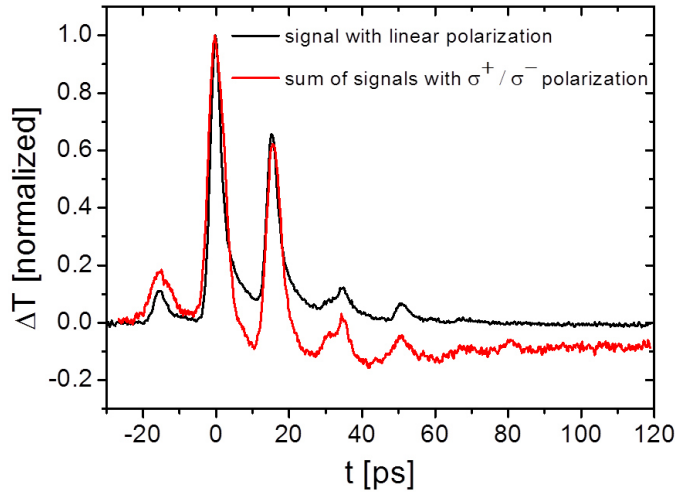
Figure 4.16.: Pump-probe signal measured with linearly polarized radiation in comparison with the sum of the four signals measured with circularly polarized radiation.

section.

4.3.3. Auger-like processes at the first Landau-level transition

The unique spectrum of the three equidistant LLs -1, 0 and 1 provides the possibility of strong Auger-like scattering processes. One possibility is the scattering of two electrons from the LL_0 to the LL_1 and LL_{-1}, while energy and momentum conservation are fulfilled. The second possibility is the inverse process, in the absence of a magnetic field also known as impact ionization. For the Auger-processes it is essential that the LL_{-1} is not completely occupied. For the inverse process the LL_1 has to be populated. Which of both processes dominates is mainly dependent on the occupation of LL_1 and LL_{-1}. This unique constellation leads to the complex pump-probe signals observed with circularly polarized radiation.

In Fig. 4.17 a scheme is shown which demonstrates how the sign reversal can occur. Immediately after pumping the lower transition, the occupation of the LL_0 increases, while the occupation of the LL_{-1} decreases. Both effects suppress the absorption of this transition, thus directly after the pump-pulse the signal is positive. The reduced population of the LL_{-1} gives rise to the Auger-processes. These processes strongly increase the population of the LL_1 and LL_{-1} while the LL_0 is depopulated partly. If these Auger processes are sufficiently efficient, this effect leads to a decreased population of the LL_0 compared to the population without pumping, which causes

73
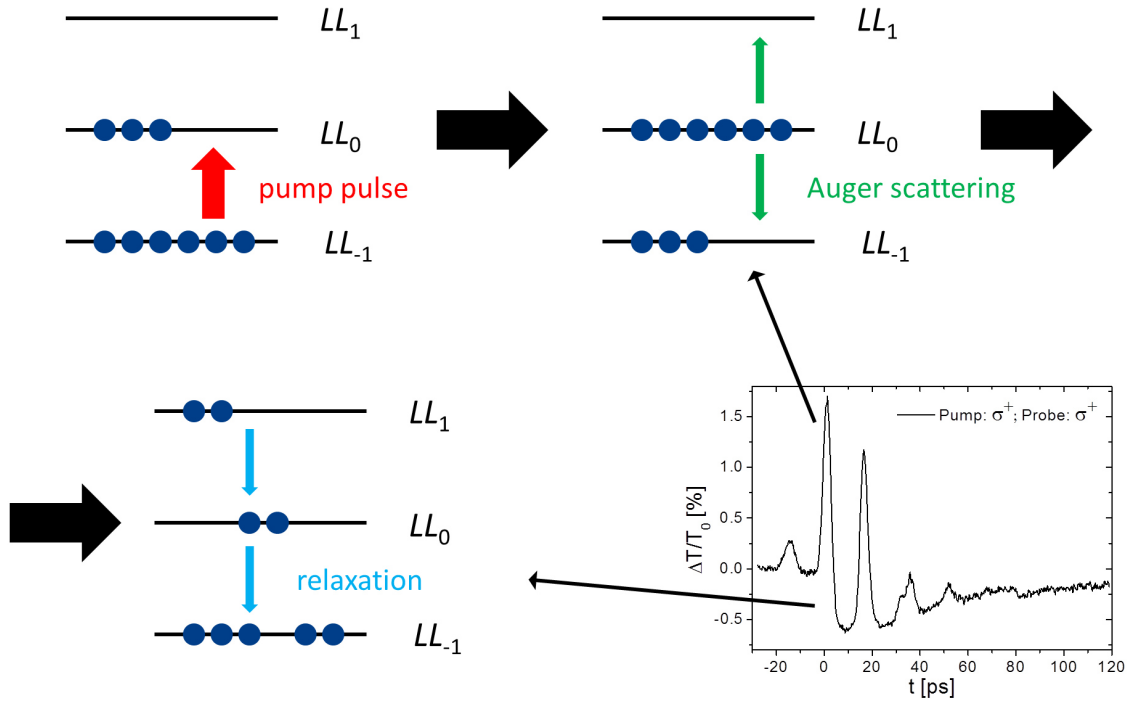
Figure 4.17.: Simple sketch for the carrier redistribution which causes the change of sign of the pump-probe signal for σ^+ polarized pump and probe beam.

a pump-induced absorption and therefore a change in sign of the pump-probe signal.

Notably these results can also provide information on the Fermi energy in the graphene layers. For a completely intrinsic graphene sheet, the four different pump-probe signals would show strictly symmetric signals. Signals measured with opposite polarization would lead to the same results (e.g. Fig. 4.15 (c): σ^--pump, σ^+-probe (d): σ^+-pump, σ^--probe). To cause this sign reversal of the signal in Fig. 4.15 (a) within 6 ps, the Auger processes have to take place extremely fast. Indeed they are so fast that the signal in Fig. 4.15 (d) is purely positive. This means that already during the pump pulse the population of the LL_0 decreases, although the electrons are excited from the LL_{-1} to the LL_0 by the pump pulse.

4.3.4. Rate-equation model

A simple three-level rate-equation model can describe the main features of the complex pump-probe signals observed in section 4.3.2. The rate equations are given by

$$\dot{N}_{LL1} = G_{\sigma-} - R_{1\to0} - R_{1\to-1} - InvAug + Aug, \tag{4.12}$$

$$\dot{N}_{LL0} = G_{\sigma+} - G_{\sigma-} + R_{1\to0} - R_{0\to-1} + 2InvAug - 2Aug, \tag{4.13}$$

$$\dot{N}_{LL-1} = -G_{\sigma+} + R_{0\to-1} + R_{1\to-1} - InvAug + Aug. \tag{4.14}$$

The relaxation rate via carrier-phonon scattering for the two possible transitions $LL_1 \Rightarrow LL_0$ and $LL_0 \Rightarrow LL_{-1}$ is described by $R_{1\to0}$ and $R_{0\to-1}$. A second rate, which accounts for the direct carrier relaxation from the LL_1 to LL_{-1}, can be added. The last two rates in Eq. 4.12 represent the Auger-like effects and describe the scattering of two electrons from the LL_0 each one the the LL_1 and LL_{-1} and the inverse process. The excitation of the electrons in the transition $LL_{-1} \Rightarrow LL_0$ ($LL_0 \Rightarrow LL_1$) is represented by $G_{\sigma+}$ ($G_{\sigma-}$) and is calculated by

$$G_{\sigma-} = G_{peak-} \cdot e^{\frac{(t-t_0)^2}{2\sigma^2}} \cdot N_0 \cdot (n - N_1) \tag{4.15}$$

and

$$G_{\sigma+} = G_{peak+} \cdot e^{\frac{(t-t_0)^2}{2\sigma^2}} \cdot N_{-1} \cdot (n - N_0). \tag{4.16}$$

The maximum excitation rate of the left or right circularly polarized pulse is represented by G_{peak}, N_i is the number of electrons in LL_i, while n stands for the degeneracy of the LLs, i.e. the maximum number of electrons that fit in to one LL. The rates for the carrier-phonon scattering ($R_{1\to0}$ and $R_{0\to-1}$) are calculated via

$$R_{1\to0} = \frac{N_1(n - N_0)}{\tau_{p1}} \tag{4.17}$$

and

$$R_{0\to-1} = \frac{N_0(n - N_{-1})}{\tau_{p1}}. \tag{4.18}$$

The time constant τ_{p1} is determined by the carrier-phonon scattering or defect mediated scattering. A second time constant τ_{p2} can be added to describe the relaxation process $R_{1\to-1}$, which can be included by

$$R_{1 \to -1} = \frac{N_1(n - N_{-1})}{\tau_{p2}}. \tag{4.19}$$

The Auger-like processes are included by Aug and $InvAug$. While Aug describes the process where two electrons from LL_0 scatter to each of the levels LL_1 and LL_0, $InvAug$ stands for the inverse process. Therefore these rates have to be doubled for the LL_0. The rate of the Auger process is calculated by

$$Aug = \frac{N_0(n_{-1} - N_{-1})}{\tau_{Auger}}. \tag{4.20}$$

For this process the two most important parameters are the number of available electrons for the scattering process in LL_0 and number of unoccupied states in LL_{-1}. If LL_1 were strongly occupied, it would also be important to take it into account, but it is neglected for these calculations. The scattering time of the Auger-like processes is given by τ_{Auger}. The inverse scattering rate is calculated by

$$InvAug = \frac{N_1(n - N_0)}{\tau_{Auger}}. \tag{4.21}$$

Similarly to the Auger-process, in the inverse Auger process the number of available electrons in LL_1 and the number of non-occupied states in LL_0 play the dominant role. In this inverse case, the number of available electrons in LL_{-1} is neglected as it would only play an important role for a very high pump fluence. With the aforementioned equations, the occupation of the three LLs during pumping and relaxation is calculated. To obtain the pump-probe signals from the occupations, a measure for the absorption probability of each transition $P_{-1 \to 0}$ and $P_{0 \to 1}$ is calculated via

$$P_{i-1 \to i} = N_{i-1} \cdot (n - N_i). \tag{4.22}$$

With this simple three-level model the main features of the pump-probe signals can be reproduced very well. The results of the model combined with the pump-probe signals are depicted in Fig. 4.18.

Immediately with the pump-pulse, the Auger-like processes start to redistribute the electrons. Which of the processes dominates in the first picoseconds depends on the polarization of the pump pulse. For a σ^+ polarized pump pulse, the Auger scattering starts, and the occupation of LL_1 increases. With increasing number of carriers in LL_1, the inverse Auger process becomes more and more important until an equilibrium between Auger and inverse Auger processes is reached. This redis-
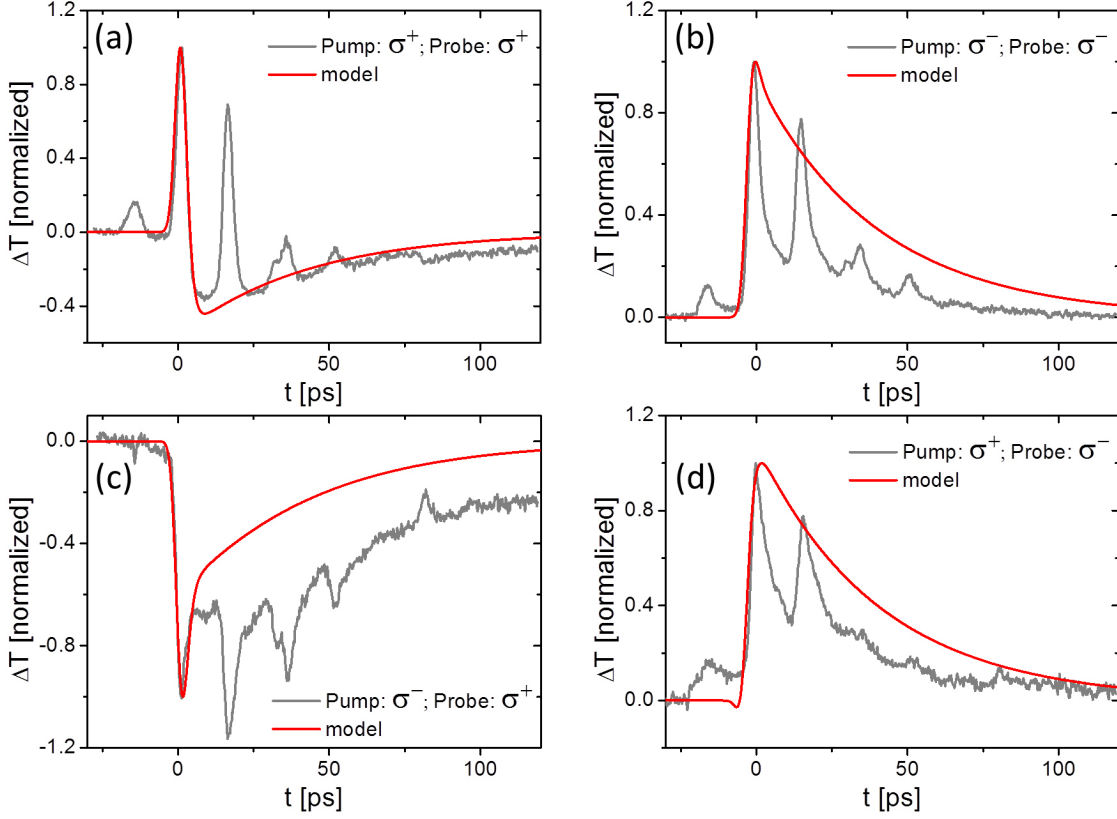
Figure 4.18.: Results of the rate-equation model for all four combinations of pump and probe beam polarization.

tribution effect can be so strong, that the occupation of LL_0 is decreased by optical pumping of the transition $LL_{-1} \Rightarrow LL_0$. As long as the Auger processes are much faster compared to the carrier-phonon scattering, only the occupation of LL_0 before the pump pulse determines whether LL_0 gets populated or depopulated during the redistribution. At negative Fermi energies, the aforementioned pump pulse leads to an increase of the occupation of LL_0, while it is decreased at positive Fermi energies. When the transition $LL_0 \Rightarrow LL_1$ is pumped, the change of the occupation of LL_0 after the redistribution changes it's sign compared to the aforementioned case. Now the LL_1 gets populated by the pump pulse and therefore enables the inverse Auger process which firstly dominates.

For the numerical solution of the rate equation model, a very simple approach was coded in $C++$. The source code of the calculation is attached in the appendix in A. With $Gpeak = 500 \, \mathrm{ps}^{-1}$ (for $n = 1000$ corresponding to $0.5 \, \mathrm{ps}^{-1}$ for $n = 1$), a change in the occupation of LL_{-1} of about 1% was reached. The two most important

parameters for the model are the initial occupation of LL_0 and the time constant τ_{Auger} for the Auger-like processes. When LL_0 is initially occupied by 50%, the pump-probe signals for σ^+ and σ^- polarized pump radiation are symmetric: The signal for σ^+ polarized pump and σ^- polarized probe radiation is identical with the signal for σ^- polarized pump and σ^+ polarized probe radiation (not shown). The asymmetry observed in the experiment can be achieved with an initial occupation of LL_0 of about 75 %. From this initial occupation one can estimate the Fermi energy without magnetic field by calculating the number of additional carriers in LL_0 from the degeneracy of the LL [7]. The degeneracy $G(B)$ is given by

$$G(B) = \frac{eB}{h}. \tag{4.23}$$

and has a value of $1.015 \cdot 10^{15}\,\mathrm{m}^{-2}$ at $4.2\,\mathrm{T}$. Taking into account the additional spin and valley degeneracy, the carrier concentration is $1.015 \cdot 10^{11}\,\mathrm{cm}^{-2}$. By integrating the density of states (cf. Eq. 1.4) in the range from zero to the Fermi energy on can calculate the carrier concentration n_c by

$$n_c(E_F) = \int_0^{E_F} g_s g_v \frac{1}{2\pi\hbar^2} \frac{E}{v_F^2}\, dE, \tag{4.24}$$

solving the integral leads to

$$n_c(E_F) = \frac{1}{2} g_s g_v \frac{1}{2\pi\hbar^2} \frac{E_F^2}{v_F^2}. \tag{4.25}$$

For a given carrier concentration, the Fermi energy is determined by

$$E_F = \sqrt{\frac{n_c 4\pi\hbar^2 v_F^2}{g_s g_v}}. \tag{4.26}$$

Therewith a Fermi energy of $37\,\mathrm{meV}$ without magnetic field is estimated.

The second important parameter τ_{Auger} is set to $1.7\,\mathrm{ps}$. This scattering processes have to be extremely fast in order to get a purely positive signal for σ^+ polarized pump and σ^- polarized probe radiation (cf. Fig. 4.18 (d)). Furthermore, the ratio of positive to negative peak in Fig. 4.18 (a), as well as the height of the shoulder in Fig. 4.18 (c) is strongly dependent on τ_{Auger}.

For the relaxation time τ_{p1}, which is mainly responsible for the slower part of the relaxation, $15\,\mathrm{ps}$ are assumed. Changes in this value only affect the slow part of the signal, the dynamics within the first part of the signal remain unchanged. The in-

fluence of relaxation processes from LL_1 to LL_{-1} are neglected in these calculations, since they play practically no visible role in the model as long as the relaxation time τ_{p2} is not extremely short. This can be explained by the small number of available electrons in LL_1 combined with the small number of non-occupied states in LL_{-1}.

4.3.5. Microscopic calculations

Triggered by our experimental findings and the insight obtained by the rate equation model, a microscopic model was developed by Florian Wendler (TU Berlin). The calculations are based on the density matrix formalism, which is described in [87,88] for the carrier dynamics without magnetic field. The Peierls substitution (cf. Eq. 4.3) was used to introduce the magnetic field into the Dirac equation. This model includes the excitation of the carriers via an optical pump pulse with a duration of $2.7\,\mathrm{ps}$, a fluence of $0.1\,\mathrm{J/cm}^2$ and a photon energy of $75\,\mathrm{meV}$, as it was employed in the experiment. The Fermi energy was set to $28\,\mathrm{meV}$, which corresponds to an occupation of $64\,\%$ of LL_0 at $4.2\,\mathrm{T}$.

To calculate the temporal evolution of the microscopic polarization and the occupation of the different LLs, Coulomb- and phonon-induced many-particle scattering processes are taken into account in these calculations. As the energy of all transition between the three lowest LL transitions is not resonant to the optical phonon energy, only very slow relaxation could be reached. Therefore, the relaxation processes via defect-induced carrier-phonon scattering is included with a fixed rate in a way that the signals fit to the experimental observations. The results obtained by the microscopic calculation in comparison with the corresponding part of the measured pump-probe signals are depicted in Fig. 4.19. In part (a) of the figure, the pump-probe scheme is depicted, while part (b) shows the expected sign of the pump-probe signals in absence of Auger processes. The focus of the microscopic modeling was the investigation of the initial relaxation processes, therefore only the first parts of the experimental signals are investigated. In the parts (c), (e), (g) and (i), only a detail of the measured data around the temporal overlap of pump and probe pulse are shown (cf. Fig. 4.15). Not only the signals that match the naive expectations (Fig. 4.19 (c) and (e)) are reproduced nicely by the microscopic calculations (Fig. 4.19 (d) and (f)), but also the unexpected purely positive signal depicted in part (g) is in very good agreement with the microscopic calculation in part (h). Even the experimental signal in part (i) can be reproduced very well by the microscopic model.
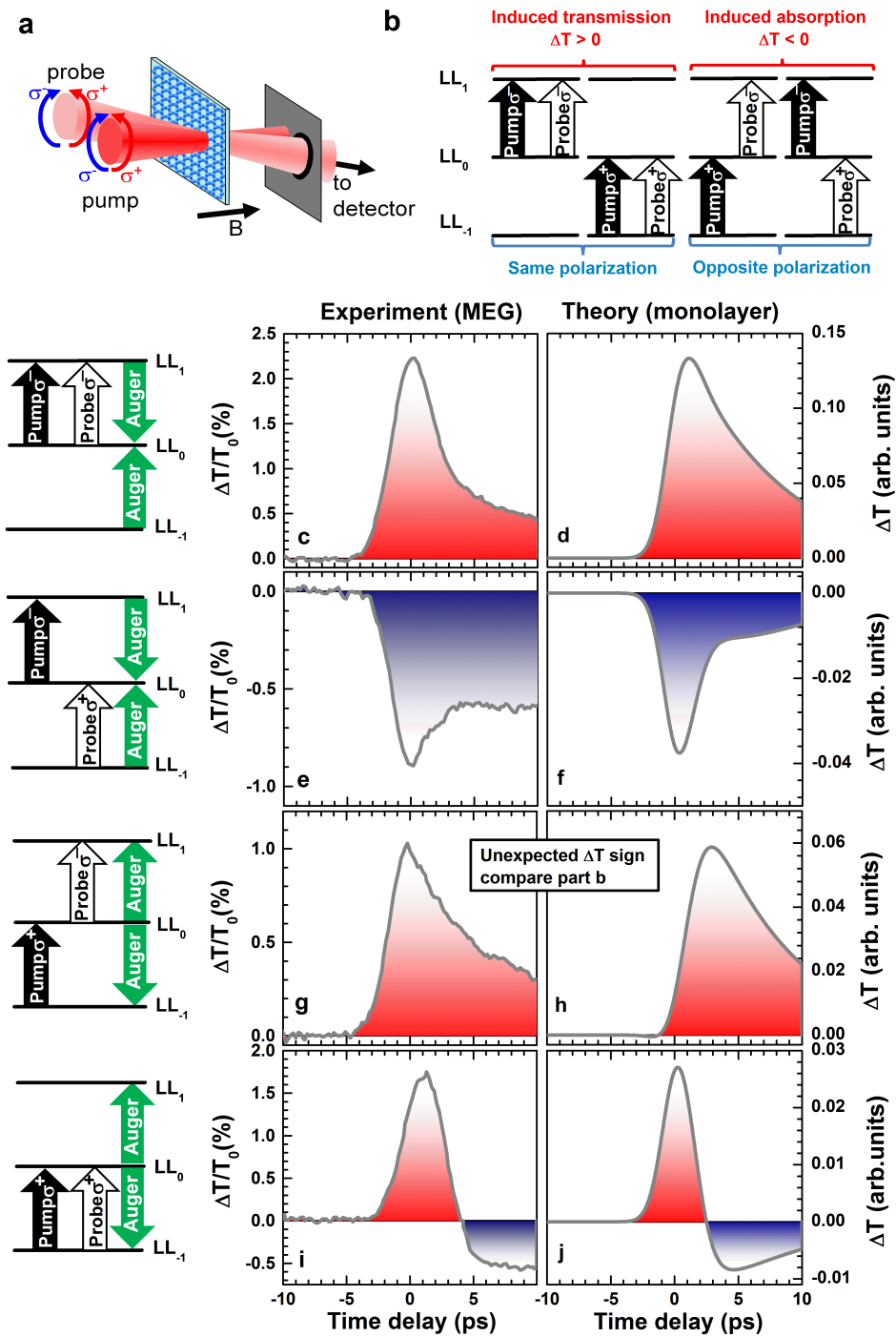
Figure 4.19.: Configuration of pump and probe polarization (a), and the expected sign of the pump-probe signals(b). In (c), (e), (g), and (i) the first part of the measured pump-probe signals is depicted, in the corresponding subfigures (d), (f), (h), and (j), the calculated pump-probe signals are depicted. Figure taken from [86].

For understanding the role of the Auger processes it is instructive to consider the temporal evolution of the involved LLs as depicted in Fig. 4.20. In part (a), the pump schema for σ^- polarized radiation is shown, the corresponding change in the occupation is plotted in part (b). The pump pulse is indicated by the vertical yellow bar around $0\,\text{ps}$. In this case, where the upper transition is pumped, the occupation in LL_1 increases while LL_0 gets depopulated. The increased occupation of LL_1 enables the inverse Auger-processes that are indicated by the green arrows in part (a), which lead to a depopulation of LL_{-1}. For the case of σ^+ polarized pump radiation, the schema and the occupations are presented in parts (c) and (d), respectively. During the first part of the pump pulse, the occupation of LL_0 increases while the LL_{-1} gets depopulated. Very shortly after the start of the pump pulse, the decreased occupation of LL_{-1} enables the inverse Auger-processes that are indicated by the green arrows in part (c). These processes lead to an increase of the occupation of LL_1 and the occupation of LL_0 starts to decrease again. These Auger-like processes are extremely efficient and even lead to a depopulation of LL_0 while the lower transition is pumped.
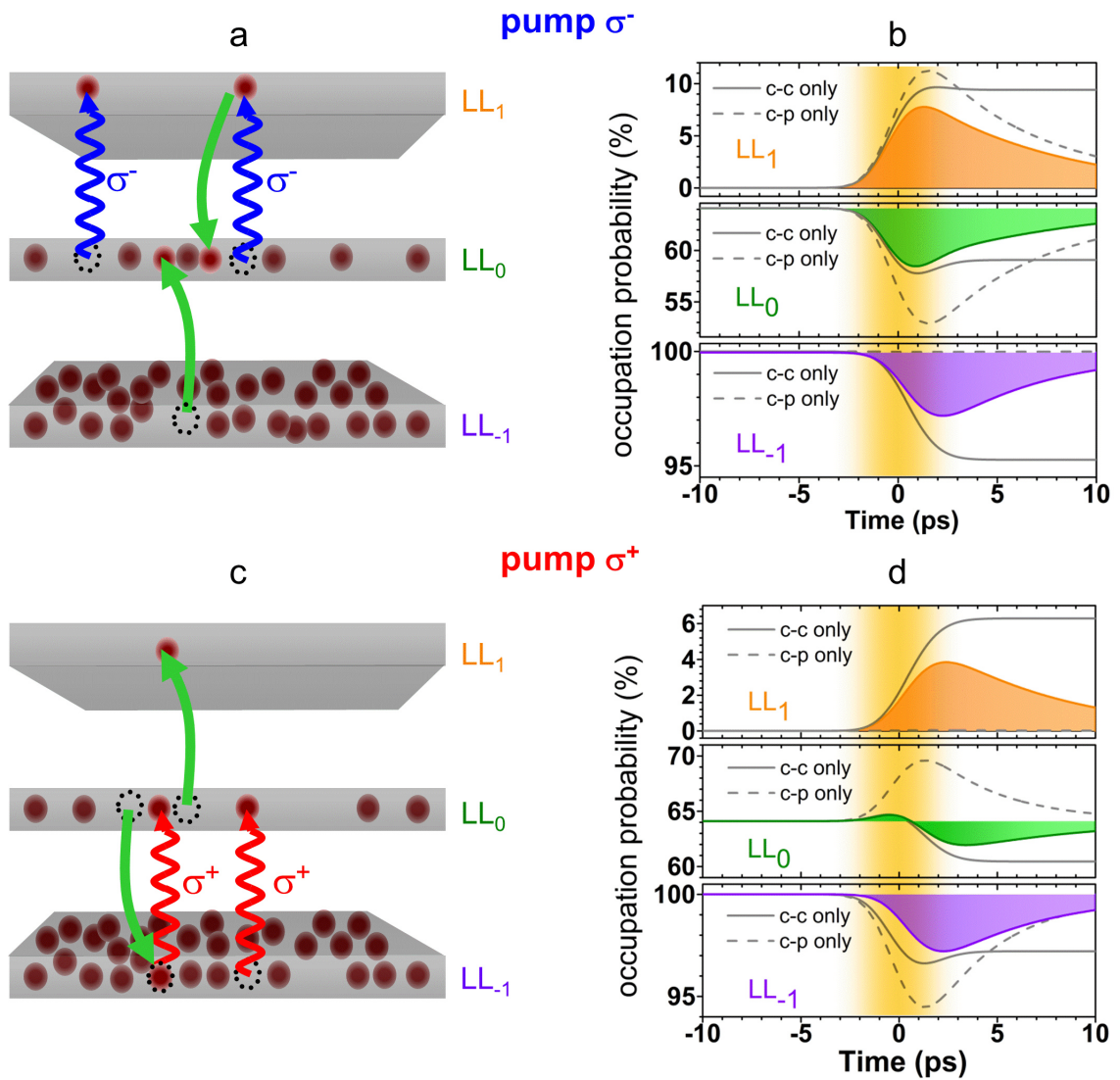
Figure 4.20.: Sketch of the effect of σ^- (a) and σ^+ (c) polarized pump-radiation to the occupation of the different LLs and the carrier redistribution via Auger-like processes (green arrows). Temporal evolution of the microscopically calculated occupation probability for σ^- (b) and σ^+ (d) polarized pump radiation. Figure taken from [86].

4.3.6. Measurements with 50 layer sample

As the results of the aforementioned measurements looked promising, but contained multiple pulses, a second set of measurements was performed under the same conditions concerning the FEL and the magnet cryostat. As a new sample from the Georgia Institute of Technology of visibly higher quality was available in the meantime, we used this new sample for the measurement. The new sample consists of about 50 layers of graphene and looks very homogeneous, while the 40 layer sample which was used for the previous measurements had already some scratches from handling. While the multiple peaks could be circumvented, the analysis of these measurements is again difficult. The high quality of the sample leads to strong coherent artifacts, which are described later in this section.

With this new sample a pump pulse energy of $1.2\,\mathrm{nJ}$ induces a maximum change in transmission of 3.4% in the absence of a magnetic field which is an enormous increase of the signal compared to the measurements on the old sample ($1.8\,\%$ at $10\,\mathrm{nJ}$). Besides the sample quality a better alignment of the setup might be responsible for this increase. The main features of the previous measurements could be reproduced with this new sample. The results of measurements with linearly polarized radiation are plotted in Fig. 4.21. The pump-induced change of the transmission is color coded depicted as a function of the delay time between pump and probe pulse on the x-axis and as a function of the magnetic field on the y-axis. This plot is dominated by the strong increase of the pump-probe signal at resonance with the transition $LL_{-1,0} \Rightarrow LL_{0,1}$ at $4.2\,\mathrm{T}$. Moreover the alignment was slightly different during the measurements with this new sample and the multiple peaks nearly vanished.

In Fig. 4.22 the fit parameters for a single exponential decay to the measured data are shown. The highest amplitude of the pump-probe signal is again observed at $4.2\,\mathrm{T}$, where the pump-probe signal is increased to $26\,\%$, which is about 8 times higher than at $0\,\mathrm{T}$. In contrast to the previous measurements, where the signals have been divided by the transmission through the sample without magnetic field, in this measurement at every field a reference measurement was performed. As the absorption of the sample is a factor of 1.5 higher at $4.2\,\mathrm{T}$ compared to the absorption without magnetic field, the amplitude of the pump-probe signal is also strongly increased. But also when the signal is divided by the transmission without magnetic field, it is increased by a factor of 5 which means a doubled effect of the magnetic field compared to the old sample.

The dependence of the relaxation time on the magnetic field of this new sample
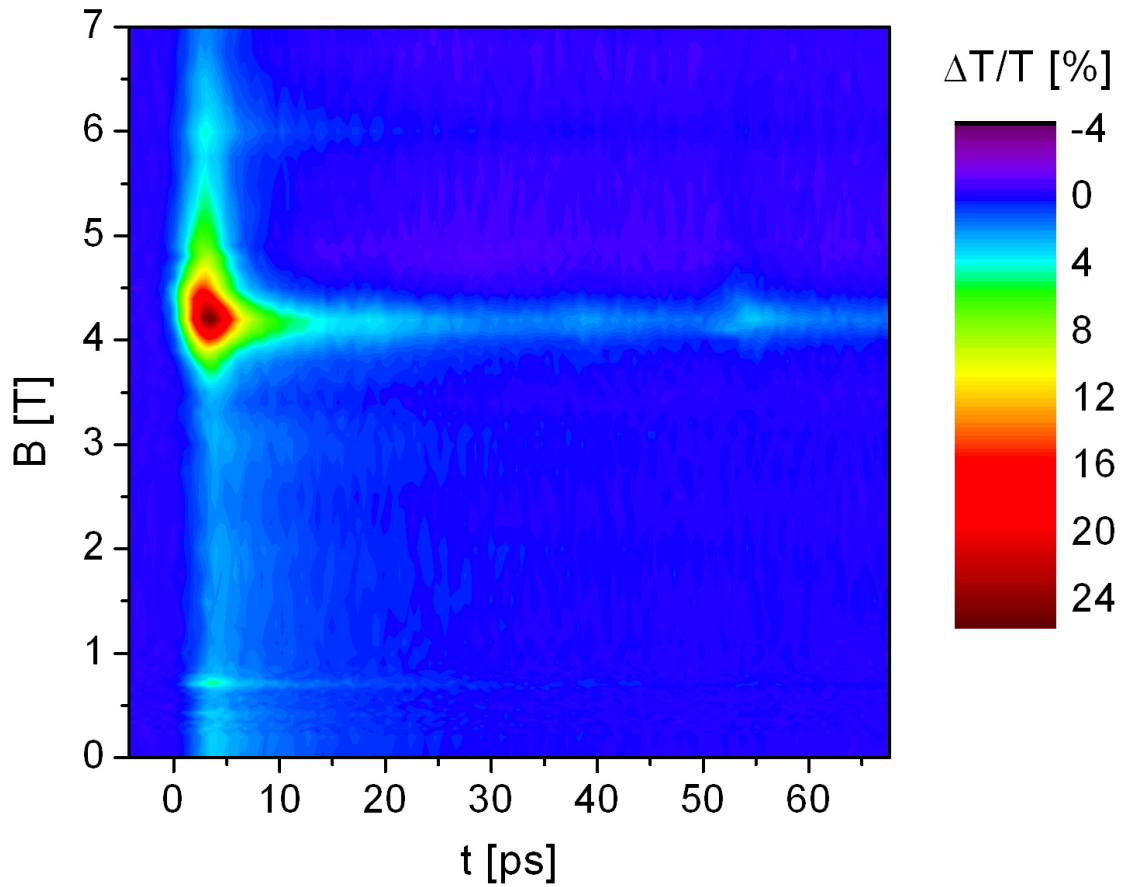
Figure 4.21.: Color coded map of the pump induced transmission change in dependence of the delay time of pump and probe pulse and the magnetic field.
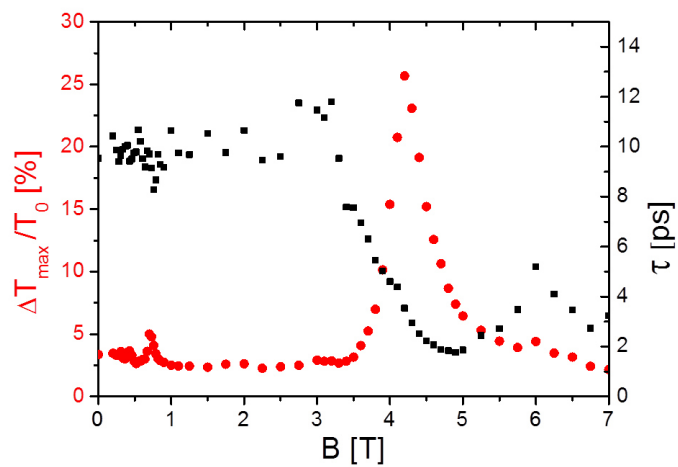

Figure 4.22.: Fit parameters for a single exponential fit for the measurements depicted in Fig. 4.21.

seems to be nearly the same as for the 40 layer sample (cf. Fig.4.14 and 4.22), but in detail there are two very important differences. Firstly, at this new measurements a dip in the relaxation time could also been observed at a magnetic field of 0.75 T, where the transition $LL_{-1,-2} \Rightarrow LL_{2,1}$ is resonant to the photon energy. Notably, at this field the dominating part of the pump-probe signal is caused by the background signal discussed in Sec. 4.3.1, but still a resonant contribution is visible. This decrease of the relaxation time can also be explained by the Auger-processes between the three lowest transitions. As the pump pulse increases the occupation of LL_1, the inverse Auger scattering between the lowest three levels is enabled. On the other hand, the depopulation of LL_{-1} enables the Auger scattering within the same levels. Which of these processes dominates is again dependent on the initial occupation of LL_0. Additional Auger-like processes, like the scattering of two electrons from LL_2 (LL_{-2}) to LL_1 (LL_{-1}) and the inverse process might occur. Another difference is the pump-probe signal at 4.2 T. In this case an extremely high maximum signal amplitude of 26 % is reached at zero time delay and the signal decreases very fast. Subsequent to this fast initial decay, the signal stays nearly constant within the observed time. This extremely slow decay can be seen by the light blue line at 4.2 T in Fig. 4.21). At slightly higher fields the signal even changes its sign after a very short positive peak (cf. the purple line at 5 T in Fig. 4.21).

Measurements with circularly polarized radiation also provided a deeper insight in the results of the measurements of the 50 layer sample. In contrast to the measurements discussed in section 4.3.2 all pump-probe signals measured with circularly polarized radiation exhibit extremely strong positive signals at zero time delay (cf. fig 4.23). The tremendous increase of the transmission for σ^- polarized pump and probe radiation exceeds even 40 % (see also Fig. 4.23 (b)), which can hardly be explained by a usual pump-probe signal. More likely, these extreme strong positive peaks represent coherent artifacts, which may also explain the higher pump-probe signal for the linearly polarized measurements compared to the older measurements. Coherent artifacts result from a grating formed by the microscopic polarization in the sample, which is induced by the probe beam radiation. Due to this grating, a part of the pump radiation is diffracted into the direction of the probe beam [89].

In Fig. 4.23 (a) and (b), also multiple peaks are visible. Those peaks might be caused by the $\lambda/4$-plates used to setup the circular polarization. About 50 ps after the initial peak, the signal seems to stay nearly constant within the observed temporal range. A long scan over the full range of the delay stage (about 1200 ps) was
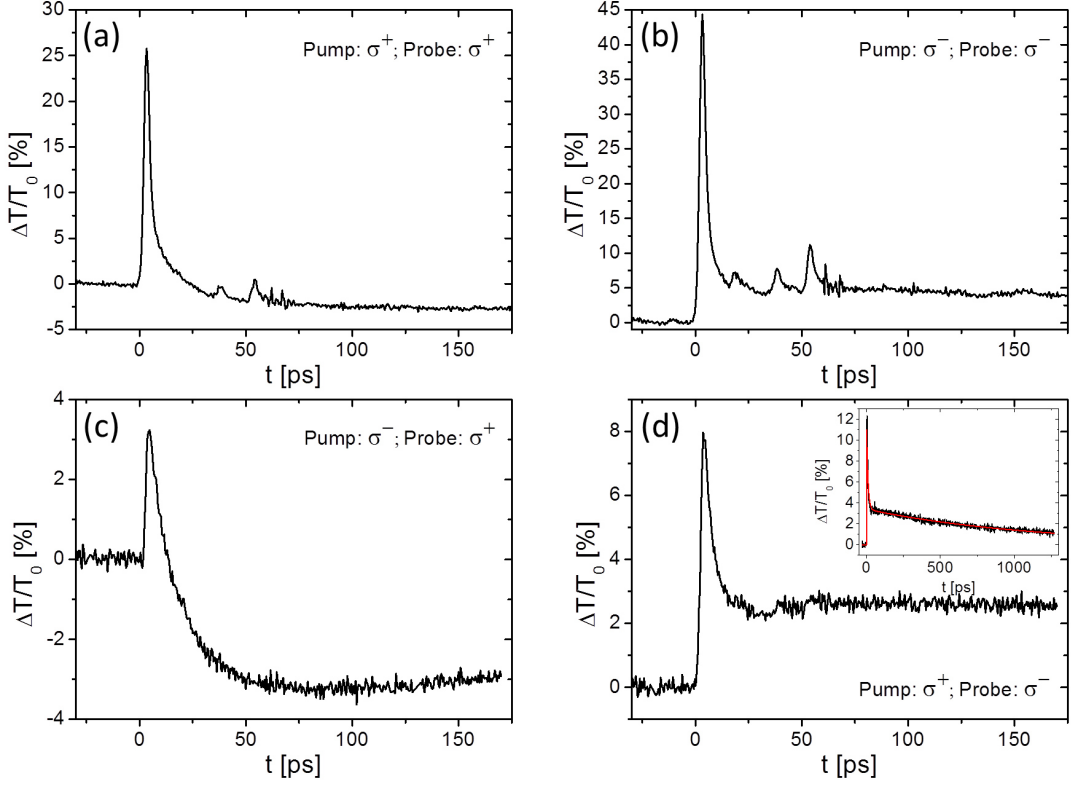
Figure 4.23.: Pump-probe signals for all four combinations of pump and probe beam polarization measured with the new 50 layer sample. The inset in part (d) shows a long measurement over the full scanning range of the delay stage together with a biexponentioal fit to determine the slow time constant.

performed to determine the relaxation time constant (see also inset of fit. 4.23 (d)). Therewith the two time constants of the pump-probe signal could be extracted by a fit function with a biexponential decay to be $\tau_1 = 9.3\,\mathrm{ps}$ and $\tau_2 = 1140\,\mathrm{ps}$.

The strong difference in the relaxation time at a magnetic field of $4.2\,\mathrm{T}$ between the new 50 layer sample and the sample with 40 layers can be explained by the sample quality. A direct relaxation via electron-phonon scattering from the LL_1 (LL_0) to LL_0 (LL_{-1}) is not possible as energy and momentum conservation could not be fulfilled. Therefore supercollisions [80] (discussed in Sec. 4.2.5) might play an important role for the relaxation as they increase the number of possible scattering channels. Interestingly the relaxation time for both sample is nearly identical without magnetic field, which was also measured in the near-infrared range. This is an evidence that for Landau-quantized graphene these supercollisions play an even more important role than without magnetic field.

5. A graphene-based terahertz detector

For two-color pump-probe experiments, as described in Sec. 3.3, it is essential to bring the pump and probe pulse at the sample position to temporal and spatial overlap. While the spatial overlap can be obtained quite simple by aligning both beams through a pin hole, finding the temporal overlap can be challenging. As long as the source of the two different pulses are naturally synchronized, as described for the OPO system, the temporal overlap can be found quite easily by measuring the optical path length with a simple ruler. But as soon as the two sources are completely independent, e.g. in experiments where the free-electron laser is used to pump a sample while it is probed by a near-infrared laser, it cannot be done that easily (e.g. [90]). In this regime it is quite simple to get both sources operating exactly at the same frequency, e.g. by synchronization with a piezo-driven mirror that controls the cavity length of a near-infrared laser. An ultra-fast detector with a risetime in the ps range is required to set the temporal overlap at the sample position. Furthermore this detector should work at room temperature, it should be easy to handle and robust. The attempts to develop such a detector based on graphene are presented in this chapter.

In the first part of this chapter, a very brief overview of some recent publications is given. In the following parts, the design of a simple, graphene-based detector as well as its capabilities are presented. Further improvements of the devices by changing the substrate material is described afterwards. In the last part of this chapter, the performance of the devices is compared to other detectors, as well as an outlook on possible improvements, e.g. by changing the contacts of the antenna, is discussed.

5.1. Recent publications on graphene-based detectors

With its universal absorption in a wide spectral range graphene can serve as an interesting broadband detector material. Furthermore, the high mobility and the fast carrier relaxation enable one to develop ultra-fast optoelectronic devices. Due to these unique properties a rapid development of graphene-based detectors has taken place recently. Since the number of publications on graphene-based detectors is very large, only a small part can be discussed within this section. In 2010, an ultra-fast detector for the near-infrared range was demonstrated [19]. A graphene flake was contacted by an interdigitated structure made of two different metals, which induces the asymmetry needed to generate a photocurrent. Müller et al. could demonstrate a communication setup with frequencies of up to 16 GHz. Despite the low absorption of a single layer of graphene, they reported a responsivity of 1.5 mA/W. To further increase the responsivity of such detectors, Konstantatos et al. presented a hybrid device made of graphene combined with quantum dots [91]. They demonstrated extremely high responsivity in the range of 10^7 A/W, by exploiting the extremely high absorbance of a film of colloidal quantum dots on top of the graphene. The holes of the excited electron-hole pairs tunnel very fast into the graphene sheet, the remaining electrons cause a very high doping of the graphene layer. Yet the price for this high responsivity is a very slow response time in the order of 10 ms. A detailed study about the origin of the photocurrent in the near-infrared range has been published by Freitag et al. [92].

The accessible wavelength range of graphene-based devices was very recently increased to the mid-infrared range by Herring et al. [93]. They combined a graphene flake with two gate regions, with which they could get a tunable p-n junction and demonstrated response at $10.6\,\mu$m. Two detectors for the THz range, made of graphene-based field-effect transistors, have been reported in 2012: Yan et al. [94] presented a dual-gated bilayer of graphene working at low temperatures. In the bilayer graphene a tunable bandgap could be induced by the gating. This bolometer was able to work at frequencies of up to 1 GHz. In contrast to this, Vicarelli et al. [20] reported a logarithmic-periodic antenna coupled to a rectifying field-effect transistor detecting THz radiation at room temperature. With this detector they demonstrated fast imaging using continuous wave radiation at a frequency of 0.3 THz. A similar device, based on bilayer graphene, was also presented [95]. Very recently a review article about graphene-based bolometers was published [96].

The detector presented in this thesis combines high-speed performance with broad-band THz response at room temperature. A part of this work was published in [97].

5.2. Design and fabrication of the detector

The devices consist of a graphene flake that is connected to a broad-band logarithmic-periodic antenna. While the design of the detector was developed in our group, the exfoliation of the graphene flake and the patterning of the antenna was done by Josef Kamann as cooperating partner in Regensburg. A graphene flake, produced by mechanical exfoliation of graphite, is deposited on a Si wafer with 300 nm SiO$_2$ on top. The single-layer property of the flake was proved by Raman spectroscopy (see Fig. 1.5). These single-layer flakes of graphene are usually quite small with a length and a width of approximately 10 μm. Compared to this small flake, the spot size of a focused FEL beam with a diameter of about 500 μm is rather large, so only a very small part of the radiation would get absorbed. To get a sufficient coupling of the THz radiation to the graphene flake, a logarithmic-periodic antenna was attached to the flake. While the outer diameter of the antenna is 1 mm, the inner diameter is 10 μm (see Fig. 5.1). The design of the metallization for the antenna and the contact pads is depicted in Fig. 5.1. For wavelengths smaller than the smallest structures of the antenna the radiation can couple directly to the graphene flake sufficiently, as in this case the focus diameter can get small enough.
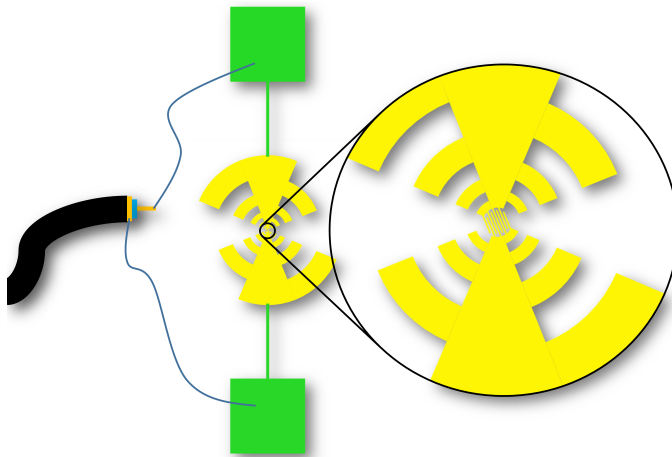

Figure 5.1.: Design of the metallization for the antenna. The green parts are the contact pads with connection to the outer part of the antenna, the yellow parts are the two arms of the antenna.

A first set of devices was fabricated with a single metallization for both arms of the antenna on a high resistive substrate ($10\,k\Omega$cm). The two arms of the antenna consist of $5\,nm$ of Ti with $60\,nm$ Au on top. Without the Ti the wetting of the Au on the substrate would be bad. The patterning of the antenna was performed by electron-beam lithography. An optical image of the inner part of the antenna, as well as an image taken with an atomic-force microscope can be seen in Fig. 5.2. For the electrical connection two contact pads with a size of $500\,\mu$m x $500\,\mu$m are placed outside of the antenna. These pads are connected on one side via strip lines ($500\,\mu$m long, $20\,\mu$m wide) to the outermost parts of the antenna, on the other side to a coaxial signal cable with an impedance of $50\,\Omega$ and a SMA connector via short wires (see also Fig. 5.1). They are glued to the contact pads with a conductive epoxy. The resistance of the devices is in the range of $100\,\Omega$.

(a)   (b)
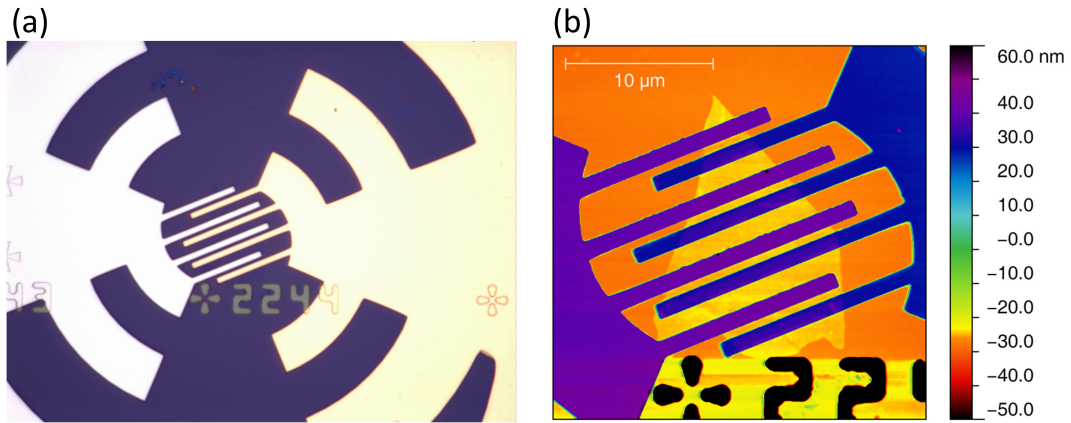
Figure 5.2.: (a) Inner part of the antenna with interdigitated structure; (b) AFM image of the interdigitated structure with the graphene flake: The blue and violet parts are the contacts, the graphene flake is diamond-shaped in yellow. Figure taken from [97] [1].

For a second set of devices the substrate material was changed to low resistive substrate with a resistivity of $5\,m\Omega$cm. Furthermore the two arms of the antenna consist of different metals: One arm is made of a Pd layer with a thickness of $60\,nm$ while the other one is made of $40\,nm$ of Au on top of $20\,nm$ of Ti. This asymmetry should maximize the photocurrent in the near infrared range. The low resistive substrate was intended to enable back gating of the graphene flake. However,this was not possible due to a leaky SiO_2 layer.

---

[1]Figures 5.2, 5.4, 5.9, and 5.10 are reprinted with permission from M. Mittendorff, S. Winnerl, J. Kamann, J. Eroms, D. Weiss, H. Schneider, and M. Helm, "Ultrafast graphene-based broadband THz detector", Appl. Phys. Lett. **103**, 021113 (2013). Copyright 2013, AIP Publishing LLC.

5.3. Time-resolved measurements at FELBE

In order to find the temporal overlap of two different laser pulses, the high speed performance of the devices is essential. To verify the high-speed response of the detectors, time resolved measurements were performed at the free-electron laser (FEL) FELBE at Dresden-Rossendorf in a wide wavelength range. For these measurements, the FEL beam was focussed to the detector by an off-axis parabolic mirror. The electrical output of the detector was directly measured with an ultra-fast sampling oscilloscope with a signal bandwidth of 30 GHz. A bias voltage of up to 200 mV could be applied to the graphene flake with Keithley sourcemeter via a bias tee. To increase the signal-to-noise ratio, for some measurements a high frequency amplifier (Miteq AFS4; gain: 50) was used.

In combination with the amplifier, signal amplitudes of up to 50 mV could be reached in a wide spectral range from 30 μm to 230 μm. With this strong signal, the timing of the FEL pulse can be set easily. In Fig. 5.3 (a) and (b), the obtained signals from a device on highly resistive substrate are depicted at two different horizontal time scales. These measurements were performed at a wavelength of 45 μm and a pulse energy of 45 nJ. While the high frequency response of a single pulse is revealed in part (a), the very long scale of part (b) represents two sequential FEL pulses with a repetition rate of 13 MHz. Notably, the noisy ground line in part (b) is not caused by noise of the detector, but by a phase stable parasitic signal at a frequency of 1.3 GHz, which is most likely caused by the electron linear accelerator that drives the FEL. The secondary pulse, which can be seen in part (a), is caused by internal reflection on the wiring of the device.

One detector on high resistive substrate as well as one detector on low resistive substrate were measured under identical conditions to investigate the influence of the substrate. A comparison of both signals is depicted in Fig. 5.4. The signal in part (a) is obtained with a device on high-resistive substrate without applied bias voltage or amplification. The rise time of the signal is 50 ps, which is easily fast enough to set the temporal overlap in two-color experiments. The pulse duration of the measured signal was about 100 ps. As the responsivity of the device is about 5 nA/W at all measured wavelengths, the resulting signal is below 1 mV. By applying a bias voltage and the high frequency amplifier, the amplitude of the signal could be increased to about 50 mV (cf. Fig. 5.3 (a)). In part (b) of Fig. 5.4, the signal obtained with the device on low-resistive substrate is depicted. Without bias voltage and amplifier,
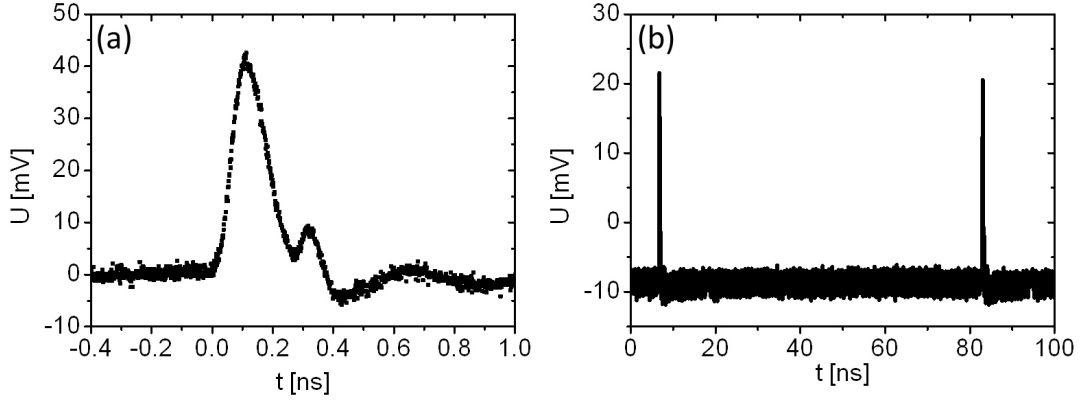
Figure 5.3.: (a)Detector signal at a wavelength of $42\,\mu$m and a pulse energy of $45\,$nJ, amplified by a high frequency amplifier. The secondary pulse is caused by reflection on the wiring.(b) Two FEL pulses measured at a wavelength of $88\,\mu$m and a pulse energy of $13\,$nJ.

no signal could be observed at all. By applying a bias voltage of about $100\,$mV in combination with the amplifier, a signal amplitude of $2\,$mV could be observed. To get a better comparability of the two substrates, the measured voltage was divided by the gain of the amplifier (50), which results in a signal amplitude of $40\,\mu$V. In comparison to the device on high-resistive substrate, the rise time ($100\,$ps) as well as the pulse duration ($1\,$ns) are strongly increased. This strong decrease of the high-speed performance can be explained by an increase of the RC time constant of the device: Combined with the low-resistive substrate, the two arms of the antenna form two capacitors which are connected in series. As the design of our logarithmic periodic antenna is self complementary, the area A of one arm of the antenna is a quarter of the area of a circle with a diameter of $1\,$mm. The SiO_2 serves as dielectric material with thickness d of $300\,$nm and a relative permittivity ε_r of 3.9. Assuming a perfectly conductive substrate, the capacitance of one arm of the antenna can be calculated via

$$C = \frac{\varepsilon_0 \varepsilon_r A}{d} \tag{5.1}$$

to be $22.6\,$pF. As the whole device consists of two identical arms that form two capacitors connected in series, the capacity of the whole device is about $11\,$pF. This capacitance, in combination with $50\,\Omega$ input resistance of the amplifier, results in a RC time of about $0.6\,$ns. Notably, the area below the measured pulses is similar, which also indicates that the number of electrons is similar for both devices and

the change in performance is only caused by the change of the RC time. This is further verified in time-integrated measurements, as here the measured photocurrent of both devices is also identical.

For the devices on high-resistive substrate, no fast signals could be measured at wavelength below $20\,\mu$m. The devices on low-resistive substrate remained untested under these conditions due to there poor high-speed performance. Remarkably, the time-integrated photocurrent, which is discussed in detail in the next sections, remains constant compared to measurements at larger wavelengths. Therefore, most probably the device gets heated strongly due to phonon absorption in the Si substrate. When the substrate is heated up to about 100°C, the number of thermally induced free carriers in the substrate increases strongly, which would lead again to a strong increase of the RC time of the device.
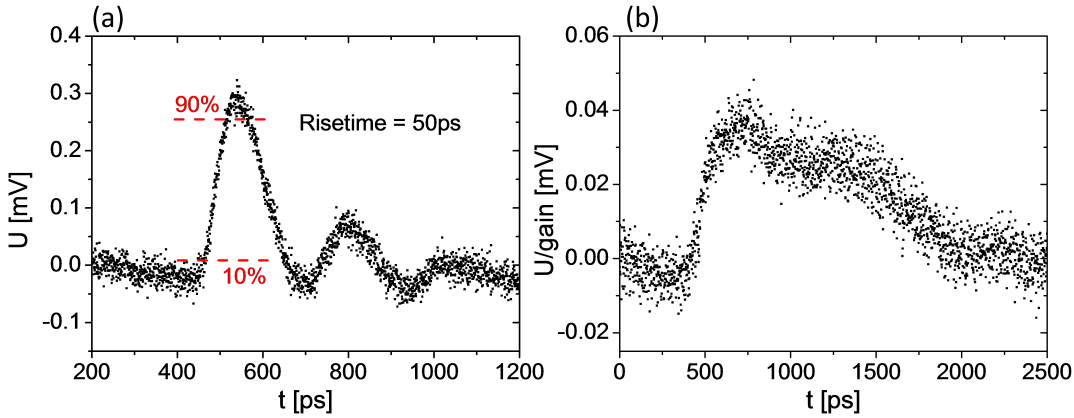
Figure 5.4.: (a) Signal shape measured with a device on high-resistive substrate at a wavelength of $68\,\mu$m and an average FEL power of $72\,$mW. For this measurement neither a bias voltage was applied, nor was the high speed amplifier used. (b) Signal shape measured with a device on low-resistive substrate. A bias voltage of $0.1\,$V was applied, additionally the high frequency amplifier was employed. For a better comparison, the voltage was divided by the gain (50) of the amplifier. Figure taken from [97].

The bias dependence of the signal amplitude for the fast detectors (on high-resistive substrate) is depicted in Fig. 5.5. The amplitude of the detected signal is proportional to the applied bias voltage with an additional offset, which means that a signal can be measured without applying a bias voltage. For this signal without bias voltage two different explanations are possible. Due to an intrinsic asymmetry in the graphene flake, e.g. by inhomogeneous doping from the substrate or inhomogeneous antenna contacts, the photocurrent might be generated directly.

This seems to be rather unlikely as the devices with two different metals for the two arms of the antenna show similar dependence on the bias voltage. On the other hand, an internal bias voltage could be generated by a thermoelectric effect: A thermoelectric circuit could be formed by the different metals, e.g. from the inner and outer wire of the coaxial cable, combined with a difference in temperature caused by the high average laser power. The signal can be nearly completely suppressed at a bias voltage of about -25 mV. Below this bias voltage the sign of the detector signal switches to negative.
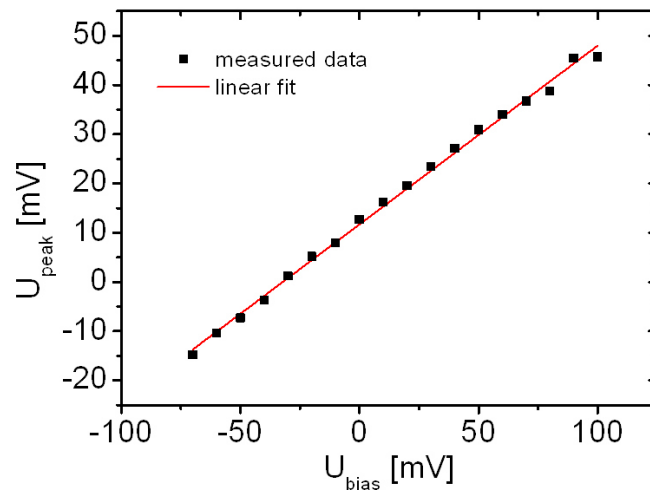
Figure 5.5.: Amplitude of the amplified detector signal of the fast detector as a function of the bias voltage.

5.4. Time-resolved measurements with gas lasers

New devices were tested at wavelengths beyond $230\,\mu$m with THz gas lasers at the University of Regensburg. They provide pulses of about 200 ns duration with a repetition rate of 1 Hz. The first measurements were performed at a wavelength of $148\,\mu$m, as the gas laser has a very high output power at this wavelength and the detector was expected to work fine, too. The average of 300 pulses was recorded to increase the signal-to-noise ratio. Furthermore, an amplifier with a gain of 100 was used for all measurements. A photon-drag detector was used as reference to measure the pulse shape. In Fig. 5.6, the averaged pulse shape of 300 measurements obtained with the photon-drag detector (a) and the graphene-based device (b) are depicted. The result of a single-shot measurement is shown in the inset of part (b).
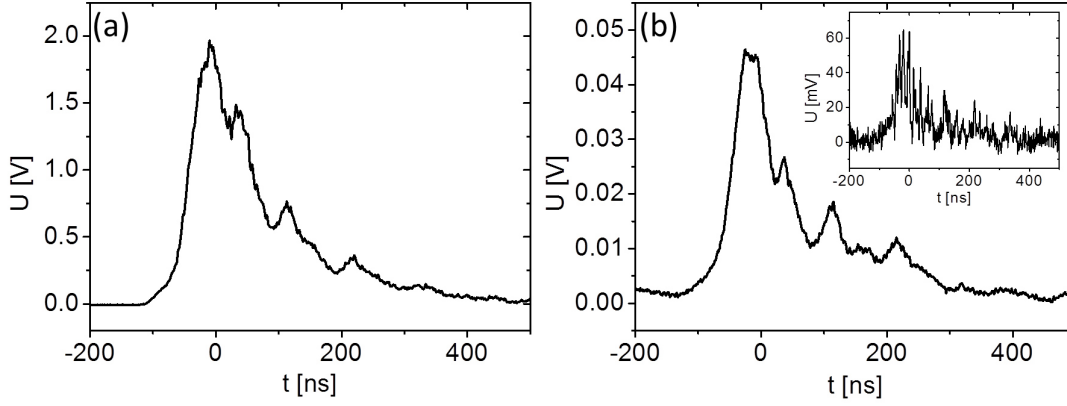
Figure 5.6.: (a) Pulse shape of the THz gas laser at a wavelength of $148\,\mu$m and a peak power of about $55\,$kW, averaged over 300 pulses, measured with a photon-drag detector. (b) The same pulse as in (a), but measured with the graphene-based device on high resistive substrate. In the inset a measurement of a single pulse is shown.

The signal shape is nicely reproduced by the measurement with the graphene based device. Small deviations between the measurements can be explained by the variations of the pulse averaged pulse shape of different measurements. The pulse shape of a single pulse contains in fact a large number of very short pulses (cf. inset of Fig. 5.6 (b)). These very short pulses can vary strongly in their temporal distribution as well as in their height, while the averaged pulses stay roughly constant. The responsivity of this device at $148\,\mu$m is $0.3\,$nA/W, which is about ten times smaller compared to the measurements with previous devices discussed in Sec. 5.3. This might be partly caused by usual deviations between the different devices, but also the spot size was larger than the outer diameter of the antenna. Due to a bad multimode structure of the beam, the spot size at the detector position was more than $2\,$mm, so only a part of the pulse energy could be coupled to the graphene flake. Notably, the performance of devices on low-resistive substrate is now the same as of the devices on high-resistive substrate. This can be understood as the pulse duration is longer than the RC time constant of the devices on low-resistive substrate. Even at a wavelength of $496\,\mu$m, which was the maximum wavelength of the gas laser, the signal could be observed with the graphene-based devices. In Fig. 5.7 (a), the shape of the average of 300 pulses, measured with the photon-drag detector, is depicted. Again, the pulse shape can be nicely reproduced by the measurement with the graphene-based detector (see Fig. 5.7 (b)), but in comparison to the measurement at $148\,\mu$m, the responsivity is increased by a factor of 10. This

increase can be explained by the increased intraband absorption at small photon energies. Therefore the longest wavelength that can be measured with this detector is expected to reach above 1 mm.
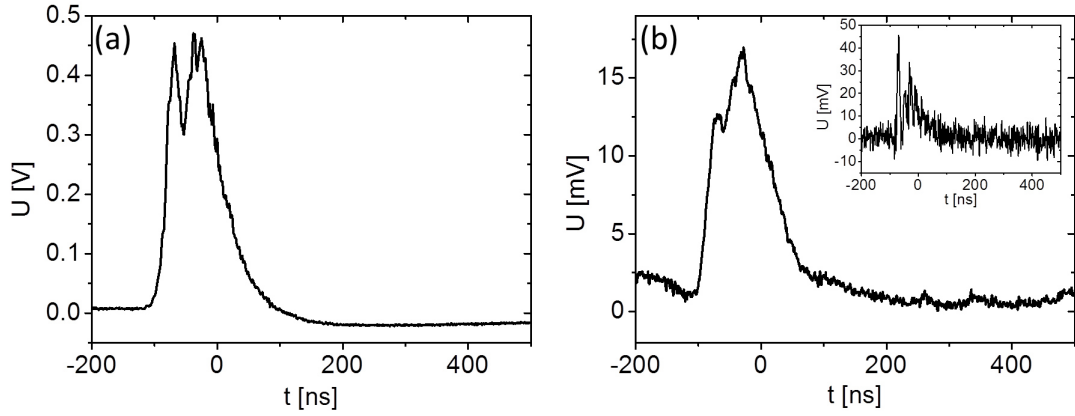
Figure 5.7.: (a) Pulse shape of the THz gas laser at a wavelength of 496 μm and a peak power of about 1.2 kW, averaged over 300 pulses, measured with a photon-drag detector. (b) The same pulse as in (a), but measured with the graphene-based device on high resistive substrate. In the inset a measurement of a single pulse is shown.

5.5. Influence of near-infrared radiation to the THz detection

To investigate the influence of the free carriers in the substrate, a detector was illuminated with near-infrared radiation while the THz pulses were measured. A Ti:sapphire laser, which was not synchronized to the FEL, served as a radiation source. The radiation was applied collinearly with the THz radiation, but not focussed to the detector. A spot of about 3 mm was illuminated to cover the whole area of the antenna homogeneously. In Fig. 5.8 (a) one can see the detector signal without near-infrared excitation compared to excitation power of 5 mW and 20 mW. The amplitude of the signal decreased approximately logarithmically as the near-infrared excitation power is increased (see also Fig. 5.8 (b)). As the detector signal is decreased already at very small near-infrared power, heating can be neglected. Also an increase of the capacitance of the antenna appears to be negligible as the rise time as well as the pulse duration is not changed. Therefore this effect seems

to originate from an electrical short-cut of the device which is caused by the increased number of photo-excited carriers in the Si in combination with the leaky oxide. Hence, a device for the spectral range from near-infrared to THz radiation should ideally be placed on a substrate that is transparent in the desired wavelength range, e.g. SiC or diamond.
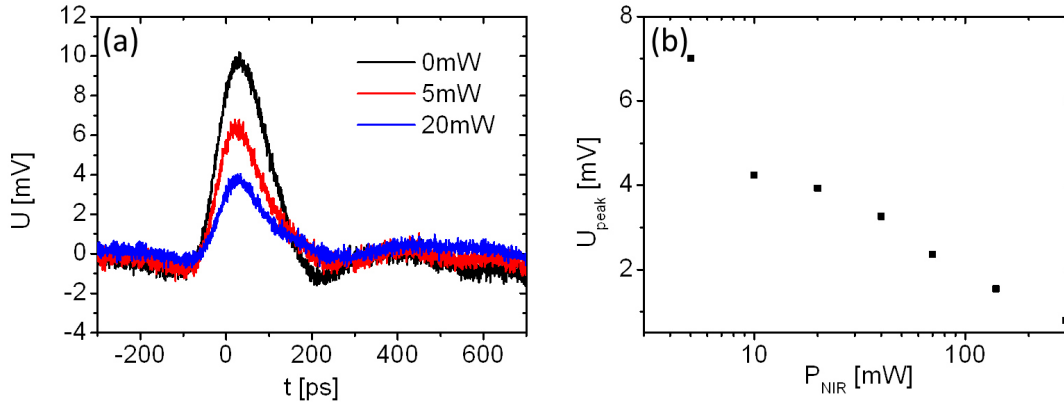
Figure 5.8.: (a) Detected signals at a wavelength of $88\,\mu$m with additional near-infrared radiation. (b) Signal amplitude as a function of the near-infrared excitation power.

5.6. Saturation behavior of the detector and autocorrelation measurements

The saturation behavior of the devices was investigated by time-integrated measurements. In these measurements, the photocurrent was directly measured with a lock-in amplifier in current mode. A mechanical chopper provided the necessary modulation of the laser beam for the lock-in technique. This technique allows one to measure the very low photocurrent, even at the lowest average powers of $1\,$mW. At wavelengths below $20\,\mu$m the photocurrent increased linearly with the applied FEL power, no saturation could be observed for average powers of above $100\,$mW. With increasing wavelength, and therefore decreasing photon energy, the saturation became more pronounced. This behavior can be understood as the density of states increases linearly with the energy in graphene. In contrast to the time resolved measurements there was no significant difference in the time integrated photocurrent for the two different substrates. In Fig. 5.9 (a), the time-integrated photocurrent is depicted as a function of the FEL pulse energy. To reveal the saturation energy E_{sat},

the function described by Eq. 3.2 was fitted to the measured data. The saturation pulse energy as a function of the photon energy is plotted in Fig. 5.9 (c). The signal saturates only slightly at the wavelength of 31 μm, which corresponds to the photon energy of 40 meV, resulting in the large error bar. In Fig. 5.9 (b), the responsivity of the detectors is plotted as a function of the photon energy. As one can see, the responsivity stays roughly constant in the whole energy range.
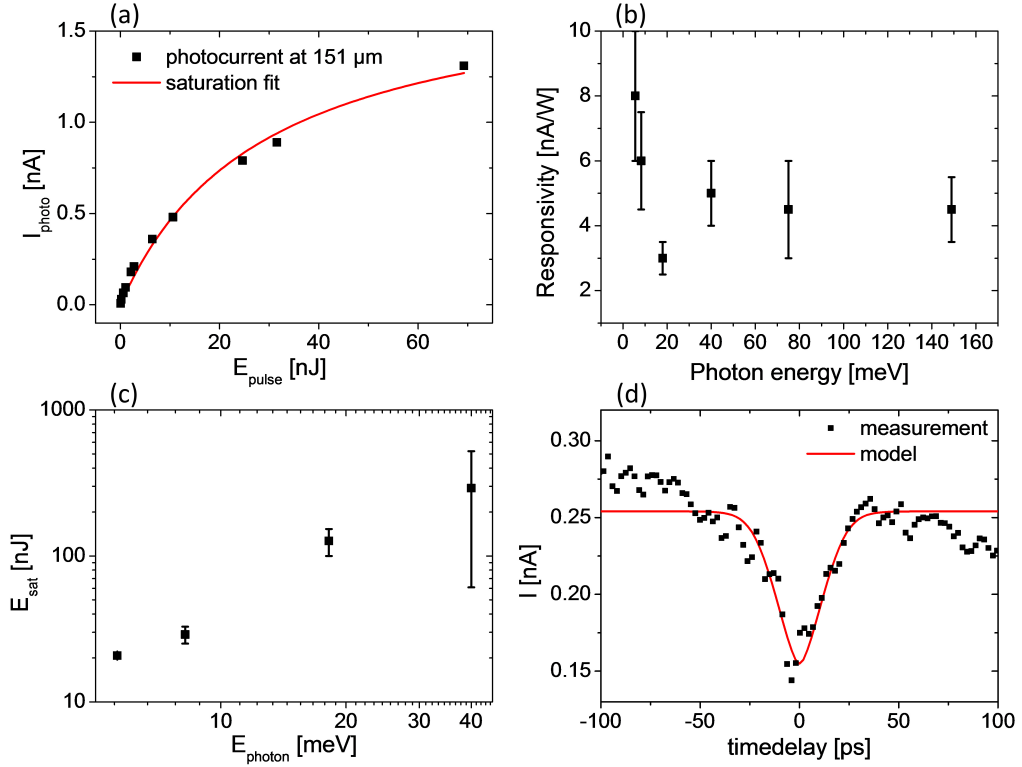
Figure 5.9.: (a) Time-integrated photocurrent as a function of the FEL pulse energy at 151 μm. (b) Responsivity measured with the lock-in amplifier at different photon energies. (c) Saturation pulse energy E_{sat} as a function of the photon energy. (d) Autocorrelation signal at a wavelength of 42 μm and a FEL-pulse duration of 7 ps. Figure taken from [97].

Due to the strong saturation at low photon energy, the devices can be exploited as nonlinear detectors for autocorrelation measurements [98]. For these measurements, each FEL pulse is split up into two pulses with nearly the same power and recombined at the detector position. Similar to the pump-probe measurements, the temporal delay between the two pulses is controlled with an optical delay stage. The time-integrated photocurrent $\bar{I}$ is measured with a lock-in amplifier as a function of this temporal delay. When the photocurrent increases linearly with the

applied pulse power P, the measurement at temporal overlap leads to the same photocurrent as compared to the photocurrent caused by two individual pulses ($I(P_1 + P_2) = I(P_1) + I(P_2)$). In contrast to this, the photocurrent decreases at the temporal overlap when the detector is strongly saturated. In a fully saturated detector, the photocurrent remains the same when the pulse power is doubled ($I(P) = I(2P)$). Therefore the signal at temporal overlap is equal to the signal of a single pulse, while both pulses can contribute to the time-integrated photocurrent as long as they are completely separated ($I(P_1) + I(P_2) = 2\,I(P_1 + P_2)$). This leads to a strong dip of the photocurrent at zero time delay.

In our case, the response of the detector is characterized by a strong saturation. Hence, it is possible to determine the intrinsic speed of the device by autocorrelation measurements. If the intrinsic speed of the device is high enough, these measurements allow one to analyze pulse shapes of laser pulses shorter than 50 ps. Two main points limited the temporal resolution of these measurements. On the one hand the pulse duration of the FEL pulse itself determines the pulse shape of the autocorrelation signal. When the intrinsic speed of the detector is in the range of the pulse duration or shorter, the autocorrelation signal is the convolution of the FEL pulse with itself. Assuming a Gaussian pulse, the width of the autocorrelation signal would be $\sqrt{2}$ times the pulse duration. On the other hand the setup increases the measured pulse duration due to internal reflections in the beamsplitters. Si wafers with a thickness of 300 μm were used as beamsplitters to get a sufficiently strong reflection, but they cause strong replica by multiple internal reflections. This results in an elongation of the pulse by the replica of the first pulse, which are delayed by 7 ps and have an amplitude of about 25 % with respect to each preceding pulse. Altogether the time resolution in our setup is about 10 ps. An intrinsic speed of the detector which is slower than the temporal resolution causes a broadening of the measured autocorrelation signal, where no interference fringes can be observed. As with this detector no such broadening could be observed, the intrinsic response time has to be comparable to or smaller than 10 ps.

5.7. Angle dependence of the photocurrent

The coupling of the antenna to the graphene flake was verified by measurements of the time-integrated photocurrent in dependence on the angle between the polarization of the radiation and the antenna. In Fig. 5.10, the photocurrent is depicted

as a function of the aforementioned angle. A strong angle dependence could be observed for the longer wavelengths. Furthermore the angle of the maximum photocurrent is different at different wavelengths, as the antenna structures, to which the radiation couples, change. This proves the coupling of the radiation through the antenna to the graphene flake. For wavelength below $20\,\mu$m no significant maximum of the photocurrent could be observed. This behavior is expected as the antenna is only important for the long-wavelength radiation. The spot size of the focus for the short wavelengths is sufficiently small for a direct coupling of the radiation to the graphene flake.
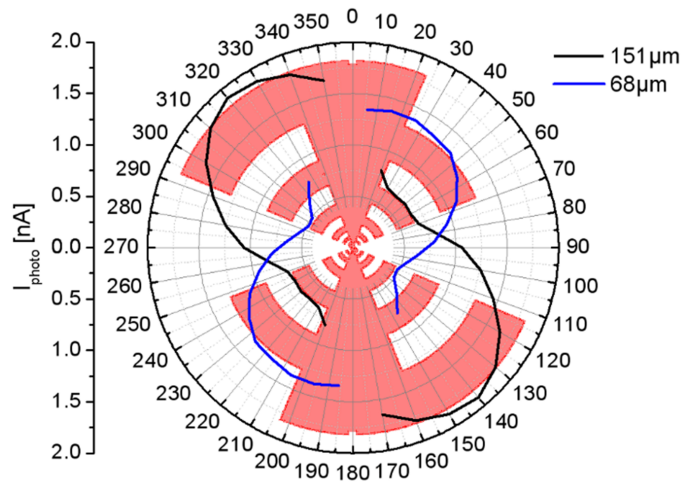
Figure 5.10.: Polarization dependent photocurrent for two different wavelengths, in the background, the orientation of the antenna is depicted. Figure taken from [97].

5.8. Improvements of the detector

To circumvent the limitations caused by the substrate, new devices have been produced on semi insulating SiC. This should be an ideal substrate as it has a very large band gap of about $3\,$eV. While it is in principle as easy to deposit a graphene flake to this substrate, the big challenge is to find it on the SiC. While a single layer of graphene is visible with the bare eye when it is placed on SiO_2 on Si, it is practically invisible on SiC. Hence, the standard procedure of producing a graphene flake by exfoliation is not suitable in this case. To circumvent these problems, in a first step a metal pattern was deposited to the SiC. To get a large amount of single

layer graphene to the substrate, CVD grown graphene on copper was transferred to the SiC. As mentioned before, the graphene is nearly invisible on this substrate, therefore a part of the surface was imaged by Raman mapping. With this technique it was possible to find large graphene flakes within reasonable time (see Fig. 5.11). With these Raman mapped images in combination with optical images of the metal pattern on the SiC, an antenna could be attached to the graphene flake. These new type of detector showed the same performance at longer wavelength (above $30\,\mu$m) compared to the first detector version on highly-resistive Si. With these new devices FEL pulses have been observed down to a wavelength of $9\,\mu$m, even directly in the Reststrahlenband of SiC. Notably, this limit of $9\,\mu$m is not the limit of the detector, but the limit of the measurements performed up to now.
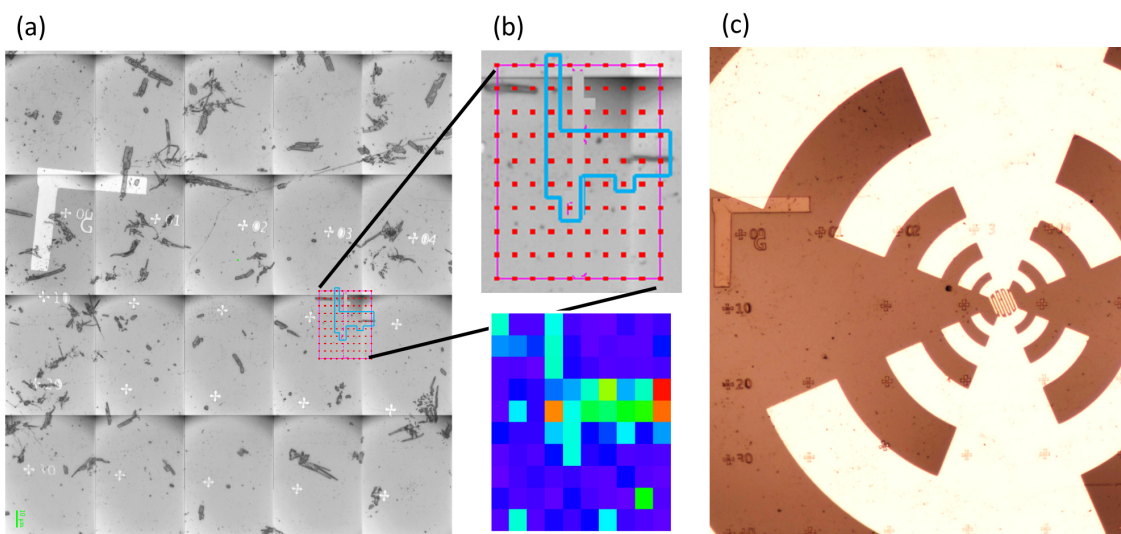
Figure 5.11.: (a) Optical image of the SiC substrate with CVD graphene on top. (b) Enlarged detail of (a) where the pixels for the Raman mapping are marked with red dots, the blue line indicates the border of a graphene flake, below is the Raman map of the $2D$-peak. (c) Optical image of the antenna with the contacts at the position of the graphene flake.

Besides the problems with the substrate, the electrical connection of the detector was strongly improved. While in the first devices a coaxial cable was directly glued to the contact pads, in a later version the chip with the detector on top is placed inside a copper block. A SMA connector is directly fixed on the copper block and the signal wire of this connector is directly contacted to one of the antenna arms, while the second arm is contacted to the copper block itself. A picture of a complete device can be seen in Fig. 5.12 (a). With this direct connection, the secondary pulses

in the detector signal is completely suppressed. In Fig. 5.12 (b), a signal measured with a new device at a wavelength of 148 μm is depicted.

(a)   (b)
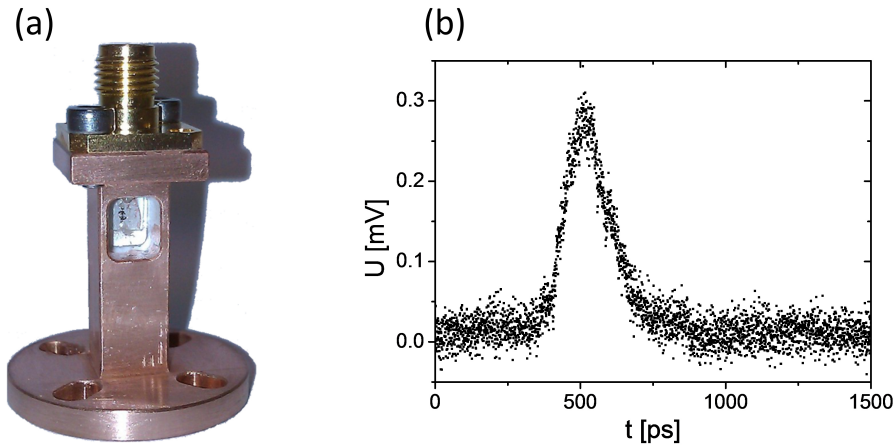
Figure 5.12.: (a) Photograph of a complete device with SMA connector. (b) FEL pulse measured at a wavelength of 148 μm with a device of the new design.

5.9. Discussion and future prospects

There is already a variety of different ultrafast detectors working in the THz range at room temperature. For example photon drag detectors [99] have an increased sensitivity compared to the detector presented in this work. They reach up to 80 nA/W, while the rise time of 1 ns is comparably low. This slow rise time leads to a signal of the extremely fast FEL pulses which is significantly smaller compared to the graphene-based devices. Detectors which are comparably fast are the superlattice detector (SLD) [100] and field-effect transistors (FET) [101]. Both types exhibit a rise time below 50 ps (SLD 20 ps; FET 30 ps) and a higher responsivity (SLD 50μA/W; FET 30 nA/W) at low frequencies (below 6 THz). For higher frequencies the responsivity decreases strongly. Among these detectors, the graphene-based THz detector presented in this work, is one of the fastest detectors in the mid and far infrared range operating at room temperature. Compared to the alternative devices, the graphene based detector is very robust, easy to produce and easy to handle.

The next, very important step has to be the experimental verification of the lower wavelength limit of the device, as it should work down to the ultraviolet range in principle. Besides its extremely broadband response, the small signals which can

be obtained remain as an important point for further improvements. One way to improve the signal-to-noise ratio could be the cooled operation at liquid nitrogen temperature. Furthermore, the possibility to gate the graphene flake could be helpful in two different ways. On the one side it would help to understand the underlying absorption effects at different wavelength, which could help to further improve the detector. On the other side, the Fermi energy in the graphene flake could be shifted to zero, which would strongly increase the resistivity of the device, and therefore enhance the signal-to-noise ratio.

6. Conclusion and outlook

A number of different pump-probe experiments are presented in this thesis combined with the results of the detector development. In this conclusion I would like to point out the my personal highlight of each chapter and give a short outlook on future measurements.

Three different investigations on the relaxation dynamics of graphene without magnetic fields were presented in Chapter 3. Besides the two-color pump-probe measurements and the experiments at large pump power and small photon energies, the anisotropic carrier excitation in graphene was investigated. We could show that the isotropic bandstructure of graphene, in combination with linearly polarized radiation, leads to a strong anisotropy of the carrier distribution in momentum space. The initial relaxation takes place via carrier-carrier scattering within the first tens of femtoseconds. Subsequent carrier-phonon scattering can change the momentum of the excited carrier which leads to an isotropic carrier distribution after about 150 fs. In the case of near-infrared excitation, the carrier-phonon scattering is very efficient since the excitation energy is far above the energies of the optical phonons. A next step could be the verification of the theoretical findings via investigations of the anisotropic carrier excitation at small photon energies. The anisotropic carrier distribution should be preserved for a longer time as the carrier-phonon scattering is less efficient in this scenario.

Chapter 4 was devoted to the carrier relaxation dynamics of graphene in magnetic fields and reflects the main part of the research in this thesis. A small photon energy of 14 meV allowed the investigation of interband Landau-level transitions in highly doped graphene layers. More importantly, at a higher photon energy of 75 meV detailed investigation of the dynamics within the three lowest Landau levels LL_{-1}, LL_0 and LL_1 were possible. The different combinations of circularly polarized pump and probe radiation led to a complex set of results. A simple three-level rate-equation model could reveal the underlying Auger-like processes, which were verified through microscopic modeling by our theory partners at the Technical University of

Berlin. A large variety of experiments is possible for future investigations of Landau-quantized graphene. E.g. two-color pump-probe experiments could shed more light on Auger-like processes between the three equidistant Landau levels LL_0, LL_1 and LL_4. Maybe the most prominent task for the dynamics under Landau quantization is the search for THz gain to pave the way for Landau-level laser. When the transition $LL_{-1} \to LL_2$ is pumped, THz gain might appear for the transition $LL_2 \to LL_1$.

A graphene-based THz detector was presented in Chapter 5. The device consists of a graphene flake that is connected to a logarithmic periodic antenna and shows response in a wavelength range from $9\,\mu$m to $500\,\mu$m. With a rise time of about $50\,$ps, this device is very interesting for ultrafast detection of free-electron laser pulses. This is very important e.g. for two-color pump-probe experiments, were the temporal overlap of a free-electron laser and a table-top laser has to be aligned. While the high-speed performance of this detector is outstanding, two features remain improvable. On the one side the responsivity of the device of about $5\,$nA/W is rather poor, on the other side it would be interesting to extend the wavelength range to the visible. In a next step the possibility to control the Fermi energy of the graphene flake with a top gate could be included. This would help to understand the underlying effects leading to the photocurrent.

A. Source code of rate-equation model

In the following part, the source code of the rate-equation model is plotted. The parameters for the results depicted in Fig. 4.18 are shown in Table A.1.

Table A.1.: Parameters for the calculation of the pump-probe signals depicted in figure 4.18.

n	N_1	N_0	N_{-1}	σ	$Gpeak$	τ_{p1}	τ_{Auger}
1000	0	750	1000	$1.7\,\mathrm{ps}$	$500\,\mathrm{ps}^{-1}$	$15\,\mathrm{ps}$	$1.5\,\mathrm{ps}$

```
void MainWindow::on_pushButton_clicked()
{
    //allocation of RAM
    if (pTime) delete[] pTime;
    if (pPulse1) delete[] pPulse1;
    if (pPulse2) delete[] pPulse2;
    if (pN_1) delete[] pN_1;
    if (pN0) delete[] pN0;
    if (pN1) delete[] pN1;
    if (pProLi) delete[] pProLi;
    if (pProRe) delete[] pProRe;
    if (ui->schritte->value()==0)return;
    int iSchritte = ui->schritte->value();
    try {
        pTime = new double[iSchritte];
        pPulse1 = new double[iSchritte];
        pPulse2 = new double[iSchritte];
        pProLi = new double[iSchritte];
```

```
        pProRe = new double[iSchritte];
        pN_1 = new double[iSchritte];
        pN0 = new double[iSchritte];
        pN1 = new double[iSchritte];
    }
    catch(...){
        return;
    }


    //add some variables
    double dAmplitude = ui->Amplitude->value();
    double dAmplitude2 = ui->Amplitude_2->value() * dAmplitude / 100.0;
    double dAmplitude3 = ui->Amplitude_3->value() * dAmplitude / 100.0;
    double dAmplitude4 = ui->Amplitude_4->value() * dAmplitude / 100.0;
    double firstPulse;
    double secondPulse;
    double thirdPulse;
    double fourthPulse;
    double dSchrittweite = (ui->stop->value() - ui->start->value())
/ (double)iSchritte;
    double dStart = ui->start->value();
    double dSigma = ui->sigma->value();
    double dt0 = ui->t0->value();
    double dt2 = ui->t0_2->value() + dt0;
    double dt3 = ui->t0_3->value() + dt0;
    double dt4 = ui->t0_4->value() + dt0;

    //set boarders for plot of pulses
    ui->Pulslinks->setLimits(ui->start->value(),ui->stop->value(),
-1,dAmplitude+1);
    ui->Pulsrechts->setLimits(ui->start->value(),ui->stop->value(),
-1,dAmplitude+1);
    pulslinks->clearPoints();
    pulsrechts->clearPoints();

    //start of the calculations
    //calculation of the pump pulse
```

```
    for ( int i = 0 ; i < iSchritte ; i++ ){
        pTime[i] = dStart + i * dSchrittweite;
        if (ui->linkszirkular->isChecked()){
            firstPulse = (dAmplitude*exp(-0.5*((pTime[i]-dt0)/dSigma)
*((pTime[i]-dt0)/dSigma)));
            //option to include multiple pulses
            secondPulse = (dAmplitude2*exp(-0.5*((pTime[i]-dt2)/dSigma)
*((pTime[i]-dt2)/dSigma)));
            thirdPulse = (dAmplitude3*exp(-0.5*((pTime[i]-dt3)/dSigma)
*((pTime[i]-dt3)/dSigma)));
            fourthPulse = (dAmplitude4*exp(-0.5*((pTime[i]-dt4)/dSigma)
*((pTime[i]-dt4)/dSigma)));
            pPulse1[i] = firstPulse + secondPulse + thirdPulse + fourthPulse;
            pPulse1[i] = ui->linksProzent->value() * pPulse1[i]/100.0;
        } else {
            pPulse1[i] = 0;
        }
        if ( ui->rechtszirkular->isChecked()){
            firstPulse = (dAmplitude*exp(-0.5*((pTime[i]-dt0)/dSigma)
*((pTime[i]-dt0)/dSigma)));
            //option to include multiple pulses
            secondPulse = (dAmplitude2*exp(-0.5*((pTime[i]-dt2)/dSigma)
*((pTime[i]-dt2)/dSigma)));
            thirdPulse = (dAmplitude3*exp(-0.5*((pTime[i]-dt3)/dSigma)
*((pTime[i]-dt3)/dSigma)));
            fourthPulse = (dAmplitude4*exp(-0.5*((pTime[i]-dt4)/dSigma)
*((pTime[i]-dt4)/dSigma)));
            pPulse2[i] = firstPulse + secondPulse + thirdPulse + fourthPulse;
            pPulse2[i] = ui->rechtsProzent->value() * pPulse2[i]/100.0;
        } else {
            pPulse2[i] = 0;
        }
        pulslinks->addPoint(pTime[i],pPulse1[i]);
        pulsrechts->addPoint(pTime[i],pPulse2[i]);
    }
    ui->Pulslinks->update();
    ui->Pulsrechts->update();
```

```
    //get initial occupation from GUI
    pN_1[0] = (double)ui->N0LL_1->value();
    pN0[0] = (double)ui->N0LL0->value();
    pN1[0] = (double)ui->N0LL1->value();

    //some more variables
    double maxN1 = pN1[0];double maxN_1 = pN_1[0]; double maxN0 = pN0[0];
    double minN1 = pN1[0];double minN_1 = pN_1[0]; double minN0 = pN0[0];
    double minProbelinks = 0;double maxProbelinks = 0;
    double minProberechts = 0;double maxProberechts = 0;
    double anregung1, anregung2;
    double relaxation1, relaxation2, relaxation1_1;
    double diff, frei,frei_1,frei1,frei0;
    double auger1,auger2;
    besLL1->clearPoints();
    besLL0->clearPoints();
    besLL_1->clearPoints();
    probelinks->clearPoints();
    proberechts->clearPoints();

    //calculation of the occupation
    for ( int i = 1 ; i < iSchritte ; i++ ){

        //calculation of non-occuppied states in each LL
        frei1 = ((double) ui->LL1->value()) - pN1[i-1];
        frei_1 = ((double) ui->LL_1->value()) - pN_1[i-1];
        frei0 = ((double) ui->LL0->value()) - pN0[i-1];

        //excitation via pump pulses
        anregung1 = pPulse1[i-1] * (pN0[i-1]/(double)ui->LL0->value()
* frei1/(double)ui->LL1->value()) * dSchrittweite*0.02;
        anregung2 = pPulse2[i-1] * (pN_1[i-1]/(double)ui->LL_1->value()
* frei0/(double)ui->LL0->value()) * dSchrittweite*0.02;

        //relaxation processes
```

```
        //relaxation LL1->LL0
        relaxation1 = 1000.0*( dSchrittweite/(double)ui->tRelax->value() )
*( pN1[i-1]/(double)ui->LL1->value())*(frei0)/(double)ui->LL0->value();
        //relaxation LL0->LL-1
        relaxation2 = 1000.0*( dSchrittweite/(double)ui->tRelax->value() )
*(pN0[i-1]/(double)ui->LL0->value())*(frei_1)/(double)ui->LL_1->value();
        //relaxation LL1->LL-1
        relaxation1_1 = 1000.0*( dSchrittweite/(double)ui->spinBox->value()
*(pN1[i-1]/(double)ui->LL1->value())*(frei_1)/(double)ui->LL_1->value());


        //Auger processes

//auger1 describes outward Auger process,
//auger2 the inward
        auger1 = (dSchrittweite/(double)ui->tAuger->value())*
(pN0[i-1]/(double)ui->LL0->value()*frei_1/(double)ui->LL_1->value())*10000.0;
        auger2 = (dSchrittweite/(double)ui->tAuger_2->value())*
(pN1[i-1]/(double)ui->LL1->value()*frei0/(double)ui->LL0->value())*10000.0;


        //deactivation possibility of different processes
        if ( !ui->checkBox->isChecked() )auger1 = 0;
        if ( !ui->checkBox_2->isChecked() )auger2 = 0;
        if ( !ui->checkBox_3->isChecked() ){
            relaxation1 = 0;
            relaxation2 = 0;
        }
        if ( !ui->checkBoxtauii->isChecked() )relaxation1_1 = 0;


        //adding up of the different contributions
        pN1[i] = pN1[i-1] + anregung1 - relaxation1 + auger1
- auger2 - relaxation1_1;
        pN0[i] = pN0[i-1] - anregung1 + anregung2 + relaxation1 - relaxation2
- (auger1 * 2.0) + (auger2 * 2.0);
        pN_1[i] = pN_1[i-1] - anregung2 + relaxation2 + auger1
- auger2 + relaxation1_1;


        //find maxima and minima for scaling of widget
```

```cpp
        if ( pN1[i] > maxN1 ) maxN1 = pN1[i];
        if ( pN1[i] < minN1 ) minN1 = pN1[i];
        if ( pN0[i] > maxN0 ) maxN0 = pN0[i];
        if ( pN0[i] < minN0 ) minN0 = pN0[i];
        if ( pN_1[i] > maxN_1 ) maxN_1 = pN_1[i];
        if ( pN_1[i] < minN_1 ) minN_1 = pN_1[i];
    }
    ui->BesetzungLL1->setLimits(ui->start->value(),
ui->stop->value(),minN1-10,maxN1+10);
    ui->BesetzungLL0->setLimits(ui->start->value(),
ui->stop->value(),minN0-10,maxN0+10);
    ui->BesetzungLL_1->setLimits(ui->start->value(),
ui->stop->value(),minN_1-10,maxN_1+10);
    for ( int i = 0 ; i < iSchritte ; i++ ){
        besLL1->addPoint(pTime[i],pN1[i]);
        besLL0->addPoint(pTime[i],pN0[i]);
        besLL_1->addPoint(pTime[i],pN_1[i]);
    }
    ui->BesetzungLL1->update();
    ui->BesetzungLL0->update();
    ui->BesetzungLL_1->update();


    //calculation of the pump-probe signals
    for ( int i = 0 ; i < iSchritte ; i++ ){
        pProLi[i] = (pN0[i] - ( (double)ui->LL0->value()
/ (double)ui->LL1->value() ) * pN1[i]);
        pProRe[i] = (pN_1[i] - ( (double)ui->LL_1->value()
/ (double)ui->LL0->value() ) * pN0[i]);
        if ( i ){
            pProLi[i] = -(pProLi[i] - pProLi[0])/pProLi[0];
            pProRe[i] = -(pProRe[i] - pProRe[0])/pProRe[0];
        }
        if ( i == 0 ){
            probelinks->addPoint(pTime[0],0);
            proberechts->addPoint(pTime[0],0);
            maxProbelinks = 0;
            minProbelinks = 0;
```

```
            maxProberechts = 0;
            minProberechts = 0;
        } else {
            probelinks->addPoint(pTime[i],pProLi[i]*100.0);
            proberechts->addPoint(pTime[i],pProRe[i]*100.0);
            if (maxProbelinks<pProLi[i]) maxProbelinks = pProLi[i];
            if (minProbelinks>pProLi[i]) minProbelinks = pProLi[i];
            if (maxProberechts<pProRe[i]) maxProberechts = pProRe[i];
            if (minProberechts>pProRe[i]) minProberechts = pProRe[i];
        }
    }
    pProLi[0] = 0;
    pProRe[0] = 0;
    ui->ProLi->setLimits(ui->start->value(),ui->stop->value(),
(minProbelinks*100.0)-1.0,(maxProbelinks*100.0)+1.0);
    ui->ProRe->setLimits(ui->start->value(),ui->stop->value(),
(minProberechts*100.0)-1.0,(maxProberechts*100.0)+1.0);
    ui->ProLi->update();
    ui->ProRe->update();
}
```

Bibliography

[1] K. S. Novoselov, A. K. Geim, S. V. Morozov, D. Jiang, Y. Zhang, S. V. Dubonos, I. V. Grigorieva, and A. A. Firsov. Electric field effect in atomically thin carbon films. *Science*, 306:666–669, 2004.

[2] K. S. Novoselov, A. K. Geim, S. V. Morozov, D. Jiang, M. I. Katsnelson, I. V. Grigorieva, S. V. Dubonos, and A. A. Firsov. Two-dimensional gas of massless Dirac fermions in graphene. *Nature*, 438:197–200, 2005.

[3] Y Zhang, Y-W Tan, H. L. Stormer, and P. Kim. Experimental observation of the quantum hall effect and Berry's phase in graphene. *Nature*, 438:201–204, 2005.

[4] I. W. Frank, D. M. Tanenbaum, A. M. van der Zande, and P. L. McEuen. Mechanical properties of suspended graphene sheets. *Journal of Vacuum Science & Technology B*, 25:2558–2561, 2007.

[5] C. Lee, X. Wei, J. W. Kysar, and J. Hone. Measurement of the elastic properties and intrinsic strength of monolayer graphene. *Science*, 321:385–388, 2008.

[6] P. R. Wallace. The band theory of graphite. *Physical Review*, 71:622–634, 1947.

[7] M. L. Sadowski, G. Martinez, M. Potemski, C. Berger, and W. A. de Heer. Landau level spectroscopy of ultrathin graphite layers. *Physical Review Letters*, 97:266405, 2006.

[8] E. L. Wolf. *Graphene*. Oxford University Press, Oxford, United Kingdom, 2014.

[9] K.I. Bolotin, K. J. Sikes, Z. Jiang, M. Klima, G. Fudenberg, J. Hone, P. Kim, and H. L. Stormer. Ultrahigh electron mobility in suspended graphene. *Solid State Communications*, 146:351 – 355, 2008.

[10] Sheng S. Li and W.Robert Thurder. The dopant density and temperature dependence of electron mobility and resistivity in n-type silicon. *Solid-State Electronics*, 20:609 – 616, 1977.

[11] J.-H. Chen, C. Jang, S. Xiao, M. Ishigami, and M. S. Fuhrer. Intrinsic and extrinsic performance limits of graphene devices on SiO2. *Nature Nanotechnology*, 3:206–209, 2008.

[12] Yanqing Wu, Yu ming Lin, Ageeth A. Bol, Keith A. Jenkins, Fengnian Xia, Damon B. Farmer, YuZhu, and Phaedon Avouris. High-frequency, scaled graphene transistors on diamond-like carbon. *Nature*, 472:74–78, 2011.

[13] W. Zhu, V. Perebeinos, M. Freitag, and P. Avouris. Carrier scattering, mobilities, and electrostatic potential in monolayer, bilayer, and trilayer graphene. *Physical Review B*, 80:235402, 2009.

[14] R. R. Nair, P. Blake, A. N. Grigorenko, K. S. Novoselov, T. J. Booth, T. Stauber, N. M. R. Peres, and A. K. Geim. Fine structure constant defines visual transparency of graphene. *Science*, 320:1308, 2008.

[15] J. M. Dawlaty, S. Shivaraman, J. Strait, P. George, M. Chandrashekhar, F. Rana, M. G. Spencer, D. Veksler, and Y. Chen. Measurement of the optical absorption spectra of epitaxial graphene from terahertz to visible. *Applied Physics Letters*, 93:131905, 2008.

[16] S. Winnerl, F. Goettfert, M. Mittendorff, H. Schneider, M. Helm, T. Winzer, E. Malic, A. Knorr, M. Orlita, M. Potemski, M. Sprinkle, C. Berger, and W. A. de Heer. Time-resolved spectroscopy on epitaxial graphene in the infrared spectral range: relaxation dynamics and saturation behavior. *Journal of Physics: Condensed Matter*, 25:054202, 2013.

[17] S. Winnerl, M. Orlita, P. Plochocka, P. Kossacki, M. Potemski, T. Winzer, E. Malic, A. Knorr, M. Sprinkle, C. Berger, W. A. de Heer, H. Schneider, and M. Helm. Carrier relaxation in epitaxial graphene photoexcited near the Dirac point. *Physical Review Letters*, 107:237401, 2011.

[18] A. B. Kuzmenko, E. van Heumen, F. Carbone, and D. van der Marel. Universal optical conductance of graphite. *Physical Review Letters*, 100:117401, 2008.

116

[19] T. Mueller, F. Xia, and P. Avouris. Graphene photodetectors for high-speed optical communications. *Nature Photonics*, 4:297–301, 2010.

[20] L. Vicarelli, M. W. Vitiello, D. Coquillat, A. Lombardo, A. C. Ferrari, W. Knap, M. Polini, V. Pellegrini, and A. Tredicucci. Graphene field-effect transistors as room-temperature terahertz detectors. *Nat. Materials*, 11:865–871, 2012.

[21] Z. Sun, T. Hasan, and A.C. Ferrari. Ultrafast lasers mode-locked by nanotubes and graphene. *Physica E: Low-dimensional Systems and Nanostructures*, 44: 1082 – 1091, 2012.

[22] M. Jablan, H. Buljan, and M. Soljačić. Plasmonics in graphene at infrared frequencies. *Physical Review B*, 80:245435, 2009.

[23] L. Ju, B. Geng, J. Horng, C. Girit, M. Martin, Z. Hao, H. A. Bechtel, X. Liang, A. Zettl, Y. R. Shen, and F. Wang. Graphene plasmonics for tunable terahertz metamaterials. *Nature Nanotechnology*, 6:630–634, 2011.

[24] X. Wang, L. Zhi, and K. Mullen. Transparent, conductive graphene electrodes for dye-sensitized solar cells. *Nano Letters*, 8:323–327, 2008.

[25] M. O. Goerbig. Electronic properties of graphene in a strong magnetic field. *Review of Modern Physics*, 83:1193–1243, 2011.

[26] A. C. Ferrari, J. C. Meyer, V. Scardaci, C. Casiraghi, M. Lazzeri, F. Mauri, S. Piscanec, D. Jiang, K. S. Novoselov, S. Roth, and A. K. Geim. Raman spectrum of graphene and graphene layers. *Physical Review Letters*, 97:187401, 2006.

[27] A. C. Ferrari. Raman spectroscopy of graphene and graphite: Disorder, electronphonon coupling, doping and nonadiabatic effects. *Solid State Communications*, 143:47–57, 2007.

[28] A. Das, S. Pisana, B. Chakraborty, S. Piscanec, S. K. Saha, U. V. Waghmare, K. S. Novoselov, H. R. Krishnamurthy, A. K. Geim, A. C. Ferrari, and A. K. Sood. Monitoring dopants by raman scattering in an electrochemically topgated graphene transistor. *Nature Nanotechnology*, 3:210–215, 2008.

[29] T. M. G. Mohiuddin, A. Lombardo, R. R. Nair, A. Bonetti, G. Savini, R. Jalil, N. Bonini, D. M. Basko, C. Galiotis, N. Marzari, K. S. Novoselov, A. K. Geim, and A. C. Ferrari. Uniaxial strain in graphene by Raman spectroscopy: G-peak splitting, Grüneisen parameters, and sample orientation. *Physical Review B*, 79:205433, 2009.

[30] M. Huang, H. Yan, T. F. Heinz, and J. Hone. Probing strain-induced electronic structure change in graphene by Raman spectroscopy. *Nano Letters*, 10:4074–4079, 2010.

[31] Y Hernandez, V. Nicolosi, M. Lotya, F. M. Blighe, Z. Sun, S. De, I. T. McGovern, B. Holland, M. Byrne, Y. K. Gun'Ko, J. J. Boland, P. Niraj, G. Duesberg, S. Krishnamurthy, R. Goodhue, V. Hutchison, J. Scardaci, Ferrari A. C., and J. N. Coleman. High-yield production of graphene by liquid-phase exfoliation of graphite. *Nature Nanotechnology*, 3:563–568, 2008.

[32] J. I. Paredes, S. Villar-Rodil, M. J. Fernandez-Merino, L. Guardia, A. Martinez-Alonso, and J. M. D. Tascon. Environmentally friendly approaches toward the mass production of processable graphene from graphite oxide. *Journal of Materials Chemistry*, 21:298–306, 2011.

[33] K. Kim, S. I. Ahn, and K. C. Choi. Simultaneous synthesis and patterning of graphene electrodes by reactive inkjet printing. *Carbon*, 66:172–177, 2014.

[34] C. Soldano, A. Mahmood, and E. Dujardin. Production, properties and potential of graphene. *Carbon*, 48:2127–2150, 2010.

[35] I. Jung, M. Pelton, R. Piner, D. A. Dikin, S. Stankovich, S. Watcharotone, M. Hausner, and R. S. Ruoff. Simple approach for high-contrast optical imaging and characterization of graphene-based sheets. *Nano Letters*, 7:3569–3575, 2007.

[36] C. Berger, Z. Song, T. Li, X. Li, A. Y. Ogbazghi, R. Feng, Z. Dai, A. N. Marchenkov, E. H. Conrad, P. N. First, and W. A. de Heer. Ultrathin epitaxial graphite: 2D electron gas properties and a route toward graphene-based nanoelectronics. *The Journal of Physical Chemistry B*, 108:19912–19916, 2004.

[37] K. Emtsev, A. Bostwick, K. Horn, J. Jobst, G. L. Kellogg, L. Ley, J.L. McChesney, T. Ohta, S. A. Reshanov, J. Rohrl, E. Rotenberg, A. K. Schmid,

D. Waldmann, H. B. Weber, and T. Seyller. Towards wafer-size graphene layers by atmospheric pressure graphitization of silicon carbide. *Nature Materials*, 8:203–207, 2009.

[38] T. Ohta, F. E. Gabaly, A. Bostwick, J. L. McChesney, K. V. Emtsev, A. K. Schmid, T. Seyller, K. Horn, and E. Rotenberg. Morphology of graphene thin film growth on SiC(0001). *New Journal of Physics*, 10:023034, 2008.

[39] C. Riedl, C. Coletti, T. Iwasaki, A. A. Zakharov, and U. Starke. Quasi-free-standing epitaxial graphene on SiC obtained by hydrogen intercalation. *Physical Review Letters*, 103:246804, 2009.

[40] M. Ruan, Y. Hu, Z. Guo, R. Dong, J. Palmer, J. Hankinson, C. Berger, and W. A. de Heer. Epitaxial graphene on silicon carbide: Introduction to structured graphene. *MRS Bulletin*, 37:1138, 2012.

[41] J. Hass, W. A. de Heer, and E. H. Conrad. The growth and morphology of epitaxial multilayer graphene. *Journal of Physics: Condensed Matter*, 20: 323202, 2008.

[42] M. Sprinkle, J. Hicks, A. Tejeda, A. Taleb-Ibrahimi, P. Le Fvre, F. Bertran, H. Tinkey, M. C. Clark, P. Soukiassian, D. Martinotti, J. Hass, and E. H. Conrad. Multilayer epitaxial graphene grown on the $SiC\,(\,000\bar{1}\,)$ surface; structure and electronic properties. *Journal of Physics D: Applied Physics*, 43:374006, 2010.

[43] D. Sun, C. Divin, C. Berger, W. A. de Heer, P. N. First, and T. B. Norris. Spectroscopic measurement of interlayer screening in multilayer epitaxial graphene. *Physical Review Letters*, 104:136802, 2010.

[44] T. A. Land, T. Michely, R. J. Behm, J. C. Hemminger, and G. Comsa. STM investigation of single layer graphite structures produced on $Pt(111)$ by hydrocarbon decomposition. *Surface Science*, 264:261–270, 1992.

[45] P. W. Sutter, J.-I. Flege, and E. A. Sutter. Eptiaxial graphene on ruthenium. *Nature Materials*, 7:406–411, 2008.

[46] Peter Sutter, Jerzy T. Sadowski, and Eli Sutter. Graphene on Pt(111): Growth and substrate interaction. *Physical Review B*, 80:245411, 2009.

[47] P. Zeller, S. Dänhardt, S. Gsell, M. Schreck, and J. Wintterlin. Scalable synthesis of graphene on single crystal Ir(111) films. *Surface Science*, 606: 1475–1480, 2012.

[48] X. Li, W. Cai, L. Colombo, and R. S. Ruoff. Evolution of graphene growth on Ni and Cu by carbon isotope labeling. *Nano Letters*, 9:4268–4272, 2009.

[49] S. Bae, H. Kim, Y. Lee, X. Xu, J.-S. Park, Y. Zheng, J. Balakrishnan, T. Lei, H. R. Kim, Y. I. Song, Y.-J. Kim, K. S. Kim, B. zyilmaz, J.-H. Ahn, B. H. Hong, and S. Iijima. Roll-to-roll production of 30-inch graphene films for transparent electrodes. *Nature Nanotechnology*, 5:574–578, 2010.

[50] M. Orlita, C. Faugeras, P. Plochocka, P. Neugebauer, G. Martinez, D. K. Maude, A.-L. Barra, M. Sprinkle, C. Berger, W. A. de Heer, and M. Potemski. Approaching the Dirac point in high-mobility multilayer epitaxial graphene. *Physical Review Letters*, 101:267601, 2008.

[51] F. Göttfert. Relaxationsdynamik der Ladungstrger in Graphen. Diplomarbeit, Technische Universität Dresden, 2011.

[52] M. Beck, I. Rousseau, M. Klammer, P. Leiderer, M. Mittendorff, S. Winnerl, M. Helm, G. N. Gol'tsman, and J. Demsar. Transient increase of the energy gap of superconducting NbN thin films excited by resonant narrow-band terahertz pulses. *Physical Review Letters*, 110:267003, 2013.

[53] N. Deßmann, S. G. Pavlov, V. N. Shastin, R. Kh. Zhukavin, V. V. Tsyplenkov, S. Winnerl, M. Mittendorff, N. V. Abrosimov, H. Riemann, and H.-W. Hübers. Time-resolved electronic capture in n-type germanium doped with antimony. *Physical Review B*, 89:035205, 2014.

[54] S. G. Pavlov, N. Deßmann, V. N. Shastin, R. Kh. Zhukavin, B. Redlich, A. F. G. van der Meer, M. Mittendorff, S. Winnerl, N. V. Abrosimov, H. Riemann, and H.-W. Hübers. Terahertz stimulated emission from silicon doped by hydrogenlike acceptors. *Physical Review X*, 4:021009, 2014.

[55] D. J. Hilton. *Optical techniques for solid-state materials characterization,* edited by R. P. Prasankumar and J. T. Antoinette, chapter Ultrafast pump-probe spectroscopy, pages 329–370. CRC Press, Boca Raton, United States of America, 2012.

120

[56] P. Michel, F. Gabriel, E. Grosse, P. Evtushenko, T. Dekorsy, M. Krenz, M. Helm, U. Lehnert, W. Seidel, R. Wünsch, D. Wohlfarth, and A. Wolf. First lasing of the ELBE mid-IR FEL. *Proceedings of the 2004 FEL Conference*, pages 8–13, 2004.

[57] J. M. Dawlaty, S. Shivaraman, M. Chandrashekhar, F. Rana, and M. G. Spencer. Measurement of ultrafast carrier dynamics in epitaxial graphene. *Applied Physics Letters*, 92:042116, 2008.

[58] H. Wang, J. H. Strait, P. A. George, S. Shivaraman, V. B. Shields, M. Chandrashekhar, J. Hwang, F. Rana, M. G. Spencer, C. S. Ruiz-Vargas, and J. Park. Ultrafast relaxation dynamics of hot optical phonons in graphene. *Applied Physics Letters*, 96:081917, 2010.

[59] M. Breusing, C. Ropers, and T. Elsaesser. Ultrafast carrier dynamics in graphite. *Physical Review Letters*, 102:086809, 2009.

[60] D. Sun, Z.-K. Wu, C. Divin, X. Li, C. Berger, W. A. de Heer, P. N. First, and T. B. Norris. Ultrafast relaxation of excited Dirac fermions in epitaxial graphene using optical differential transmission spectroscopy. *Physical Review Letters*, 101:157402, 2008.

[61] H. Choi, F. Borondics, D. A. Siegel, S. Y. Zhou, M. C. Martin, A. Lanzara, and R. A. Kaindl. Broadband electromagnetic response and ultrafast dynamics of few-layer epitaxial graphene. *Applied Physics Letters*, 94:172102, 2009.

[62] P. Bowlan, E. Martinez-Moreno, K. Reimann, M. Woerner, and T. Elsaesser. Terahertz radiative coupling and damping in multilayer graphene. *New Journal of Physics*, 16:013027, 2014.

[63] T. Winzer, E. Malic, and A. Knorr. Microscopic mechanism for transient population inversion and optical gain in graphene. *Physical Review B*, 87: 165413, 2013.

[64] S. Boubanga-Tombet, S. Chan, T. Watanabe, A. Satou, V. Ryzhii, and T. Otsuji. Ultrafast carrier dynamics and terahertz emission in optically pumped graphene at room temperature. *Physical Review B*, 85:035443, 2012.

[65] T. Watanabe, T. Fukushima, Y. Yabe, S. A. B. Tombet, A. Satou, A. A. Dubinov, Aleshkin V. Y., V. Mitin, V. Ryzhii, and T. Otsuji. The gain enhancement effect of surface plasmon polaritons on terahertz stimulated emission in optically pumped monolayer graphene. *New Journal of Physics*, 15:075003, 2013.

[66] J. C. Johannsen, S. Ulstrup, F. Cilento, A. Crepaldi, M. Zacchigna, C. Cacho, I. C. E. Turcu, E. Springate, F. Fromm, C. Raidel, T. Seyller, F. Parmigiani, M. Grioni, and P. Hofmann. Direct view of hot carrier dynamics in graphene. *Physical Review Letters*, 111:027403, 2013.

[67] I. Gierz, J. C. Petersen, M. Mitrano, C. Cacho, I. C. E. Turcu, E. Springate, A. Sthr, A. Khler, U. Starke, and A. Cavalleri. Snapshots of non-equilibrium dirac carrier distributions in graphene. *Nature Materials*, 12:1119–1124, 2013.

[68] A. Grüneis, R. Saito, Ge. G. Samsonidze, T. Kimura, M. A. Pimenta, A. Jorio, A. G. Souza Filho, G. Dresselhaus, and M. S. Dresselhaus. Inhomogeneous optical absorption around the K point in graphite and carbon nanotubes. *Physical Review B*, 67:165402, 2003.

[69] M. Mittendorff, T. Winzer, E. Malic, A. Knorr, C. Berger, W. A. de Heer, H. Schneider, M. Helm, and S. Winnerl. Anisotropy of excitation and relaxation of photogenerated charge carriers in graphene. *Nano Letters*, 14: 1504–1507, 2014.

[70] E. Malic, T. Winzer, and A. Knorr. Efficient orientational carrier relaxation in optically excited graphene. *Applied Physics Letters*, 101:213110, 2012.

[71] E. Malic, T. Winzer, E. Bobkin, and A. Knorr. Microscopic theory of absorption and ultrafast many-particle kinetics in graphene. *Physical Review B*, 84: 205406, 2011.

[72] K. L. Sala, G. A. Kenney-Wallace, and G. E. Hall. CW autocorrelation measurements of picosecond laser pulses. *IEEE Journal of Quantum Electronics*, 16:990–996, 1980.

[73] E. Garmire. Resonant optical nonlinearities in semiconductors. *Selected Topics in Quantum Electronics, IEEE Journal of*, 6:1094–1110, 2000.

[74] T. Winzer, A. Knorr, M. Mittendorff, S. Winnerl, M.-B. Lien, D. Sun, T. B. Norris, M. Helm, and E. Malic. Absorption saturation in optically excited graphene. *Applied Physics Letters*, 101:221115, 2012.

[75] Z. Sun, T. Hasan, F. Torrisi, D. Popa, G. Privitera, F. Wang, F. Bonaccorso, D. M. Basko, and A. C. Ferrari. Graphene mode-locked ultrafast laser. *ACS Nano*, 4:803–810, 2010.

[76] P. Plochocka, P. Kossacki, A. Golnik, T. Kazimierczuk, C. Berger, W. A. de Heer, and M. Potemski. Slowing hot-carrier relaxation in graphene using a magnetic field. *Physical Review B*, 80:245415, 2009.

[77] N. M. R. Peres and E. V. Castro. Algebraic solution of a graphene layer in transverse electric and perpendicular magnetic fields. *Journal of Physics: Condensed Matter*, 19:406231, 2007.

[78] M. Mittendorff, M. Orlita, M. Potemski, C. Berger, W. A. de Heer, H. Schneider, M. Helm, and S. Winnerl. Intraband carrier dynamics in Landau-quantized multilayer epitaxial graphene. *New Journal of Physics*, 16:123021, 2014.

[79] M. Orlita, I. Crassee, C. Faugeras, A. B. Kuzmenko, F. Fromm, M. Ostler, T. Seyller, G. Martinez, M. Polini, and M. Potemski. Classical to quantum crossover of the cyclotron resonance in graphene: a study of the strength of intraband absorption. *New Journal of Physics*, 14:095008, 2012.

[80] J. C. W. Song, M. Y. Reizer, and L. S. Levitov. Disorder-assisted electron-phonon scattering and cooling pathways in graphene. *Physical Review Letters*, 109:106602, 2012.

[81] A. C. Beck, S. H. Jhang, E. Pallecchi, R. Ferreira, G. Feve, J-M. Berroir, and B. Placais. Supercollisions cooling in undoped graphene. *Nature Physics*, 9: 109–112, 2013.

[82] J. C. Johannsen, S. Ulstrup, F. Cilento, A. Crepaldi, M. Zacchigna, C. Cacho, I. C. E. Turcu, E. Springate, F. Fromm, C. Raidel, T. Seyller, F. Parmigiani, M. Grioni, and P. Hofmann. Direct view of hot carrier dynamics in graphene. *Physical Review Letters*, 111:027403, 2013.

[83] M. W. Graham, S.-F. Shi, Z. Wang, D. C. Ralph, J. Park, and P. L. McEuen. Transient absorption and photocurrent microscopy show that hot electron supercollisions describe the rate-limiting relaxation step in graphene. *Nano Letters*, 13:5497–5502, 2013.

[84] F. Speck, J. Jobst, F. Fromm, M. Ostler, D. Waldmann, M. Hundhausen, H. B. Weber, and Th. Seyller. The quasi-free-standing nature of graphene on H-saturated SiC(0001). *Applied Physics Letters*, 99:122106, 2011.

[85] I. Crassee, J. Levallois, A. L. Walter, M. Ostler, A. Bostwick, E. Rotenberg, T. Seyller, D. van der Marel, and A. B. Kuzmenko. Giant Faraday rotation in single- and multilayer graphene. *Nature Physics*, 7:48–51, 2011.

[86] M. Mittendorff, F. Wendler, E. Malic, A. Knorr, M. Orlita, M. Potemski, C. Berger, W. A. de Heer, H. Schneider, M. Helm, and S. Winnerl. Carrier dynamics in Landau-quantized graphene featuring strong Auger scattering. *Nature Physics*, 11:75–81, 2015.

[87] E. Malic, T. Winzer, E. Bobkin, and A. Knorr. Microscopic theory of absorption and ultrafast many-particle kinetics in graphene. *Physical Review B*, 84: 205406, 2011.

[88] E. Malic and A. Knorr. *Graphene and carbon nanotubes - ultrafast relaxation dynamics and optics.* Wiley-VCH, Weinheim, Germany, 2013.

[89] S. L. Palfrey and T. F. Heinz. Coherent interactions in pump-probe absorption measurements: the effect of phase gratings. *Journal of the Optical Society of America B*, 2:674–679, 1985.

[90] M. Teich, M. Wagner, H. Schneider, and M. Helm. Semiconductor quantum well excitons in strong, narrowband terahertz fields. *New Journal of Physics*, 15:065007, 2013.

[91] G. Konstantatos, M. Badioli, L. Gaudreau, J. Osmond, M. Bernechea, F. P. Garcia de Arquer, F. Gatti, and F. H. L. Koppens. Hybrid graphenequantum dot phototransistors with ultrahigh gain. *Nature Nanotechnology*, 7:363–368, 2012.

[92] M. Freitag, T. Low, F. Xia, and P. Avouris. Photoconductivity of biased graphene. *Nature Photonics*, 7:53–59, 2013.

[93] P. K. Herring, A. L. Hsu, N. M. Gabor, Y. C. Shin, J. Kong, T. Palacios, and P. Jarillo-Herrero. Photoresponse of an electrically tunable ambipolar graphene infrared thermocouple. *Nano Letters*, 14:901–907, 2014.

[94] J. Yan, M.-H. Kim, J. A. Elle, A. B. Sushkov, G. S. Jenkins, H. M. Milchberg, M. S. Fuhrer, and H. D. Drew. Dual-gated bilayer graphene hot-electron bolometer. *Nature Nanotechnology*, 7:472–478, 2012.

[95] D. Spirito, D. Coquillat, S. L. De Bonis, A. Lombardo, M. Bruna, A. C. Ferrari, V. Pellegrini, A. Tredicucci, W. Knap, and M. S. Vitiello. High performance bilayer-graphene terahertz detectors. *Applied Physics Letters*, 104: 061111, 2014.

[96] X. Du, D. E. Prober, H. Vora, and C. B. Mckitterick. Graphene-based bolometers. *Graphene and 2D Materials*, 1:1–22, 2014.

[97] M. Mittendorff, S. Winnerl, J. Kamann, J. Eroms, D. Weiss, H. Schneider, and M. Helm. Ultrafast graphene-based broadband thz detector. *Applied Physics Letters*, 103:021113, 2013.

[98] S. Winnerl, W. Seiwerth, E. Schomburg, J. Grenzer, K. F. Renk, C. J. G. M. Langerak, A. F. G. van der Meer, D. G. Pavelev, Yu. Koschurinov, A. A. Ignatov, B. Melzer, V. Ustinov, S. Ivanov, and P. S. Kopev. Ultrafast detection and autocorrelation of picosecond thz radiation pulses with a GaAs/AlAs superlattice. *Applied Physics Letters*, 73:2983–2985, 1998.

[99] S. D. Ganichev, Y. V. Terentev, and I. D. Yaroshetskii. Photon-drag photodetectors for the far-IR and submillimeter regions. *Soviet Technical Physics Letters*, 11:20, 1985.

[100] F. Klappenberger, A. A. Ignatov, S. Winnerl, E. Schomburg, W. Wegscheider, K. F. Renk, and M. Bichler. Broadband semiconductor superlattice detector for THz radiation. *Applied Physics Letters*, 78:1673–1675, 2001.

[101] S. Preu, M. Mittendorff, S. Winnerl, H. Lu, A. C. Gossard, and H. B. Weber. Ultra-fast transistor-based detectors for precise timing of near infrared and THz signals. *Optics Express*, 21:17941–17950, 2013.

Publications in refereed journals

- M. Mittendorff, F. Wendler, E. Malic, A. Knorr, M. Orlita, M. Potemski, C. Berger, W. A. de Heer, H. Schneider, M. Helm, and S. Winnerl, "Carrier dynamics in Landau-quantized graphene featuring strong Auger scattering", Nat. Phys. **11**, 75-81 (2015).

- M. Mittendorff, M. Orlita, M. Potemski, C. Berger, W. A. de Heer, H. Schneider, M. Helm, and S. Winnerl, "Intraband carrier dynamics in Landau-quantized multilayer epitaxial graphene", New. J. Phys. **16**, 123021 (2014).

- F. Kadi, T. Winzer, E. Malic, F. Göttfert, M. Mittendorff, S. Winnerl, M. Helm, and A. Knorr, "Microscopic description of intraband absorption in graphene: the occurrence of transient negative differential transmission", Phys. Rev. Lett. **113**, 035502 (2014).

- S. Pavlov, N. Deßmann, V. N. Shastin, R. Kh. Zhukavin, B. Redlich, A. F. G. van der Meer, M. Mittendorff, S. Winnerl, N. V. Abrosimov, H. Riemann, and H.-W. Hübers, "Terahertz stimulated emission from silicon doped by hydrogenlike acceptors", Phys. Rev. X **4**, 021009 (2014).

- M. Mittendorff, T. Winzer, E. Malic, A. Knorr, C. Berger, W. A. de Heer, H. Schneider, M. Helm, and S. Winnerl, "Anisotropy of excitation and relaxation of photogenerated charge carriers in graphene", Nano Lett. **14**, 1504-1507 (2014).

- N. Deßmann, S. G. Pavlov, V. N. Shastin, R. Kh. Zhukavin, V. V. Tsyplenkov, S. Winnerl, M. Mittendorff, N. V. Abrosimov, H. Riemann, and H.-W. Hübers, "Time-resolved electronic capture in n-type germanium doped with antimony", Phys. Rev. B **89**, 035205 (2014).

- M. Xu, M. Mittendorff, R. J. B. Dietz, H. Künzel, B. Sartorius, T. Göbel, H. Schneider, M. Helm, and S. Winnerl, "Terahertz generation and detection

with InGaAs-based large-area photoconductive devices excited at $1.55\,\mu$m", Appl. Phys. Lett. **103**, 251114 (2013).

- S. Preu, M. Mittendorff, S. Winnerl, H. Lu, A. C. Gossard, and H. B. Weber, "Ultra-fast transistor-based detectors for precise timing of near infrared and THz signals", Opt. Express **21**, 17941-17950 (2013).

- M. Mittendorff, S. Winnerl, J. Kamann, J. Eroms, D. Weiss, H. Schneider, and M. Helm, "Ultrafast graphene-based broadband THz detector", Appl. Phys. Lett. **103**, 021113 (2013).

- M. Beck, I. Rousseau, M. Klammer, P. Leiderer, M. Mittendorff, S. Winnerl, M. Helm, G. N. Gol'tsman, and J. Demsar, "Transient increase of the energy gap in superconducting NbN thin films excited by resonant narrow-band terahertz pulses", Phys. Rev. Lett. **110**, 267003 (2013).

- M. Mittendorff, M. Xu, R. J. B. Dietz, H. Künzel, B. Sartorius, H. Schneider, M. Helm, and S. Winnerl, "Large area photoconductive THz emitter for $1.55\,\mu$m excitation based on an InGaAs heterostructure", Nanotechnology **24**, 214007 (2013).

- S. Winnerl, F. Göttfert, M. Mittendorff, H. Schneider, M. Helm, T. Winzer, E. Malic, A. Knorr, M. Orlita, M. Potemski, M. Sprinkle, C. Berger, and W. A. de Heer, "Time-resolved spectroscopy on epitaxial graphene in the infrared spectral range: relaxation dynamics and saturation behavior", J. Phys.-Condens. Mat. **25**, 054202 (2013).

- S. Boppel, A. Lisauskas, M. Mundt, D. Seliuta, L. Minkevičius, I. Kašalynas, G. Valušis, V. Krozer, M. Mittendorff, S. Winnerl, and H. G. Roskos, "CMOS integrated antenna-coupled field-effect-transistors for the detection of radiation from 0.2 to 4.3 THz", IEEE T. Microw. Theory **60**, 3834-3843 (2012).

- T. Winzer, A, Knorr, M. Mittendorff, S. Winnerl, D. Sun, T. B. Norris, M. Helm, and E. Malic, "Absorption saturation in optically pumped graphene", Appl. Phys. Lett. **101**, 221115 (2012).

- S. Winnerl, R. Hubrich, M. Mittendorff, H. Schneider, and M. Helm, "Universal phase relation between longitudinal and transverse fields observed in focused terahertz beams" New J. Phys. **14**, 103049 (2012).

- S. Preu, M. Mittendorff, H. Lu, H. B. Weber, S. Winnerl, and A. C. Gossard, "1550 nm ErAs:In(Al)GaAs large area photoconductive emitter", Appl. Phys. Lett. **101**, 101105 (2012).

- C. Kaya, C. Schneider,A. Al Shemmary, W. Seidel, M. Kuntzsch, J. Bhattacharyya, M. Mittendorff, P. Evtushenko, S. Winnerl, G. Staats, M. Helm, N. Stojanovic, P. Michel, and M. Gensch, "Phase sensitive monitoring of electron bunch form and arrival time in superconducting linear accelerators", Appl. Phys. Lett. **100**, 141103 (2012).

129

Acknowledgment

In this last part of my thesis I would like to thank all the people who helped me during my work over the last years. First of all, I want to thank my project leader Stephan Winnerl, who answered all my questions in an incredibly patient way and allowed me great latitude in my work. His supportive way helped me a lot during the last four years. I am very grateful to my thesis supervisors Manfred Helm and Joachim Ohser, who always were available in the background and helped me with my writing and presentations.

Furthermore I want to thank all the cooperation partners contributing to the different parts of this thesis. Milan Orlita and Marek Potemski from the high-magnetic field lab in Grenoble cooperated in the experiments and the discussion of the results. The samples were grown by Mike Sprinkle, Claire Berger and Walter de Heer from the Georgia Institute of Technology. Ermin Malic, Florian Wendler, Torben Winzer, Faris Kadi and Andreas Knorr from the Technical University in Berlin supported our work with their theory. Furthermore, I am grateful for fruitful discussions with them about our experiments. Josef Kamann, Jonathan Eroms and Dieter Weiss from the University in Regensburg did a great job in fulfilling all my wishes concerning the production of graphene flakes and the clean-room processing afterwards. I also want to thank Sergey Ganichev and Christoph Drexler from the University in Regensburg. They afforded the detector tests with a THz gas laser.

Of course, I want to thank all my colleagues from the spectroscopy department, namely Harald Schneider, Martin Teich, Sabine Zybell, Faina Eßer, Markus Fehrenbacher, Carsten Franke, Daniel Stephan, Jayeeta Battacharyya, Johannes Schmidt, Manos Dimakis and Uta Lucchesi. They provided a great work environment and were always helpful. I also want to thank all temporary coworkers who helped a lot during their stay, namely Xu Ming, Christoph Böttger, Fabian Göttfert, and Riko Kießling.

The whole (F)ELBE team was very important for a large part of my work and I am grateful for their dedicated support. They always worked hard to get the best

Versicherung

Hiermit versichere ich, dass ich die vorliegende Arbeit ohne unzulässige Hilfe Dritter und ohne Benutzung anderer als der angegebenen Hilfsmittel angefertigt habe; die aus fremden Quellen direkt oder indirekt übernommenen Gedanken sind als solche kenntlich gemacht. Die Arbeit wurde bisher weder im Inland noch im Ausland in gleicher oder ähnlicher Form einer anderen Prüfungsbehörde vorgelegt.

Ich erkenne die Promotionsordnung der Fakultät Mathematik und Naturwissenschaften der Technischen Universität Dresden an.

Diese Arbeit entstand am Helmholtz-Zentrum Dresden-Rossendorf unter wissenschaftlicher Betreuung durch Prof. Dr. Manfred Helm, Professor im Institut für Angewandte Photophysik der Fakultät Mathematik und Naturwissenschaften der Technischen Universität Dresden.

Dresden, den 02.07.2014

Martin Mittendorff